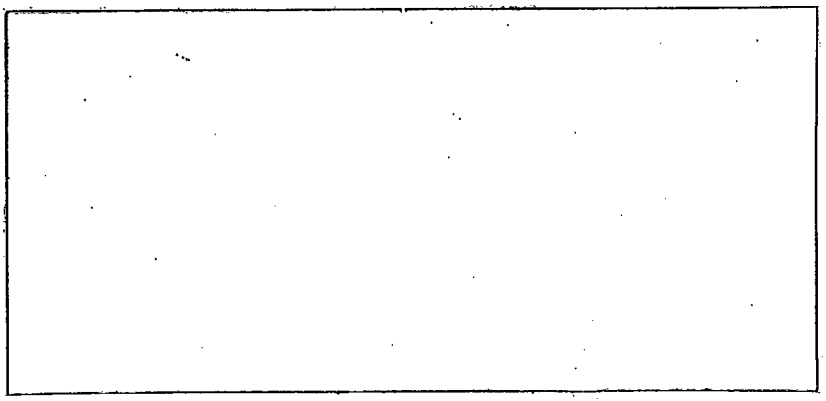

Materials Science Center

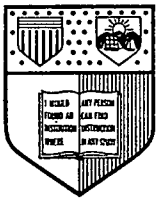

Cornell University

ITHACA, NEW YORK

DISCLAIMER

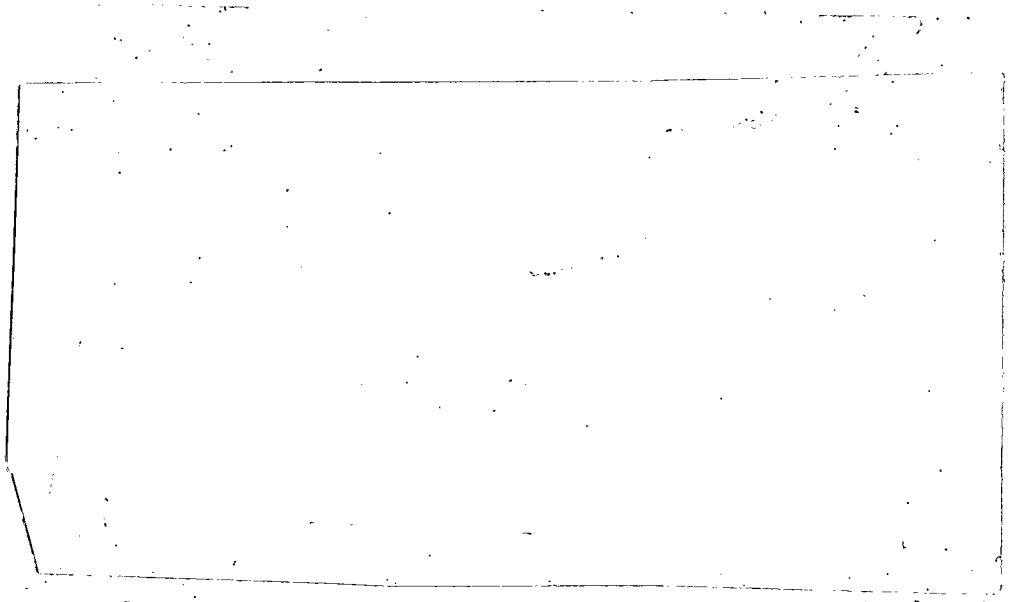

This report has been prepared by the Central Report Facility of the Materials Science Center.

Report #1872
COO-3151-9

SOME SIZE EFFECTS IN METALS IN THE FAR INFRARED

by

David Burnham Tanner

Ph. D. Thesis
August 1972

Research Group:
Prof. A. J. Sievers
LASSP

ACKNOWLEDGMENTS

It gives me great pleasure to acknowledge the guidance of Professor A. J. Sievers during this work. His constant interest and enthusiasm, valuable advice and large measure of practical help were essential to its completion. I also thank Professors J. W. Wilkins, N. D. Mermin, and D. B. Fitchen for serving on my special committee.

My four years of association with the far infrared group have been highly interesting and enjoyable ones and I thank all its members, past and present, who have made it so. In particular I thank Dr. R. D. Kirby for taking time to help me get started when he was trying to finish up. I have had interesting discussions on many subjects and some fine beer drinking sessions with my contemporaries in the group, Dr. G. Brandli, R. Blewitt, R. K. Elsley, Dr. K. C. Johnson, A. M. Kahan, W. J. Shotts, and Dr. A. J. Sievers.

I have had helpful discussions with Professor J.W. Wilkins, Dr. B. R. Patton, and R. A. Buhrman. R. A. Buhrman is also to be thanked for preparing all of the small particle samples.

Thanks also to Helen Consla for typing the final copy of the thesis, to A. Turco for doing a great amount of maching, and to W. Bement for general technical assistance. A large amount of general support came from the machine shop, the Technical Operations Laboratory and other facilities of the Material Science Center.

Financial support during my first three years at Cornell came from an NDEA title IV fellowship. This research has been supported by the U.S. Atomic Energy Commission through contract # AT(11-1)-3151, Technical Report #C00-3151-9.

TABLE OF CONTENTS

Table of Contents (continued)

LIST OF FIGURES

LIST OF FIGURES (CONTINUED)

LIST OF FIGURES (continued)

SOME SIZE EFFECTS IN METALS IN THE FAR INFRARED

David Burnham Tanner, Ph. D.
Cornell University, 1972

The far infrared transmission of lead thin films and of small metallic particles has been measured. In both of these systems, the sample size strongly affects the infrared response. The thin film measurements were made at temperatures near the superconducting transition temperature, where fluctuations in the superconducting order parameter give an extra contribution to the conductivity. This extra conductivity exists both above and below Tc and has its largest value at frequencies below a characteristic frequency.

$$\omega_F = \frac{16k_BT}{\pi h} \quad \frac{|T-T_c|}{T_c}$$

Calculations from the time dependent Ginsburg-Landau theory of the extra conductivity give a good description of the data.

The small particle measurements were made on powder samples of Cu, Al, Sn, and Pb. The diameter of the particles ranged from 65 A to 350 A. All of the samples showed absorption which was very small at low frequencies and which increased more or less linearly as the frequencies increased. There was no change in the absorbtion as the temperature was varied from 1.2° to 20° K, and there was no evidence for a superconducting energy gap below the bulk superconducting transition temperature in the Sn or Pb samples.

All of these measurements were made using a new He^3 refrigerator to cool the bolometer-detector. This cryostat used charcoal to absorb the He^3 gas. There are no moving parts in the He^3 gas system, instead cycling is accomplished by changing the temperature of the charcoal.

CHAPTER I

INTRODUCTION

This thesis is a description of two experiments in which the sample size greatly affects the far infrared response of the metals studied. One is the far infrared transmission of thin films of lead at the superconducting transition temperature and the other is the far infrared transmission of small particles of various metals.

The thread that ties these two problems together is the quantization of the wave vector, $\vec{k}$, of the electrons. The free electron model[1] of a metal begins with a free particle Schroedinger equation for the Fourier components of the electron wave function. Because the metal has surfaces which the electrons cannot penetrate, periodic boundary conditions are introduced:

$$\psi_{\vec{\kappa}}(x+L,y,z) = \psi_{\vec{\kappa}}(x,y,z)$$

and similarly for y and z. The wave function is of the form

$$\psi_{\vec{\kappa}} = \frac{1}{V} e^{i\vec{k}\cdot\vec{r}}$$

with the boundary conditions restricting the components of the wave vector to

$$k_x = 0, \frac{2\pi}{L}, \frac{4\pi}{L} \ldots$$

and similarly for k_y and k_z. The energy eigenvalues are

$$\varepsilon_\kappa = \frac{\hbar^2 k^2}{2m}$$

with $k^2 = k_x^2 + k_y^2 + k_z^2$.

According to the Pauli principle, two electrons are put in each energy level until all the N electrons are used up. The

uppermost filled level, the Fermi level, has the largest momentum value

$$k_F = \left(\frac{3\pi^2 N}{V}\right)^{1/3} \simeq \frac{\pi}{a}$$

where a is a lattice parameter. The Fermi energy is

$$E_F = \frac{\hbar^2}{2m}\left(\frac{3\pi^2 N}{V}\right)^{2/3}$$

This energy depends only on the concentration of electrons and not on their number or the volume. The density of states does, however, depend on the volume.

$$D(E) = \frac{Vmk}{\pi^2\hbar^2} = \frac{V}{2\pi^2}\left(\frac{2m}{\hbar^2}\right)^{3/2} E^{1/2}$$

Now, the general way that one calculates physical quantities is to Fourier transform the appropriate equation into momentum space and calculate the quantity for one component of the wave vector, e.g. as $F_{\vec{k}}$. Then at the end another Fourier transform regains the total quantity in real space. If there are a large number of values of the momentum (if L>>a) then an integral transform may be performed but if one or more of the dimensions of the sample is small then the component in those directions must be summed. The behavior for various dimensionalities is

$$\text{3D: } \frac{1}{V}\sum_{\vec{\kappa}} e^{-i\vec{k}\cdot\vec{r}} F_{\vec{k}} \rightarrow \int \frac{d^3k}{(2\pi)^3}\, e^{-i\vec{k}\cdot\vec{r}} F_{\vec{k}} = \int_0^\infty \frac{k^2 dk}{2\pi^2}\, e^{-i\vec{k}\cdot\vec{r}}\, F_{\vec{k}}$$

$$\text{2D: } \frac{1}{V}\sum_{\vec{\kappa}} e^{-i\vec{k}\cdot\vec{r}}\, F_{\vec{k}} \rightarrow \frac{1}{d}\sum_{k_z}\int \frac{d^2k}{(2\pi)^{1_2}} e^{-i\vec{k}\cdot\vec{r}} F_{\vec{k}} = \frac{1}{d}\sum_{k_z}\int_0^\infty \frac{k\, dk_1}{2}\, e^{-i\vec{k}\cdot\vec{r}}\, F_{\vec{k}}$$

1D: $\frac{1}{V}\sum_{\vec{\kappa}} e^{-i\vec{k}\cdot\vec{r}} F_{\vec{k}} \to \frac{1}{A}\sum_{k_x k_y} \int_{-\infty}^{\infty} \frac{dk_z}{2\pi} e^{-i\vec{k}\cdot\vec{r}} F_{\vec{k}}$

OD: $\frac{1}{V}\sum_{\vec{\kappa}} e^{-i\vec{k}\cdot\vec{r}} F_{\vec{k}}$ remains unchanged.

From the foregoing a simple argument arises as to why transitions are broadened in fewer than three dimensions. If one or more dimensions is small (not many times larger than the lattice parameter) then there are only a few momentum values allowed; the sum has only a few terms and will not approximate a step. It is not possible to get a sharp discontinuity with only a few terms in a Fourier series.

A similar argument comes from K. Wilson.[2] All of the measured quantities are calculated by performing thermodynamic averages. These involve sums of the form $\Sigma e^{-\frac{H}{kT}}$, where H is the Hamiltonian of the system and the sum goes over all possible configurations in the system. There can only be a singularity or a discontinuity if there is an infinite sum.

The next chapter, Chapter II, is a discussion of the far infrared techniques used in this work and the apparatus built during it. Among the former is Fourier transform spectroscopy and among the latter is a helium three temperature detector system that uses charcoal to adsorb the He^3 and has an associated evaporator for making thin films.

Chapter III is on the contributions of superconducting fluctuations to the far infrared transmission of thin films. The dc resistive transition of a thin film made from a super-

conductor is not sharp in temperature as in the bulk metal but is rounded off and has a certain intrinsic width.[3] This has been explained[4,5] as being due to fluctuations of the superconducting order parameter which cause small regions of the film to become superconducting (have finite order parameter or density of superconducting electrons). In these regions the pairs can be freely accelerated by the field and they will short out the normal regions around them. The resistance of the film is thereby reduced. The fluctuations have only a finite lifetime. The metal is above its transition temperature and so the superconductivity cannot be sustained indefinitely. As the temperature is reduced towards the transition temperature, T_c, the lifetime of the fluctuations becomes longer and their strength increases until at T_c the superconductivity freezes in. The characteristic frequency of the fluctuations (the inverse of the effective relaxation time) is

$$\omega_F = \frac{1}{\tau_F} = \frac{16 k_B T}{\pi \hbar} \cdot \frac{|T-T_c|}{T_c}$$

The measurements discussed in Chapter III show an increase in the conductivity above the conductivity of the normal state at frequencies below ω_F. In the superconducting state (below T_c) there is a similar contribution to the conductivity by the fluctuations. In both temperature ranges, the conductivities can be calculated using time dependent Ginsburg-Landau theory, and the transmission of the film calculated from the conductivities. These calculations agree with the measurements quite well.

Chapter IV gives the results of measurements on small metallic particles. These are powders made up of spherical

particles of the metal, all with diameters around 100 Å. In these samples there is a size quantization of the electron energy levels, given by

$$\Delta = \frac{2}{D(E_F)} = \frac{4E_F}{3N}$$

where E_F is the Fermi energy and N is the number of electrons. For an 100 Å diameter particle N~10,000. The electrons have a mean energy level spacing on the order of an meV, rather than being in a band. This will affect the behavior of the metal substantially. One might expect that light with photon energies below the energy spacing of the Fermi surface and the first level above the Fermi surface would not be absorbed and would penetrate a collection of these particles rather readily. As the photon energies are increased the samples begin to absorb. Because of size inhomogeneities and particle irregularities there will not be absorption in bands. It will instead increase with increasing frequency. Chapter IV presents data on measurements of small particles of copper, aluminum, tin, lead and carbon.

CHAPTER II

FAR INFRARED TECHNIQUES AND APPARATUS

1. General.

The far infrared lies at the extreme long wavelength end of what may be called the optical region of the electromagnetic spectrum. It is characterized by the use of continuous sources, mirrors, lenses, and gratings. It is generally considered to extend from 2 to 200 cm^{-1}, where the frequency is measured in wave number or inverse centimeter, and is the inverse of the wavelength: $\tilde{\nu} = 1/\lambda = \nu/c$. One may convert from wave number to other energy units by the following relations:

$$1\ cm^{-1} = 30GH_z = .124\ meV = 1.44^{o}\ K = 1.99 \times 10^{-16}\ erg.$$

The far infrared is one of the more inaccessible spectral regions on account of the small amount of energy available from radiant sources at these frequencies.

One may estimate the output of the mercury arc lamp used as a source in these experiments, in a spectrum peaked at 30 cm^{-1}, to be 50 μW into a f/1.4 collecting mirror. To make these estimates one integrates the Rayleigh-Jeans[6] law to find the radiated power from zero up to a frequency, ν, to be

$$P_o^{\nu} = \frac{2\pi}{3} A \frac{kT\nu^3}{c^2}$$

where the area of the source, A, is 5 cm^2 and its temperature, T, is 5000^{o} K. Of this power perhaps 1 μW makes it to the detector.

There are three ways to overcome this energy limitation:

improve the output of sources, use more sophisticated spectroscopic techniques, and improve the sensitivity of detectors. The first possibility has not yet occurred; the mercury arc lamp used in these experiments is very similar to the one used by Hagen and Reubens[7] in the first far infrared experiments on metals at the beginning of this century. There has been no improvement in far infrared sources in the last sixty years. On the other hand spectroscopic techniques and detectors have improved dramatically in that time.

2. Interferometry.

The spectroscopic method used in these experiments is called interferometry or Fourier transform spectroscopy. Instead of dispersing the source output into different angles according to frequency as with a grating one generates an interference between two beams, sorting the radiation according to phase difference. To understand this, consider the figure at the right. It shows a Michelson interferometer, with source S, detector D, beam splitter B, and mirrors M (moveable) and M' (fixed). Initially, let S be a monochromatic source and the distances from the beam splitter to the mirrors be the same. Then there is no phase difference between the two beams when they recombine, they interfere constructively, and the signal at the detector is a maximum. Now move mirror M away from the beam splitter a distance ¼λ,

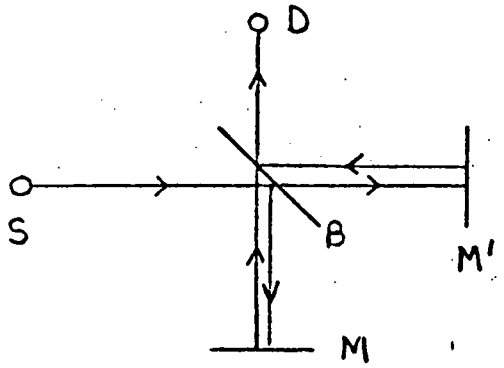

Fig. 1. Michelson Interferometer

introducing a phase difference ½λ between the two beams. They interfere destructively as they are 180° out of phase and the intensity at the detector is zero. Another ¼λ step brings the beams in phase again and the detector sees a maximum signal again. The signal continues to vary sinusoidally as M is moved along. Fourier transforming the cosine wave so obtained gives the delta function frequency dependence of the source. Now let the source have a width from ν_1 to ν_2, and move mirror M away from zero phase difference as before. The signal will initially vary as before but will damp out until at some phase difference, Δ_m, ν_2 will be out of phase and ν_1 will be in phase. At this point one is said to have resolved the line. The resolution is $\delta\nu = 1/\Delta_m$.

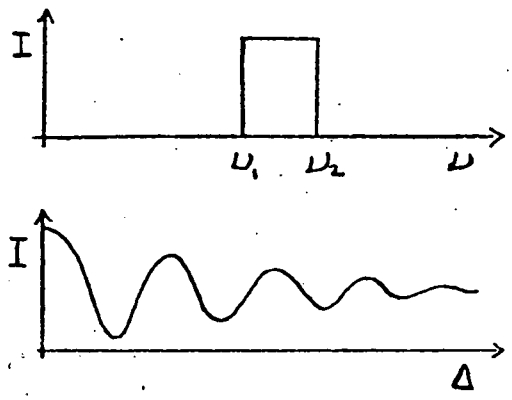

Figure 2. Resolution

The advantage of interferometry was first pointed out by Fellgett.[8] It is that, as opposed to grating spectrometers, an interferometer has the entire spectral region of interest incident on the detector all of the time, rather than just one resolution width. If, now, one is detector noise limited then the signal to noise ratio is increased only as the square root of the integration time. If one increases the signal by the number of resolution widths in the spectrum as one does with an interferometer compared to a grating machine, then the entire spectrum can be taken with the interferometer in the same time that the grating machine needs for one resolution

width.

Interferometry has been discussed in detail by Strong,[9] Genzel,[10] Nolt,[11] and Richards[12] in particular the latter. The interferometer used in these measurements is a lamellar grating interferometer described by Nolt, Kirby, Lytle, and Sievers.[11,13,14] In a lamellar grating the wave division is accomplished by a set of interleaved plates. These plates are efficient down to the lowest frequencies while the dielectric film in a Michelson is not. This instrument is useful from 2 to 70 cm^{-1}, and is shown in Figure 3.

3. Detectors

The infrared detector used in all of this work was a germanium bolometer operating at 0.3° K first discovered by Drew and Sievers[15] and described by Drew.[16] This type of detector is probably the most sensitive far infrared bolometer in general use today and has a measured noise equivalent power of NEP of 3×10^{-14} Watt compared to the NEP of 5×10^{-13} Watt reported by Low[17] for 2.1° K Germanium bolometer. This fifteenfold increase in sensitivity arises from two factors. There is a reduction of thermal noise due to a decrease in the detector operating temperature and there is a large increase in responsivity due to the steeper slope of the resistance versus temperature curve at the lower temperature. This second effect is the more important. Later in this chapter a He^3 refrigerator will be described that lead to an improvement in detector noise figures over those described by Drew and Sievers.

4. Electronics

A block diagram of the entire far infrared experimental

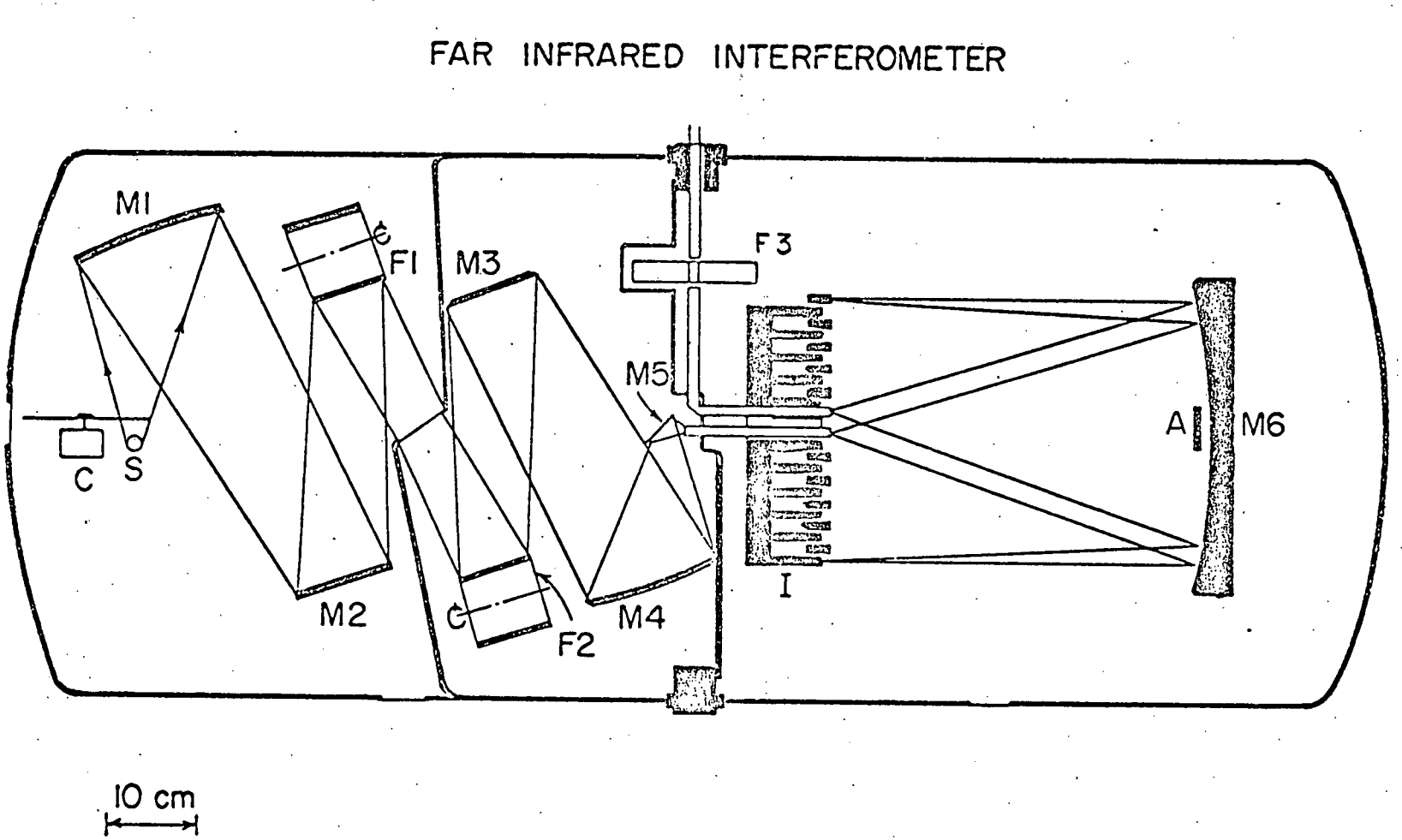

Fig. 3. Top view of the interferometer. F1, F2, and F3 are low pass filters; M1-M6 are mirrors; I is the lamellar grating.

arrangement is shown in Fig. 4. The signal from the detector is amplified and rectified by a phase sensitive amplifier and digitized by a voltage to frequency converter plus frequency counter or scaler. The digital data is then sent on line to a PDP 11 computer.[18] During a run, while the interferogram is being taken, the computer Fourier transforms the current number of points and displays the spectrum or ratio to a previously obtained spectrum on an oscilloscope, using a program written and described by Kahan.[19] The computer also controls the interferometer stepping motor. This allows the computer to check for noise spikes in the incoming data and retake a point if it detects one. At the end of a run the spectrum or ratio may be plotted on an X-Y recorder and the interferogram is punched on paper tape. More sophisticated analysis programs are also available for off line use.

5. Charcoal Pump System.

This section describes the construction and operation of a cryostat using cooled charcoal to pump on the He^3 used to cool the detector that was built by the author during the course of these experiments. It is unique in that the He^3 gas system has no moving parts; the He^3 is permanently stored in the cryostat.

This apparatus is shown diagramatically in Fig. 5. The drawing also shows an evaporator insert in place in the cryostat. The main system will be described first. At the bottom of the figure is the detector section vacuum can. This isolates the

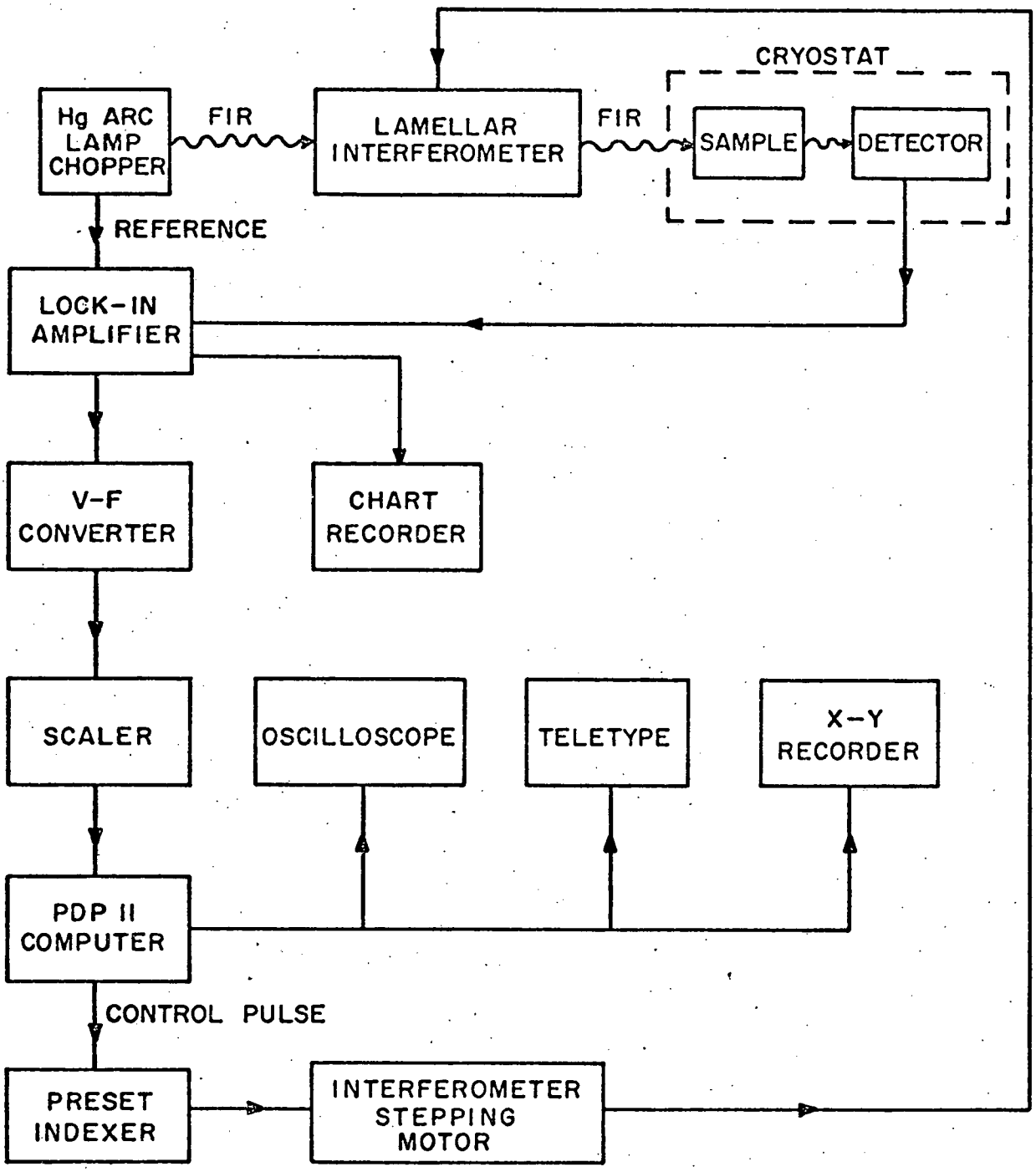

Fig. 4. Schematic diagram of the data acquisition system.

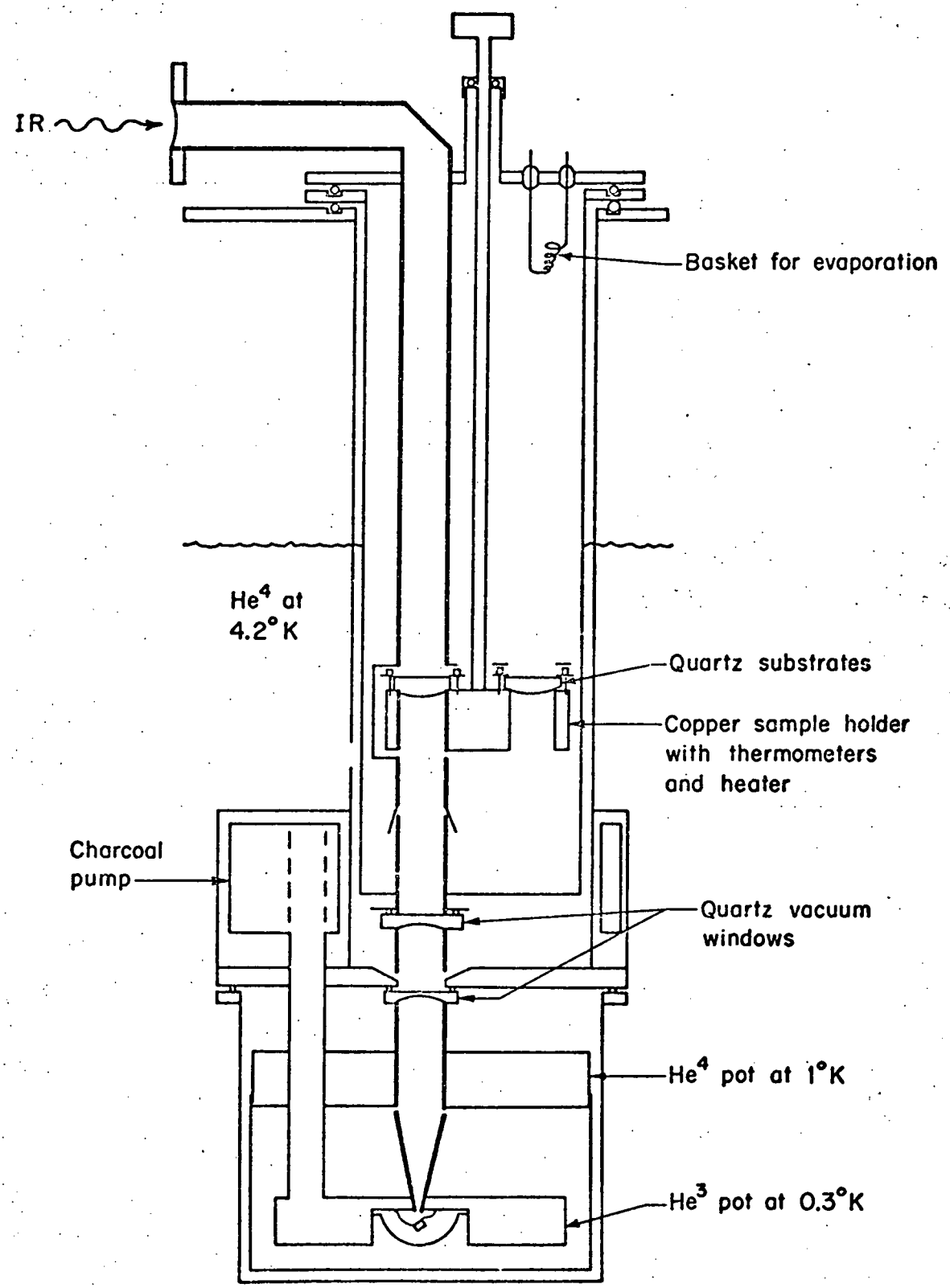

Fig. 5. Sketch of detector cryostat and evaporator insert. Glass liquid helium and liquid nitrogen dewars surround the cryostat.

0.3^{o}K He^{3} section and the 1^{o} K pumped He^{4} section from the outer 4.2^{o} K bath. The can is connected with an indium O-ring to the flange above it as is the quartz vacuum window through which the far infrared radiation passes on its way from the sample section to the detector section. The radiation goes down a short section of ½ inch brass light pipe which takes it through th 1^{o} K section. Then comes a condensing cone which reduces the cross sectional area of the radiation from ½ to $3/16^{th}$ of an inch while increasing the maximum angle that it makes with the axis of the light pipe from 18^{o} to 90^{o}. The radiation then enters the hemispherical integrating cavity where sits the detector.

The detector is the very piece of germanium used by Drew in his He^{3} refrigerator, re-etched and with new leads soldered on. The ground lead which serves as the heat sink to the 0.3^{o} K bath is now .025 inch diameter OFHC copper wire, increasing the thermal conductivity considerably over that of Drew's .010 inch. The signal lead is Tophet "A" which is .001 inch in diameter and has a resistance of 140 Ω/foot. The detector etching solution was a mixture of 5 parts HF, 5 parts HCH_2COOH, and 8 parts HNO_3. The leads were soldered on with indium solder using an ultrasonic soldering iron and no flux. It is not known what effect the decay of the unstable indium isotope has on the detector noise performance.

The charcoal pump is located in a vacuum can just above the detector section. The charcoal pump is in cross section an eccentric annulus surrounding the sample section and has a volume of 400 cm^{3}. It is filled full with cocoanut charcoal

obtained from Arthur B. Little Co.[20] This charcoal has a relatively large grain size, about 2mm in diameter, so that the He^3 can circulate freely in the pump. The charcoal was put in the pump through a ½ inch diameter hole in its bottom flange after which a brass plug was soldered in place. The pump line from the pump to the He^3 pot is a 3/8 inch diameter stainless steel tube, except for the condenser in the 1^o section which is a copper rod with seven $1/16^{th}$ inch holes in it. The stainless tube goes through the entire length of the charcoal pump but has many slots sawed in it to allow passage of the gas and prevent the charcoal from falling into the He^3 section. A 1/8 inch tube goes from the top of the pump to the cryostat top plate where there is a pressure gauge and needle valve to seal the He^3 in. There is currently three stp liters of He^3 gas in the system, at a pressure of 12 atmospheres.

The charcoal pump is surrounded by a vacuum can to give thermal isolation from the outside 4.2^o bath. The bottom flange of this vacuum can is also the top flange of the detector vacuum can. This is an unfortunate arrangement as it causes the needle valve through which the inner 1^o can is filled to be placed above the charcoal pump vacuum section. Initially the pumping line for this 1^o pot passed through the charcoal pump and it was not possible to fill the inner can with the charcoal pump warm. As a consequence the system had to be modified to bring the He^4 pump line through the charcoal pump with a double walled section, for vacuum thermal

insulation. A better arrangement would have the charcoal pump and its vacuum isolation moved upwards a few inches and the needle valve placed below it with the needle valve actuating rod passing clear through the charcoal pump section.

Along with the He^3 fill line there are also going up to the top plate the He^4 pump line, two needle valve actuating rods, the sample section, and two pumpout tubes for the two vacuum sections which also carry electrical leads for the various thermometers, heaters, and the detector and its load resistors. In the pump section there are three heaters and two 1 KΩ carbon resistors. One of these is connected externally to a battery, series resistor, and 50 microammeter as a ohmmeter-thermometer. In the detector section there are 1 KΩ carbon resistors on both the He^4 and He^3 cans. There is a heater on the He^3 can. There are two detector load resistors: a series connection of eight 950 KΩ metal film resistors and one of two 750 KΩ wire wound resistors.

The sample section is a 2½ inch O.D. stainless steel tube which extends from the cryostat top plate to the flange which carrys the quartz window. There is a conical depression in this flange above the window to act as a guide in alignment of the lower light pipe of the sample insert. The distance from the bottom of the sample insert top plate to the $9/16^{th}$ inch diameter of this cone is 40½ inches. There is a needle valve in the wall of the sample section located just above the charcoal pump. If opened this valve allows liquid helium to enter the sample section; if closed the sample may be left in vacuum.

However this latter arrangement apparently only works if the needle valve is closed tightly at room temperature after which it cannot be opened when the cryostat is cooled down. It is not possible to make a leak tight seal at low temperatures with the valve currently used.

The sample section used here is similar to others built earlier in our laboratory and permits a wide variety of general or special purpose sample inserts to be used and also allows samples to be changed by merely unbolting them from the top, lifting them out, and inserting the new sample, without having to break any low temperature seals. In fact, samples can be easily changed while the detector is running.

The operation of the rig is as follows. The night before pump out the glass dewar double wall section and leave about 100μ of air pressure in it, pump out the helium and sample volume and backfill it with an atmosphere of helium gas, pump out the charcoal pump vacuum insulation and add about 100μ pressure of air there, and if necessary pump out the detector can vacuum and backfill it with an atmosphere of helium gas. Fill the liquid nitrogen dewar. The next day, refill the nitrogen dewar and begin transferring liquid helium. The charcoal traps in the detector section will collect all of the helium exchange gas there by the time the inner cans are at 20° K. When the liquid helium level has reached the needle valves the inner 1° can will fill after some coaxing and should be pumped down, first closing the needle valve. Since the charcoal pump is still at 77° K the He^3 will condense against the 1° section and drip down

into the He^3 pot. This process takes from twenty minutes to half an hour and can be followed by watching the pressure gauge and the thermometers on the 1^o and He^3 cans. Condensation is complete when the temperatures of these two cans stabilize at their lowest value, around 10 Meg Ω.

After condensation, add the smallest possible amount of helium exchange gas to the vacuum can surrounding the charcoal pump and speed up the transfer, which has been going very slowly. When the charcoal pump has cooled to 20^o K it begins to pump and the He^3 bath is pumped down to 0.3^o K very quickly; about ten minutes is all it takes. When sufficient liquid helium has been transferred refill and pump down to 1^o pot and everything is ready to start taking the data. The total start-up time, from the beginning of the helium transfer to the start of the first interferogram, is about one and a half hours, although it can be done in less than an hour.

The signal from the detector stabilizes very rapidly and remains very stable; the signal level changes less than one percent over a period of six hours. The three stp liters of He^3 gas provides a running time of thirty-six hours at an estimated temperature of 0.30^o to 0.31^o K. This estimate was made from the detector resistance which is, when the light pipe is blocked off, 10 Meg Ω.

One curious and unforeseen feature of this cryostat has been named the autorecondense mode. This effect arises when changing samples. Placing a warm sample insert into an already

cold and operating cryostat blows off all of the liquid helium in the sample section. Heat is then transferred to the charcoal pump which warms up. The He^3 is deabsorbed and condenses against the 1^o section. When the sample cools down or when liquid helium is retransferred, the charcoal pump repumps down the He^3 bath and one is ready to take data for another thirty-six hours.

A normal recondense requires care in this system if one does not want to retransfer. The best method found to date is to add a tremendous amount of heat to the charcoal pump in a very short time, for example thirty watts for two minutes. The charcoal pump warms up very quickly to 40^o to 50^o K and enough He^3 is condensed to last for six to ten hours. The charcoal pump then cools down during the next five minutes or so and pumps down the He^3. If one is lucky there will be liquid helium above the charcoal pump and sample after this operation.

The detector in this system has, in comparison with Drew's detector, about twice the responsivity for large signals due perhaps to the increase in thermal conductivity of the gound lead. The noise voltage for small signals, estimated from the noise in low infrared intensity conditions, is 20 nV. Part of this factor of three or so improvement is due to the increased first grid resistance of the type D preamplifier in the PAR[21] HR-8 lock in amplifier. This resistance is 100MΩ, up by a factor of 10 from the old type A preamp. The 300^o K noise voltage of this input resistor is shorted out more fully by the detector with the type D preamp.

6. Evaporator

The usual sample insert for this cryostat is a five position sample rotator in a 2¼ inch can with the associated light pipes, right angle bends, and top plates. One special purpose insert constructed for these experiments is the evaporator shown in place in the dewar in Fig. 5. The evaporator is a long tube, 2 inches in diameter with a quartz vacuum window at the lower end. Near the top plate is a spiral wound tungsten basket from which the evaporation takes place. The substrates which are polished quartz blanks are clamped to the copper sample holder about twenty inches below the baskets. The sample holder is a two position sample rotator. In one position the substrate is in position for evaporation and after evaporation a rotation of 180^{o} brings the film into the far infrared beam and places the other substrate in position for evaporation. The substrates are held by brass clamps against indium pads for good thermal contact to the copper block. Attached to the sample holder are a heater and two thermometers, a 1 kΩ carbon resistor for the resistance bridge, and a 330Ω carbon resistor for the Artronix temperature controller. There are four leads connected to each film in order to allow the film resistance to be measured using a four probe technique. These leads are attached with indium solder to four narrow gold strips that had been evaporated onto the substrates before they were mounted. The copper sample holder is hollow and there exists the capability of transferring liquid helium into it through the hollow rotator rod, but this has not proven to work very well.

At top plate of the evaporator insert there are electrical feed throughs for the basket and the sample holder wiring and also an ionization gauge. On the bottom plate is a layer of charcoal. The sample holder, light pipe and can surrounding the sample holder are all carried on the evaporator top plate. There is on the bottom of the tube a stub of light pipe, which is picked up by a conical piece on the main light pipe. This stub passes through the bottom of the evaporator and ends with the quartz vacuum window holder. This vacuum window is sealed with an indium o-ring like the detector section vacuum window.

In operation, the evaporator is inserted into the cryostat when both are warm. It is pumped out with an oil diffusion pump to the 10^{-5} torr range. Then it is sealed off and the cryostat cooled down. As the cryostat cools to nitrogen temperature overnight the pressure in the evaporator rises to near 1×10^{-4} due to outgassing. When liquid helium is transferred the pressure at the ionization gauge, goes to the 10^{-7} range. After the detector cryostat is operating and the liquid helium filled, the evaporation is done. This is the time that one could transfer helium into the sample rotator. If this is done the helium will last for only twenty minutes and then the sample holder will warm to 30° K. If not done the sample holder will cool to 40° K in an hour. During the evaporation, the dc resistance of the film is monitored, mostly to determine when the film becomes electrically continuous. This is done by putting 60 microvolts in series with a 10 kΩ resistor across the leads to the film, and measuring the voltage across the

film with a Fluke[22] voltmeter. As the film resistance decreases during deposition the voltage measured by the Fluke will also decrease. With this arrangement it is always possible to get a continuous film and easy to get close to a desired resistance.

The evaporation rate is about 2 Å per minute; it takes three minutes to get a continuous lead film. After two films have been deposited sufficient helium exchange gas is added to the evaporator volume to bring the film temperature to 4.2° K and the far infrared measurements begin.

7. Manufacture of Small Particles.

The methods of preparation of the small particle samples were developed by R.A. Buhrman[23] and he also did the actual sample preparation. Here I will describe what I have learned by watching him. His thesis will give more details.

The majority of the samples studied were made by the smoke method. A tungsten boat containing the metal was prepared. This was put in bell jar inside a glass cylinder of five inches diameter on which the particles were collected. The system was evacuated and then helium gas was bled in. The helium pressure depended on two things: what size particles were wanted and what the atomic weight of the metal was. The larger the particle or the heavier the metal the higher the gas pressure. Typical pressures for copper were .5 to 2.5 mm He, for tin 1 to 5 mm He.

After the gas was in the boat was heated up until the metal was evaporating at a good rate and oxygen was bled in slowly.

The metal atoms coming off the boat collide with helium atoms and other metal atoms as they do a random walk to the collecting surface. They also pick up oxygen and when they are completely oxidized stop growing. It is possible to get quite small range in sizes by this method. After the evaporation the smoke was brushed off of the glass surface and collected.

The other sample preparation method was called the sludge method. In this, chunks of the metal of interest were placed in a beaker of acetone. An RF discharge between two electrodes there spark cut small chips off. As the discharge continued the chips were cut down smaller and smaller. Because the field tended to stay in the larger chunks they were the ones reduced in size, which helped to keep uniform size. After a while a colloidal suspension of particles in the acetone had been prepared. This could be centrifuged to eliminate the larger particles. Afterwards the acetone was evaporated with a hot plate to create a dried mass of small particles known as sludge.

The smoke has proven to be better in all ways than the sludge and all but the earliest samples were made by this method. The smoke forms a loose dry powder with a density only a few percent of the bulk metal. It is black in most cases, as it scatters visible light; some of the larger sizes are greyish. To do the far infrared experiments between 1/2 and 2 mm of the powder were clamped between two pieces of polyethelene, using a brass or nalgene tube as a spacer, and mounted on a standard sample rotator ring.

CHAPTER III

FLUCTUATIONS

1. General.

This chapter is a discussion of the far infrared transmission of thin films of lead or lead-bismuth near the superconducting transition temperature. It is in this temperature interval that the effects of fluctuations in the superconducting order parameter are expected to give the biggest contribution to the film conductivity. It is in the far infrared frequency region that the effects of the lifetimes of the fluctuations are seen.

Here is how the chapter will proceed. There will first be a review of previous results of experimental and theoretical work on the fluctuation problem. Next comes a derivation of the conductivities in the time dependent Ginsburg-Landeau theory of phase transitions. This is followed by a section on the noninfrared properties of my films; such as thickness, dc resistance, transition temperature and the like. Finally there are the far infrared measurements and their comparison with theory.

2. Previous Work.

It has long been known[24] that the resistive superconducting transitions of thin films were broader than those of bulk samples, but it was only with the papers of Glover[25] and of Ferrell and Schmidt[26] that anybody realized that there was any physics in the effect. At the suggestion of the latter, Glover measured the resistance of an amorphous bismuth film and found the

conductivity varied as $(T-T_c)^{-1}$. Shortly before this Aslamazov and Larkin[27] had published the first of a pair of papers in which they calculated the conductivity due to fluctuations using the microscopic theory and obtained the now famous result

$$\sigma' = \frac{e^2 T_c}{16\hbar d(T-T_c)}$$

where d is the film thickness and σ' is the extra conductivity due to the fluctuations. The measured conductivity is $\sigma = \sigma' + \sigma_N$. This result depends only on the thickness of the film and not on any other parameters. The constant,

$$\tau_o = \frac{e^2}{16\hbar} = 1.5 \times 10^{-5}\ \Omega^{-1}$$

This result was obtained to within a few percent in measurement on several thicknesses of bismuth films by Naugle and Glover.[28]

Après cela, le déluge. Many, many experimental measurements of the dc resistive transition appeared. A good number of these were on aluminum films (see for example Strongin et al[29] and Masker and Parks[30]) where the Aslamazov-Larkin results were not obtained; the transition being wider by a factor of ten. This has been explained by Maki[31] who adds another therm to the conductivity.

Measurements of the transition of lead films were made by Smith et al[32] who found the Aslamazov-Larkin result; by Testardi, Reed, et al[33] who found the transitions in most samples to be narrower than Aslamazov-Larkin by about a factor of two; and by Thompson et al[34] who find the transiton to be much narrower than Aslamazov-Larkin. It is not clear what a mechanisim in

lead is that would cause the transition width to be narrowed; it is possible to think of many reasons why the transition width might be broadened (inhomogeneities, uneven thickness, strains, and the like) but few that would go the other way. The only suggestion is that of Thompson et al[34] who suppose that the film might be composed of loosely connected grains.

The conductivity above the transition temperature was calculated using the time dependent Ginsburg-Landau equation at essentially the same time by both Schmid[35] and Schmidt.[36] Schmid obtained the dc conductivity, getting the same result as Aslamazov and Larkin. Schmidt also gets this result for the dc conductivity and he further calculates the frequency dependence of the fluctuation conductivity. This extra conductivity shows a peak at zero frequency whose height increase and whose width decreases as the transition temperature is approached. Schmidt has also calculated the conductivity as a function of frequency below the transition temperature and finds similar results.[37] Later in this chapter a derivation of the fluctuation conductivities will be presented that is similar to Schmidt's.

There have been measurements of the fluctuation conductivity in the microwaves by two groups. D'Aiello and Freedman[38] measured the transmission of aluminum films both above and below T_c at 20 GHz (.67 cm^{-1}) and found no extra conductivity. Their results did not agree with the Schmidt theory. Lehoczky and Briscoe[39] measured the transmission and reflection of lead films both above and below the transition at three frequencys (.7, 1.2, and 2.3 cm^{-1}) and found excellent agreement with Schmidt's theory.

3. The Phenomenon

The physical picture of the fluctuation phenomenon is as follows. As the superconductor is cooled down towards its transition temperature, small superconducting regions appear in it caused by fluctuations. These grow and decay in the course of time. The material cannot sustain bulk superconductivity but there is the possibility that small volumes in it can be superconducting for a while. Pairs will form for a short time, and while they exist they can be accelerated freely by an electric field. The conductivity of the material is increased as the fluctuations short out the normal material around them.

The size of the fluctuations is given by the Ginsburg-Landau[40] coherence length. This is the length over which the electron wavefunctions remain coherent,

$$\xi(T) = \xi_o \left| \frac{T_c}{T-T_c} \right|^{\frac{1}{2}}$$

where ξ_o is the BCS coherence length which is independent of temperature and equal to 980 Å in lead. There are fluctations in samples of all dimensionality, including the bulk. Their importance increases as the number of dimensions large compared to the coherence length is reduced. This is because the fluctating regions can save energy by touching the surfaces of the sample. The relative energies required are proportional to the volume of the fluctuations: $\xi^3 : \xi^2 D : \xi A$ in 3D, 2D, 1D.

As the temperature approaches the transition temperature from above the size of the fluctuations will increase and so

will their lifetime. It takes longer for a larger volume to decay. It will be shown shortly that the effective lifetime is

$$\tau_F = \frac{1}{\omega_F} = \frac{\pi \hbar}{16 k_B T} \frac{T_c}{|T-T_c|}$$

At the transition temperature the lifetime becomes infinite and bulk superconductivity sets in. The dc conductivity is infinite. However below T_c and at finite frequency the conductivity is finite and fluctuations in samples of restricted geometry will increase the conductivity. Just below the transition temperature the number of superconducting pairs is small and fluctuations in the normal electrons cause increases in the conductivity above the BCS value for finite frequency. As the sample is cooled away from the transition temperature the conductivity due to the fluctuations decreases, because the superconductivity becomes more stable.

Thus there is an effect of fluctuations both above and below the superconducting transition. The fluctuation components of the conductivity have similar (although not exactly the same) forms in both regions. The real part is a maximum at zero frequency, rolling off at the characteristic relaxation rate ω_F to zero. The imaginary part is zero at zero frequency, rises to a peak near ω_F and then drops to zero again. It should be pointed out that the regular conductivity (that not involving fluctuations) is quite different in the two regimes. It is constant and real above the transition and has the BCS form and is complex below.

4. Ginsburg-Landau Theory.

Here I will present a calculation of the extra conductivity, that due to superconducting fluctuations, using the time dependent form of the Ginsburg-Landau[40] theory of second order phase transitions. This theory begins with an expansion of the free energy in terms of the order parameter, $\underline{\psi}(x,t)$, of the system

$$F_S - F_N = \int dV(\alpha|\underline{\psi}|^2 + \tfrac{1}{2}\beta|\underline{\psi}|^4 + \frac{\hbar^2}{2m^*}|\nabla\underline{\psi}|^2)$$

where $\alpha \sim (T-T_c)$ so that it is positive above the transition temperature, T_c, zero at it, and negative below it. β is roughly independent of temperature. For a spatially uniform order parameter, minimizing F with respect to ψ leads to

$$\langle\underline{\psi}\rangle = \underline{\psi}_o = \begin{cases} 0 & T>T_c \\ \left(\frac{\alpha}{\beta}\right)^{\frac{1}{2}} & T<T_c \end{cases}$$

for the equilibrium value of $\underline{\psi}$. So $\langle\underline{\psi}\rangle$ is zero above the transition but not below it, which is just what we would like it to be. However, above T_c there will be fluctuations in the order parameter and the mean square fluctuation, $\langle|\psi|^2\rangle$, can be calculated very easily. Thermal averages of a quantity are done by weighting it with the free energy and integrating. The Fourier transform of free energy expression is, keeping terms only to second order in the order parameter, which is small

$$F_S - F_N = \int_V d^3X \sum_{\vec{k},\vec{k}'} \psi^*_{\vec{k}'}(t)\, \psi_{\vec{k}}(t)\, \frac{h^2}{2m^*} \left(\frac{1}{\xi^2} - \nabla^2\right) e^{i(\vec{k}-\vec{k}')\cdot\vec{x}}$$

Doing the volume integral leads to a Kroeniker delta, $\delta_{\vec{k},\vec{k}'}$, times the volume V. The k' sum can be immediately done.

$$F_S - F_N = V\frac{\hbar^2}{2m^*} \sum_k \psi_k^*(t)\, \psi_k(t) \left(\frac{1}{\xi^2} + k^2\right)$$

where ξ is the Ginsburg-Landau coherence length. If $\ell >> \xi_o$

$$\xi(T) = \left(\frac{h^2}{2m(\alpha)}\right)^{\frac{1}{2}} = \xi(o) \left|\frac{T_c}{T-T_c}\right|^{\frac{1}{2}} = .74\xi_o \left|\frac{T_c}{T-T_c}\right|^{\frac{1}{2}} = \frac{1.48\hbar\, V_F}{\pi\, 2\Delta} \left|\frac{T_c}{T-T_c}\right|^{\frac{1}{2}}$$

$$= 980\text{A}^{\text{o}} \left|\frac{T_c}{T-T_c}\right|^{\frac{1}{2}}$$

The third and fourth forms are from the microscopic theory (2Δ is the energy gap) and the last is for lead. If $\ell << \xi_o$ $\xi(o) = (\xi_o \ell)^{\frac{1}{2}}$ where ℓ is the mean free path. The Fourier transform of the order parameter, which appears in the free energy is defined by

$$\underline{\psi}(x,t) = \sum_{\vec{k}} \psi_{\vec{k}}(t) e^{-i\vec{k}\cdot\vec{x}}$$

Now thermal averages of time independent quantities are calculated by weighting the fluctuations with the free energy associated with them.

$$\langle |\psi_k(0)|^2 \rangle_o = \frac{\int d|\psi_k|^2\, e^{-\frac{F_k}{k_B T}} |\psi_k|^2}{\int d|\psi_k|^2\, e^{-\frac{F_k}{k_B T}}} = \frac{\int d|\psi_k|^2\, e^{-\frac{h^2(1+\xi^2k^2)}{2m^*\xi^2 k_B T}|\psi_k|^2} |\psi_k|^2}{\int d|\psi_k|^2\, e^{-\frac{h^2(1+\xi^2k^2)}{2m^*\xi^2 k_B T}|\psi_k|^2}}$$

and

$$\langle|\psi_k(0)|^2\rangle_o = \frac{m^* k_B T}{V h^2} \quad \frac{\xi^2}{1 + \xi^2 k^2}$$

above the transition temperature.

Below T_c there are also fluctuations in the order parameter producing deviations from the equilibrium value. It is the presence of this non-zero equilibrium value that introduces complications in the superconducting regime. The order parameter can be decomposed into the equilibrium part, ψ_o, and two non-equilibrium parts, the real (longitudinal) part, ψ, and the imaginary (transverse) part, ϕ.

$$\underline{\psi} = \psi_o + \psi + \phi$$

Putting this into the free energy formula, multiplying out and then only keeping terms of second order in the fluctuations, yields the following formula for the free energy

$$F_S - F_N = \int dV\{ \tfrac{1}{2} \alpha \psi_o^2 - 2\alpha|\psi|^2 + \frac{h^2}{2m} \left((\nabla\psi)^2 + (\nabla\phi)^2\right)\}$$

The Fourier transform of the free energy is

$$F_S - F_N = \tfrac{1}{2}\alpha V \psi_o^2 + V\frac{h^2}{2m^*} \sum_k \{(\frac{2}{\xi^2} + k^2) |\psi_k(t)|^2 + k^2|\psi_k(t)|^2\}$$

where below T_c, $\xi = \frac{h^2}{2m(-\alpha)}$. The mean square fluctuations are

$$\langle|\psi_k(0)|^2\rangle = \frac{m^* k_B T}{\hbar^2 V} \quad \frac{\xi^2}{2 + k^2\xi^2}$$

$$\langle|\phi_k(0)|^2\rangle = \frac{m^* k_B T}{\hbar^2 V} \quad \frac{1}{k^2}$$

The Ginsburg-Landau theory also provides a formula connecting the current to the order parameter.

$$\vec{J}(x,t) = \frac{e^*h}{2m^*i} \{\underline{\psi}^*(x,t)\ \nabla\underline{\psi}(x,t) - \nabla\underline{\psi}^*(x,t)\ \underline{\psi}(x,t)\}$$

The mean square fluctuations calculated above are not sufficient to give even the dc conductivity. It is necessary to average over all time differences between the current densities. For this, an equation describing the time evolution of the fluctuations is required. This is the time dependent Ginsburg-Landau equation. This equation has been discussed by Abrahams and Tsuento,[41] Caroli and Maki,[42] and Schmid.[43] The form that will be used here is

$$\frac{\partial}{\partial t}\underline{\psi}(x,t) = -\frac{8k_BT}{T_c\hbar}\left(\frac{T-T_c}{T_c}\right)\{1 + \frac{\beta}{\alpha}|\underline{\psi}(x,t)|^2 - \frac{\hbar^2}{2m\alpha}\nabla^2\}\underline{\psi}(x,t)$$

One should note that this resembles the Schroedinger equation.

The arguments and results of the calculation are different in details depending on whether the system is above or below its transition temperature. It will be done first for above the transition temperature and then the deviations for below the transition will be discussed.

5. Fluctuations Above the Transition.

Above T_c the time dependent equation becomes, ignoring the fourth order term

$$\frac{\partial}{\partial t}\underline{\psi}(x,t) = -\frac{8k_BT}{\pi\hbar}\left(\frac{T-T_c}{T_c}\right)(1-\xi^2\nabla^2)\underline{\psi}(x,t)$$

If we substitute for $\psi(\vec{x},t)$ its Fourier transform

$$\psi(\vec{x},t) = \sum_{\vec{k}} \psi_{\vec{k}}(t)\, e^{-\vec{k}\cdot\vec{x}}$$

$$\frac{\partial}{\partial t}\psi_{\vec{k}}(t) = -\frac{8k_BT}{\pi\hbar}\left(\frac{T-T_c}{T_c}\right)(1+\xi^2k^2)\,\psi_{\vec{k}}(t)$$

and $$\psi_{\vec{k}}(t) = \psi_{\vec{k}}(0)\, e^{-\frac{8k_BT}{\pi\hbar}\left(\frac{T-T_c}{T_c}\right)(1+\xi^2k^2)t}$$

This gives the time dependence. It is convenient to define a characteristic frequency or effective relaxation rate of the fluctuations as

$$\omega_F = \frac{1}{\tau_F} = \frac{16k_BT}{\pi\hbar}\left(\frac{T-T_c}{T_c}\right)$$

It is this frequency that the far infrared measurements are designed to check. Then

$$\psi_{\vec{k}}(t) = \psi_{\vec{k}}(0)\, e^{-\frac{\omega_F t}{2}(1+\xi^2k^2)}$$

The next step is to substitute into the current equation the Fourier transforms. For the current use

$$J(\vec{q},t) = \int d^3x\, J(\vec{x},t)\, e^{-\vec{q}\cdot\vec{x}}$$

Shortly the long wavelength limit ($q=0$) will be taken. The equation for the current becomes

$$\bar{J}(\bar{q},t) = \frac{e^*\hbar}{2m^*i}\int_V d^3x e^{-i\vec{q}\cdot\vec{x}} \sum_{\vec{k},\vec{k}'} \psi_{\vec{k}}^*(t)\,\psi_{\vec{k}'}(t)\, e^{-i(\vec{k}-\vec{k}')}\,(i\vec{k}'+i\vec{k})$$

Next, exchanging the integral and summation and doing the volume integral yields a Kroeniker delta, $\delta_{\vec{k},\vec{k}',q}$ times the volume V. Doing the sum of $\vec{k}'$ then gives, letting $2\vec{k}+\vec{q}\to\vec{k}$ or $\vec{k}\to\vec{k}-\frac{\vec{q}}{2}$

$$J(\vec{q},t) = \frac{e^*\hbar}{m^*} V \sum_{\vec{k}} \vec{k}\, \psi_{\vec{k}-\frac{\vec{q}}{2}}(t)\, \psi_{\vec{k}+\frac{\vec{q}}{2}}(t)$$

$$= \frac{e^*\hbar}{m^*} V \sum_{\vec{k}} \vec{k}\, e^{\frac{\omega_F t}{2}(2 + \xi^2(\vec{k}+\frac{\vec{q}}{2})^2 + \xi^2(\vec{k}-\frac{\vec{q}}{2})^2)}\, \psi^*_{\vec{k}-\frac{\vec{q}}{2}}(0)\, \psi_{\vec{k}+\frac{\vec{q}}{2}}(0)$$

where the solution of the time dependent equation has been substituted.

At this point an expression relating the current to the conductivity is required. It is necessary to average over all time differences between the current densities, i.e. to use the current-current correlation function. A form of time dependent perturbation theory called time dependent linear response theory can be used to connect the current-current correlation function to the conductivity. This is worked out in Appendix C, or see the article by Martin[44], and the result is

$$\sigma_{\mu\nu 1} = \frac{1}{\hbar\omega}\left(1-e^{-\frac{\hbar\omega}{kt}}\right)\frac{1}{V}\int_0^\infty dt \cos\omega t \,\langle J_\mu(\vec{q},t)\, J_\nu(-\vec{q},0)\rangle_o$$

$$\sigma_{\mu\nu 2} = \frac{1}{\hbar\omega}\left(1-e^{-\frac{\hbar\omega}{kt}}\right)\frac{1}{V}\int_0^\infty dt \sin\omega t \,\langle J_\mu(\vec{q},t)\, J_\nu(-\vec{q},o)\rangle_o$$

where σ_1 is the real part of the conductivity and σ_2 is the imaginary part. The indices μ and ν refer to the spatial coordinate directions of the conductivity tensor. The subscript on the correlation function means that the function is calculated using the wave functions of the unperturbed system. This is the central result of the linear response theory: the response of the system to an external perturbation depends only on the properties of the unperturbed system.

Now

$$\langle J_\mu(\vec{q},t)\ J_\nu(-\vec{q},0)\rangle_o = \left(\frac{e^*\hbar}{m^*}\right)^2 V^2 \sum_{\vec{k},\vec{k}'} k_\mu k'_\nu e^{-\omega_F t(1+\xi^2(k^2+\frac{q^2}{4}))} \times$$

$$\times \langle \psi^*(0)\ \psi(0)\ \psi^*(0)\ \psi(0)\rangle_o$$

$$k-\frac{q}{2}\quad k+\frac{q}{2}\quad k'+\frac{q}{2}\quad k'-\frac{q}{2}$$

The expectation value may be written in the mean field approximation

$$\langle \psi^*_{\vec{k}-\frac{\vec{q}}{2}}(0)\ \psi_{\vec{k}+\frac{\vec{q}}{2}}(0)\ \psi^*_{\vec{k}'+\frac{\vec{q}}{2}}(0)\ \psi_{\vec{k}'-\frac{\vec{q}}{2}}(0)\rangle_o = \langle \psi^*_{\vec{k}-\frac{\vec{q}}{2}}(0)\ \psi_{\vec{k}'-\frac{\vec{q}}{2}}(0)\rangle_o \times$$

$$\times \langle \psi_{\vec{k}+\frac{\vec{q}}{2}}(0)\ \psi^*_{\vec{k}'+\frac{\vec{q}}{2}}(0)\rangle_o$$

The mean field approximation is valid if the fluctuations do not interact with each other. Then those responding to $-\frac{\vec{q}}{2}$ are independent of those responding to $\frac{\vec{q}}{2}$ and the decomposition may be made as indicated. Now the wave vector of the electromagnetic radiation, $\vec{q}$, is much smaller than that of the electrons, $\vec{k}$. It has served its purpose and may be conveniently set to zero at this point. Then

$$\langle J_\mu(0,t)\ J_\nu(0,0)\rangle_o = \left(\frac{e^*\hbar}{m^*}\right)^2 V^2 \sum_{\vec{k},\vec{k}'} k_\mu k'_\nu\ e^{-\omega_F T(1+\xi^2 k^2)}$$

$$\langle \psi^*_{\vec{k}}(0)\ \psi_{\vec{k}'}(0)\rangle_o \langle \psi_{\vec{k}}(0)\ \psi^*_{\vec{k}'}(0)\rangle_o$$

but $\langle \psi_{\vec{k}} \psi^*_{\vec{k}'}\rangle \quad \delta_{\vec{k},\vec{k}'} \langle |\psi_{\vec{k}}|^2\rangle_o$ so the $\vec{k}'$ sum can be done immediately

and

$$\langle J_\mu(0,t)\ J_\nu(0,0)\rangle = \left(\frac{e^*\hbar}{m^*}\right)^2 V^2 \sum_{\vec{k}} k_\mu k_\nu e^{-\omega_F t(1+\xi^2k^2)} \langle|\psi_{\vec{k}}(0)|^2\rangle_o^2$$

From above

$$\langle|\psi_{\vec{k}}(0)|^2\rangle_o = \frac{m^* k_B T}{V\hbar^2} \frac{\xi^2}{1+\xi^2k^2}$$

The conversion of $\sigma_{\mu\nu}$ to a scalar requires an angular average which depends on the number of dimensions, n. The result is

$$\sigma_{\mu\nu} = \frac{1}{n}\sigma\,\delta_{\mu\nu}$$

The real part of the conductivity is now, with e* = 2e

$$\sigma_1(\omega) = \left(\frac{2e^2}{\hbar}\right)\frac{(k_BT)^2}{\hbar\omega}\left(1-e^{-\frac{\hbar\omega}{k_BT}}\right)\frac{n}{V}\sum_{\vec{k}}\frac{\xi^4\,k^2}{(1+\xi^2k^2)^2}\int_o^\infty dt\,\cos\omega t\, e^{-\omega_F t(1+\xi^2k^2)}$$

$$\sigma_1(\omega) = \frac{\pi e^2}{4\hbar}\left(\frac{T_c}{T-T_c}\right)\frac{k_BT}{\hbar\omega}\left(1-e^{-\frac{\hbar\omega}{k_BT}}\right)\frac{n}{V}\sum_{\vec{k}}\frac{k^2\xi^2}{(1+\xi^2k^2)\left((1+\xi^2k^2)^2+\frac{\omega 1^2}{\omega_F^2}\right)}$$

The imaginary part of the conductivity is

$$\sigma_2(\omega) = \left(\frac{2e}{\hbar}\right)^2\frac{(k_BT)}{\hbar\omega}\left(1-e^{-\frac{\hbar\omega}{k_BT}}\right)\frac{n}{V}\sum_{\vec{k}}\frac{\xi^4\,k^2}{(1+\xi^2k^2)^2}\int_o^\infty dt\,\sin\omega t\, e^{-\omega_F t(1+\xi^2k^2)}$$

$$= \frac{\pi e}{4\hbar}\left(\frac{T_c}{T-T_c}\right)\frac{k_BT}{\hbar\omega}\left(1-e^{-\frac{\hbar\omega}{k_BT}}\right)\frac{\omega}{\omega_F}\frac{n}{V}\sum_{\vec{k}}\frac{k^2\xi^2}{\left((1+\xi^2k^2)^2\left[(1+\xi^2k^2)^2+\frac{\omega^2}{\omega_F^2}\right)\right.}$$

With the exception of the term $\frac{k_BT}{\hbar\omega}\left(1-e^{-\frac{\hbar\omega}{k_BT}}\right)$ this is the same result for σ_1 that Schmidt obtains. At low frequencies, $\hbar\omega << k_BT$, this term reduces to unity. Notice that the complex

conductivity can be written

$$\sigma = \sigma_1 - \sigma_2 = \frac{\pi e^2}{4\hbar}\left(\frac{T_c}{T-T_c}\right)\frac{k_B T}{\hbar}\left(1-e^{-\frac{\hbar\omega}{k_B T}}\right)\frac{n}{V}\sum_{\vec{k}}\frac{k^2\xi^4}{(1+\xi^2k^2)^2\left((1+\xi^2k^2)+i\frac{\omega}{\omega_F}\right)}$$

This is similar to the Drude form. $\left(\sigma = \frac{\sigma_o}{1+i\omega\tau}\right)$

The above equations must now be evaluated for various dimensionalities of interest. In the case of this work this is for two dimensions and zero dimensions. The conductivities for the other dimensions are given by Schmidt.

In two dimensions (thin film)

$$\frac{n}{V}\sum_{\vec{k}} \rightarrow \frac{2}{d}\sum_{k_z}\int_A \frac{d^2k}{(2\pi)^2} = \frac{1}{\pi d}\sum_{k_z}\int_o^\infty kdk \xrightarrow{x=k\xi} \frac{1}{\pi d\xi^2}\sum_{k_z}\int_o^\infty xdx$$

Now, $k_z = 0, \frac{2\pi}{d}, \frac{4\pi}{d}, \frac{6\pi}{d}\ldots$ If $d<<\xi$ then only the $k_z = 0$ wave vector of the fluctuations will be excited since the maximum Fourier component of the fluctuations has $k\sim\frac{2\pi}{\xi}$. Thus the only term in the k_z sum which contributes and the only one which gives a singular result has $k_z = 0$.

$$\sigma_1(\omega) = \frac{e^2}{4\hbar d}\left(\frac{T_c}{T-T_c}\right)\frac{k_B T}{\hbar\omega}\left(1-e^{-\frac{\hbar\omega}{k_B T}}\right)\int_o^\infty \frac{x^3dx}{(1+x^2)\left((1+x^2)^2+\frac{\omega^2}{\omega_F^2}\right)}$$

$$= \frac{e^2}{16\hbar d}\left(\frac{T_c}{T-T_c}\right)\frac{k_B T}{\hbar\omega}\left(1-e^{-\frac{\hbar\omega}{k_B T}}\right)\frac{\omega_F}{\omega}\left(\pi-2\tan^{-1}\left(\frac{\omega_F}{\omega}\right)-\frac{\omega_F}{\omega}\ln\left(1+\frac{\omega^2}{\omega_F^2}\right)\right)$$

and

$$\sigma_2(\omega) = \frac{e^2}{4\hbar d}\left(\frac{T_c}{T-T_c}\right)\frac{k_BT}{\hbar\omega}\left(1-e^{-\frac{\hbar\omega}{k_BT}}\right)\frac{\omega}{\omega_F}\int_0^\infty \frac{x^3dx}{(1+x^2)^2\left((1+x^2)^2+\frac{\omega^2}{\omega_F^2}\right)}$$

$$= \frac{e^2}{16\hbar d}\left(\frac{T_c}{T-T_c}\right)\frac{k_BT}{\hbar\omega}\left(1-e^{-\frac{\hbar\omega}{k_BT}}\right)\frac{\omega_F}{\omega}\left(-2+\pi\frac{\omega_F}{\omega}-2\frac{\omega_F}{\omega}\tan^{-1}\frac{\omega_F}{\omega}+\ell n\left(1+\frac{\omega^2}{\omega_F^2}\right)\right)$$

At low frequencies, $\omega << \omega_F$, these become

$$\sigma_1(\omega) = \frac{e^2}{16\hbar d}\left(\frac{T_c}{T-T_c}\right)\left(1-\frac{1}{6}\frac{\omega^2}{\omega_F^2}\right)$$

$$\sigma_2(\omega) = \frac{e^2}{16\hbar d}\left(\frac{T_c}{T-T_c}\right)\frac{\omega}{\omega_F}$$

while at high frequencies, $\hbar\omega >> kT$, they both are zero. The dc conductivity of the film calculated by this method is the same as the formula discovered by Aslamazov and Larkin from microscopic considerations,

$$\sigma_{D_C} = \frac{e^2}{16\hbar d}\left(\frac{T_c}{T-T_c}\right)$$

As T approaches T_c from above, it and the low frequency conductivity increase proportional to $\left(\frac{T_c}{T-T_c}\right)$ while the roll-off frequency, ω_F, decreases as $\left(\frac{T-T_c}{T_c}\right)$. The integrated area under the conductivity curve, then, remains roughly constant as the temperature is varied. The imaginary part of the conductivity is zero at zero frequency, has a peak

near ω_F and then decays to zero at high frequencies. Fig. 6 is a picture of these conductivities versus frequency for one of the films.

In zero dimensions one obtains the result that in first order there is no conductivity. For, if one takes $k_z = k_x = k_y = 0$

$$\sigma_1 = 0$$

$$\sigma_2 = 0$$

In second order take $k = \frac{\pi}{D}$ where D is the diameter of the particle, n = 3 since all three dimensions are the same, and $V = \frac{\pi}{6}D^3$ to find

$$\sigma_1 = \frac{9e^2}{2\hbar D}\left(\frac{T_c}{T-T_c}\right)\frac{k_B T}{\hbar\omega}\left(1-e^{-\frac{\hbar\omega}{k_B T}}\right)\frac{\pi^2\xi^4}{D^4}\;\frac{1}{\left(1+\frac{\pi^2\xi^2}{D^2}\right)\left(\left(1+\frac{\pi^2\xi^2}{D^2}\right)+\frac{\omega^2}{\omega_F{}^2}\right)}$$

but $\frac{\xi}{D} >> 1$

$$\sigma_1 = \frac{9e^2}{2\pi^4\hbar D}\left(\frac{T_c}{T-T_c}\right)\frac{k_B T}{\hbar\omega}\left(1-e^{-\frac{\hbar\omega}{k_B T}}\right)\frac{D^2}{\xi^2}\;\frac{1}{1+\frac{\omega^2 D^4}{\pi^4\omega_F{}^2\xi^4}}$$

Similarly,

$$\sigma_2 = \frac{9e^2}{2\hbar D}\left(\frac{T_c}{T-T_c}\right)\frac{k_B T}{\hbar\omega}\left(1-e^{-\frac{\hbar\omega}{k_B T}}\right)\frac{\omega}{\omega_F}\;\frac{\pi^2\xi^4}{D^4}\;\frac{1}{\left(1+\frac{\pi^2\xi^2}{D^2}\right)^2\left(\left(1+\frac{\pi^2\xi^2}{D}\right)^2+\frac{\omega^2}{\omega_F{}^2}\right)}$$

$$= \frac{e^2}{2\pi^4\hbar D}\left(\frac{T_c}{T-T_c}\right)\frac{k_B T}{\hbar\omega}\left(1-e^{-\frac{\hbar\omega}{k_B T}}\right)\frac{\omega}{\omega_F}\frac{D^4}{\xi^4}\;\frac{1}{1+\frac{\omega^2 D^4}{\pi\omega_F{}^2\xi^4}}$$

Now, $\xi = \xi_o(\frac{T_c}{T-T_c})^{\frac{1}{2}}$ and this just cancels the other factors of $(\frac{T-T_c}{T_c})$ everywhere since $\omega_F = \frac{16k_BT}{\pi\hbar}(\frac{T-T_c}{T_c})$. Then

$$\sigma_1 = \frac{9e^2}{2\pi^4\hbar D}\frac{k_BT}{\hbar\omega}(1-e^{-\frac{\hbar\omega}{k_BT}})\frac{D^2}{\xi_o^2}\frac{1}{1+(\frac{\hbar\omega}{16\pi k_BT})^2\frac{D^4}{\xi_o^4}}$$

$$\sigma_2 = \frac{9e^2}{32\pi^3\hbar D}(1-e^{-\frac{\hbar\omega}{k_BT}})\frac{D^4}{\xi_o^4}\frac{1}{1+(\frac{\hbar\omega}{16\pi k_BT})^2\frac{D^4}{\xi_o^4}}$$

At low frequencies, $\hbar\omega << k_BT$,

$$\sigma_1 = \frac{9e^2}{2\pi^4\hbar D}\frac{D^2}{\xi_o^2}(1-(\frac{\hbar\omega\ D^2}{16\pi k_BT\xi_o^2})^2)$$

$$\sigma_2 = \frac{9e^2}{32\pi^3\hbar D}\frac{D^4}{\xi_o^4}(\frac{\hbar\omega}{k_BT})$$

while at high frequencies, $\hbar\omega >> k_BT\ \frac{\xi_o^4}{D^4}$

$$\sigma_1 = \frac{9(16^2)e^2}{2\pi^2\hbar D}(\frac{k_BT}{\hbar\omega})^3\frac{\xi_o^2}{D^2}$$

$$\sigma_2 = \frac{9(16)^2e^2}{32\pi\hbar D}\frac{k_BT}{\hbar\omega}$$

The result is that fluctuation conductivities (in this model) of small particles are small and almost independent of temperature.

6. Fluctuations Below the Transition.

The above results are, as mentioned, only valid for temperatures above the transition temperature. They must be modified to calculate the extra conductivity below T_c. In this region there are fluctuations which cause an increase in the conductivity at finite frequencies above that due to the quasiparticles (e.g. above the BCS value). This extra conductivity dies out as the system is cooled away from the transition and the superconductivity becomes more stable. At the transition it should join smoothly with the results calculated above T_c.

Recall

$$\frac{\partial}{\partial t}\psi(\vec{x},t) = -\frac{8k_BT(T-T_c)}{\pi\hbar\, T_c}\{1 + \frac{\beta}{\alpha}|\psi|^2 - \frac{\hbar^2}{2m\alpha}\nabla\}\,\underline{\psi}(\vec{x},t)$$

with $\underline{\psi} = \underline{\psi}_o + \psi + i\phi$

Upon substituting for $\underline{\psi}$ this can be separated into two relaxation equations

$$\frac{\partial}{\partial t}\psi(\vec{x},t) = -\frac{8k_BT}{\pi\hbar}\left(\frac{T_c-T}{T_c}\right)\{2-\xi^2\nabla^2\}\psi(\vec{x},t)$$

$$\frac{\partial}{\partial t}\phi(\vec{x},t) = \frac{8k_BT}{\pi\hbar}\left(\frac{T_c-T}{T_c}\right)\xi^2\nabla^2\phi(\vec{x},t)$$

where $\xi^2 = \frac{\hbar^2}{2m(-\alpha)}$. Now, inserting the Fourier transforms of ψ and ϕ and solving

$$\chi(\vec{k},t) = \psi(\vec{k},0)\,e^{-\frac{\omega_F t}{2}(2+\xi^2k^2)}$$

$$\phi(\vec{k},t) = \phi(\vec{k},0)\,e^{-\frac{\omega_F t}{2}\xi^2k^2}$$

where, below T_c,

$$\omega_F = \frac{16 k_B T}{\pi \hbar} \left(\frac{T_c - T}{T_c}\right)$$

is the negative of ω_F above T_c. (Both, then, are positive.) The next step is to insert this into the current equation, which operation produces

$$\vec{J}(\vec{q},t) = \frac{e^* \hbar V}{2m^*} \vec{q}\, \psi_o \{\psi(\vec{q},t) + i\,\phi(\vec{q},t) - \psi^*(-\vec{q},t) + i\phi^*(-\vec{q},t)\}$$

$$+ \frac{e^* \hbar V}{2m^*} \sum_{\vec{k}} \vec{k}\, (\psi^*(\vec{k}-\frac{\vec{q}}{2},t) - i\,\phi^*(\vec{k}-\frac{\vec{q}}{2},t))(\psi(\vec{k}+\frac{\vec{q}}{2}) + i\,\phi(\vec{k}+\frac{\vec{q}}{2}))$$

If the current-current correlation function is calculated and Fourier transformed as before, the conductivities are found to be

$$\sigma_1(\omega) = \frac{4\pi e^2}{m} \psi_o\, \delta(\omega) + \frac{\pi e^2}{\hbar} \left(\frac{T_c}{T_c - T}\right) \frac{k_B T}{\hbar\omega} \left(1 - e^{-\frac{\hbar\omega}{k_B T}}\right) \frac{n\xi^2}{V} \times$$

$$\sum_k \frac{1+k^2\xi^2}{(2+k^2\xi^2)\left((1+k^2\xi^2)^2 + \frac{\omega^2}{\omega_F^2}\right)}$$

$$\sigma_2(\omega) = \frac{4e^2}{m} \psi_o \frac{1}{\omega} + \frac{\pi e^2}{\hbar} \left(\frac{T_c}{T_c - T}\right) \frac{k_B T}{\hbar\omega} \left(1 - e^{-\frac{\hbar\omega}{k_B T}}\right) \frac{n\xi^2}{V} \frac{\omega}{\omega_F} \times$$

$$\sum_k \frac{1}{(2+k^2\xi^2)\left((1+k^2\xi^2)^2 + \frac{\omega^2}{\omega_F^2}\right)}$$

The first term in each of these is just the London form for the

conductivity of a superconductor: the real part is infinite at $\omega = 0$ (an infinite dc conductivity) and zero everywhere else and the imaginary part goes as $1/\omega$. The second terms are the conductivities due to superconducting fluctuations and are the ones of interest here. The London terms will be replaced by the correct bulk conductivities from the BCS theory of superconductivity when they are needed.

Then the extra conductivity due to superconducting fluctuations is given in the second term of the equation above. In the usual way the sums are evaluated by replacing them with integrals in those directions in which the sample dimensions are much larger than the coherence length and the k = 0 term is taken in the other directions.

The formulae are, for thin films

$$\sigma_1 = \frac{e^2}{16\hbar d}\left(\frac{T_c}{T_c - T}\right)\frac{k_B T}{\hbar\omega}\left(1 - e^{-\frac{\hbar\omega}{k_B T}}\right)\frac{\frac{\omega}{\omega_F}}{1 + \frac{\omega^2}{\omega_F^2}}\left(\pi - 2\tan^{-1}\frac{\omega_F}{\omega} - \frac{\omega_F}{\omega}\ln\tfrac{1}{4}\left(1 + \frac{\omega^2}{\omega_F^2}\right)\right)$$

$$\sigma_2 = \frac{e}{16\hbar d}\left(\frac{T_c}{T_c - T}\right)\frac{k_B T}{\hbar\omega}\left(1 - e^{-\frac{\hbar\omega}{k_B T}}\right)\frac{1}{1 + \frac{\omega^2}{\omega_F}}\left(\pi - 2\tan^{-1}\frac{\omega_F}{\omega} + \frac{\omega}{\omega_F}\ln\tfrac{1}{4}\left(1 + \frac{\omega^2}{\omega_F^2}\right)\right)$$

These have similar form as above T_c. Fig. 7 is a picture of the conductivities below T_c.

For small particles

$$\sigma_1 = \frac{9e^2\xi^2(0)}{\hbar D^3}\left(\frac{T_c}{T-T_c}\right)^2\frac{k_BT}{\hbar\omega}\left(1-e^{-\frac{\hbar\omega}{k_BT}}\right)\frac{1}{1+\frac{\omega^2}{\omega_F^2}}$$

$$\sigma_2 = \frac{9e^2\xi^2(0)}{\hbar D^3}\left(\frac{T_c}{T-T_c}\right)^2\frac{k_BT}{\hbar\omega}\left(1-e^{-\frac{\hbar\omega}{k_BT}}\right)\frac{\frac{\omega}{\omega_F}}{1+\frac{\omega^2}{\omega_F^2}}$$

This is quite different than above T_c. Here the conductivities increase as $(T_c-T)^{-2}$ as the transition is approached.

7. Discussion of the Calculations.

Figures 6 and 7 show the behavior of the conductivities above and below T_c respectively for one of the films. Above T_c, the real part is equal to the dc conductivity at zero frequency and falls off to the normal state conductivity at high frequencies. The imaginary part is zero at zero frequency, rises to a peak and then falls off. Notice that the peak frequency is around twice ω_F. The characteristic frequency ω_F is indicated by a cross mark on each of the curves.

Below T_c the real part looks like the real part above T_c very near the transition and then goes over to the Mattis-Bardeen form as the temperature is decreased. There is little temperature dependence at low frequency. The imaginary part has the $1/\omega$ form with little temperature dependence near T_c, beginning to grow as the temperature falls.

The results obtained here, both for temperature above and below the transition are the same as those obtained by Schmidt

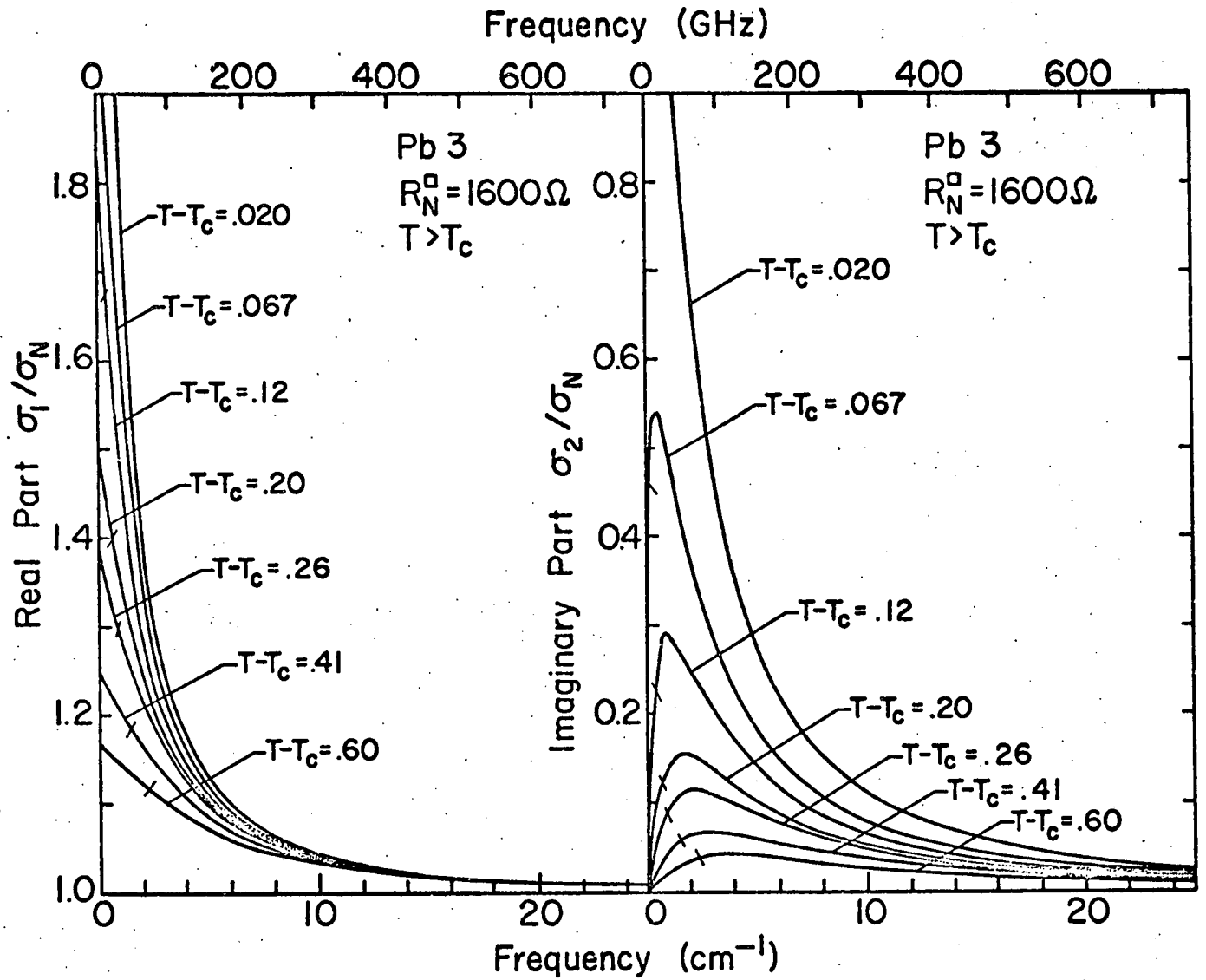

Fig. 6. Real and imaginary parts of the conductivity of a film above the transition temperature.

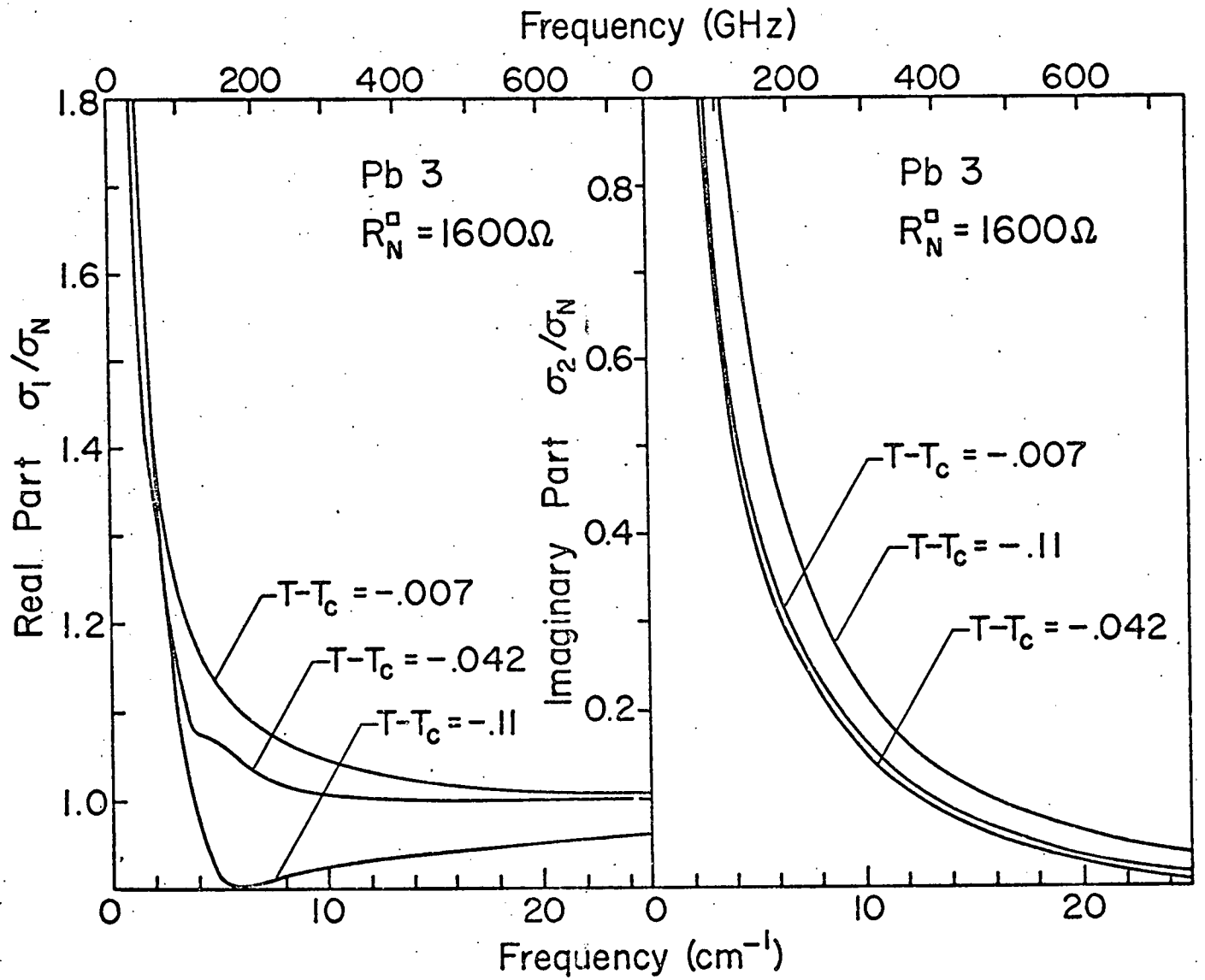

Figure 7. Real and imaginary parts of the conductivity of a film below the transition temperature.

if the frequencies are restricted to low enough values that

$$\frac{k_B T}{\hbar\omega}\left(1-e^{-\frac{\hbar\omega}{k_B T}}\right) = 1$$

This factor forces the extra conductivities to fall off to zero faster at high frequencies (by a factor of $1/\omega$) than do Schmidt's results.

There are some problems with this theory. It does not in general obey the Ferrell-Glover[45] sum rule on the real part of the conductivity (although the two dimensional case comes close to obeying it). In addition, in the very clean limit (long relaxation time) it does not give the correct results. If the relaxation time for collisions were longer than the decay time of the fluctuations then the current from the fluctuating regions should continue on in the normal metal for a time comparable to the relaxation time. Considerations of momentum conservation in the clean limit by Eilenberger[46] led to his calculating that the complex conductivity in the normal state should be multiplied by a factor $(1 + i\omega\tau)^{-2}$ where τ is the relaxation time due to collisions of the normal electrons.

This theory also becomes invalid very close to the transition temperature where it gives an arbitrary large value for the conductivities at finite temperatures. The factor $(\frac{T_c}{T-T_c})$ goes to infinity at T_c. Patton[47] has developed a microscopic theory of fluctuations which can be used right through the transition. In his theory $\frac{T_c}{T-T_c}$ is replaced everywhere that it appears by η, where η is the solution of a nonlinear equation which varies according

to the dimensionality of the sample. These are in two dimensions

$$\eta = \ln \frac{T}{T_c} + \eta_c(\ln \frac{\pi^2}{8\eta} - 1); \quad \eta_c = \frac{7/8\ \rho(3)}{4\pi^3 N_o \xi^2(0) d k_B T}$$

and in zero dimensions

$$\eta = \ln \frac{T}{T_c} + \frac{\eta_c^2}{\eta} \quad ; \quad \eta_c^2 = \frac{7/8\ \rho(3)}{\pi^2 N_o \Omega\ k_B T}$$

where

$$\xi_o^2 = \frac{\pi\hbar}{16 N_o e^2 k_B T}, \quad \rho(3) = 1.202 \quad \text{(Riemann Zeta Function)}$$

$$\Omega = V = \frac{\pi}{6} D^3$$

For $\eta > \eta_c$, these equations all become

$$\eta = \ln \frac{T}{T_c} \rightarrow \frac{T-T_c}{T_c} \quad \text{for } T-T_c \ll T_c$$

At $T = T_c$ the function $\eta(T)$ is non-zero so the conductivities do not diverge at the transition. The width of the critical region is defined by η_c. In two dimensions it reduces to

$$\eta_c = \frac{4.16e^2}{\pi^4\hbar} \frac{1}{\sigma_N d} = \frac{.043e^2}{\hbar} R_N^{\square} = 1.0 \times 10^{-5} \Omega^{-1} R_N^{\square}$$

slightly smaller than τ_o in the Aslamazov-Larkin formula

8. General Properties of the Films.

For the purpose of this experiment measurements were made on seven lead films and one blank substrate. The films were produced two by two in the evaporator insert and helium-three cooled detector system described in Chapter II. The films have been numbered Pb 1 through Pb 7. For the first six films, Pb 1

through Pb 6, the basket in the evaporator was charged with an alloy of lead (Cominco 99.999%) with 4 At. % bismuth (Cominco 99.9999%). The purpose of the bismuth was to decrease the normal state conductivity. This was felt to be unnecessary so Pb 7 was made from the pure lead alone.

Various parameters useful in discussing the films are displayed in Table I. The temperature at which the films were deposited is shown in the first line. This is also the highest temperature to which the films were submitted until the end of the measurements and so indicates the state of annealing of the films. As the experiments progressed and the experimenter became more adept at the use of the apparatus this temperature wandered around. It was always less than 50^{o} K. The major anneal in an amorphous film should occur near the Debye temperature which in lead is 96^{o} K. In fact there is a big change in resistance in these films between 80^{o} K and 100^{o} K. Most of the films became discontinuous at these temperatures and all increased their resistance. Strongin et al[48] have measured the resistance of several lead films on different substrates and find that some annealing begins even at 7^{o} K, the transition temperature and continues as the temperature is increased. By evaporating the films at a higher temperature than ever reached during repeated passes through the transition region any problems due to changing residual resistance during the experiment were avoided. At the end of the infrared experiments the resistance was generally measured as the films were warmed up to nitrogen temperatures. The resistance would increase slightly, indicating that there was no major annealing going on.

Table 1

Various Film Parameters

Film number		1	2	3	4	5	6	7
Deposition temperature	^{o}K	15	20	40	50	26	30	25
Evaporation time	min	1½	5	3	3	2	3	3
Evaporation pressure	Torr	$1x10^{-6}$	$1x10^{-6}$	$9x10^{-7}$	$2x10^{-6}$	$7x10^{-7}$	$7x10^{-7}$	$3x10^{-6}$
DC Square resistance	$R_N^{\square}$ Ω	442	100	5470	22,100	3010	910	1430
FIR sheet resistance	$R_N^{\square}(\omega)$	300	80	1600	--	820	440	1100
FIR Transmission	T_n/T_q	.5	.1	.88	1.0	.76	.61	.81
Thickness	d Å	22	44	10	--	14	20	12,7
Transition temperature	T_c, ^{o}k	6.92	--	6.423	6.64	6.914	6.844	6.660
Aslamazov Larkin parameter	τ_o Ω^{-1}	--	--	$.98x10^{-5}$	--	$.96x10^{-5}$	$.89x10^{-5}$	$.89x10^{-5}$
Patton parameter	η_c	--	--	$.62x10^{-6}$	--	$.60x10^{-6}$	$.54x10^{-6}$	$.54x10^{-6}$
Critical width	$\tau_o R_N^{\square} T_c$	--	--	.100	--	.054	.026	.064

The next two rows give the time that the evaporation took and the pressure at the beginning of the evaporation. This pressure was measured by the ionization gauge at the top of the evaporator.

The square or sheet resistance in the normal state is the major parameter of the films. It is given in the next two rows of the table. The dc square resistance is just

$$R_N^{\square} = \frac{1}{\sigma_o d} = R_N \frac{w}{L}$$

where σ_o is the zero frequency electrical conductivity of the film R_N the measured residual resistance and d, L, and w are its thickness, length, and width respectively. The conductivity and thickness are not easy to measure in independent ways for a thin sample but the square resistance can be gotten by multiplying the measured residual resistance by the ratio of width to length. Another and perhaps more reliable measure of the square resistance can come from comparing the infrared transmission of the films to that of a blank substrate. The formulas for calculating this are given in Appendix B, section 5. The transmission versus $R_N^{\square}$ is shown in Fig. B6. The infrared measure of $R_N^{\square}$ is equal to the dc value when $\omega\tau << 1$. This is surely the case for these very thin films. The far infrared transmission ratios from which the square resistances were calculated are shown in the next row.

Inspection of Table 1 shows that the far infrared values for $R_N^{\square}$ are in some cases almost a factor of four smaller than the dc values, the deviations being the largest in the thinner films. I would like now to argue that the far infrared value is by far

the more accurate. In the first place the geometry of the film, as shown in Figure 8 at right, was far from ideal. It was wider than it was long and it had curved sides whose contribution to the conductivity is hard to estimate. Any decrease in the effective width of the film would lower its square resistance. Secondly, the far infrared radiation tends to average over point imperfections in the film. The infrared radiation measures the average conductivity in an area approximately the wavelength squared. Because of this it is insensitive to small holes or cracks in the film. Similarly, it is insensitive to a few scratches in the substrate which, if across the film, would seriously affect the dc resistance.

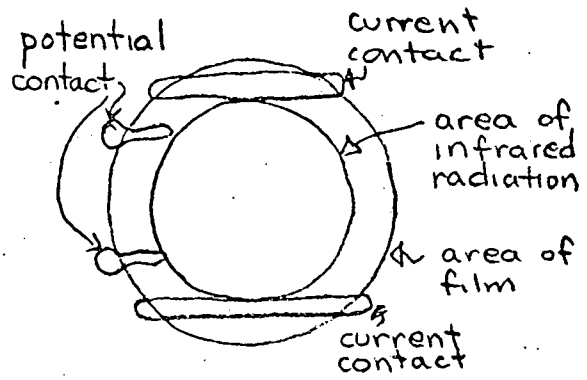

Figure 8. Film Geometry

The thickness can be estimated in two ways.[49] For a very thin film one would expect the mean free path to be [50]

$$\ell = \frac{8}{3} d$$

assuming diffuse scattering at the surface. Then the conductivity is

$$\sigma = \frac{8ne^2d}{3mV_F}$$

and the square resistance is

$$R_N^{\square} = \frac{3mV_F}{8ne^2d^2}$$

values for $\frac{mV_F}{ne^2}$ have been published by Cody and Miller[51] (for lead

$\frac{mV_F}{ne^2} = 1.5 \times 10^{-11}\ \Omega\ cm^2$) so the thickness can be calculated from $R_N^{\square}$.

A check on this can be obtained for those films that exhibit temperature dependence in the resistance between the lowest temperatures and liquid nitrogen temperature. Then

$$R^{\square}(T) - R_N^{\square} = \rho(T)\ \frac{1}{d}$$

where $\rho(T)$ is the bulk resistivity at the temperature T. In the case of Pb 7, the second value given for the thickness came from this calculation. For the others only the first estimate was available.

The last four items in the table, transition temperature, Aslamazov-Larkin parameter critical width, and Patton parameter were obtained from analysis of the dc resistive transition as discussed in the next section.

Four of the films, Pb 3, Pb 5, Pb 6, and Pb 7, produced successful simultaneous measurements of far infrared transmission in the fluctuation region, dc resistance, and temperature. The experiments on three of the films were unsuccessful for various reasons: The detector system was unacceptably noisy during the run on Pb 1 and Pb 2. In addition, Pb 2 was quite thick so that its transmission was too low. Pb 4, on the other hand, was too thin; it was almost perfectly transparent. Qualitative fluctuation effects were observed in both Pb 1 and Pb 4, but a detailed comparison with theory was not made. The films which did not produce successful fluctuation measurements are included in this

section for the sake of completeness; they will not be mentioned again.

9. The DC Conductivity.

In Fig. 9 is plotted the resistivity ratio, $\frac{R}{R_N}$, of the films versus temperature. As can be seen, the resistive transition is broad; the films exhibit considerable extra conductivity; and there is something of a tail in the resistance below the transition. It is the presence of this tail (whether a real or bogus phenomenon) that makes determination of the transition temperature difficult. Not immediately evident from the figure, but true nonetheless, is that the transition is narrower by about 40% in all of these films than would be predicted by the Aslamazov-Larkin formula

$$\frac{R_N}{R} = \frac{\sigma}{\sigma_N} = 1 + \frac{\tau_o}{\sigma_N d}\left(\frac{T_c}{T-T_c}\right) \quad ; \quad \tau_o = \frac{e}{16\hbar} = 1.5\times10^{-5}\ \Omega^{-1}, \frac{1}{\sigma_N d} = R_N\square$$

It is thus necessary to determine an empirical value for the constant τ_o applicable to these films. This requires the extraction of two parameters (T_c and τ_o) from one set of data. Here is how it is done. By eye the dc resistance is extrapolated to zero according to $R\sim(T-T_c)$. This eliminates the tail and gives a first estimate for T_c. Using this T_c the constant τ_o is calculated for each of the resistance points. This gives several values for τ_o. Those for temperatures rather far from T_c are the least sensitive to variations in it and their average is used to calculate a new value for T_c. Continuing the process, requiring both reasonableness and consistency in the results quickly leads to good estimates in both T_c and τ_o. These

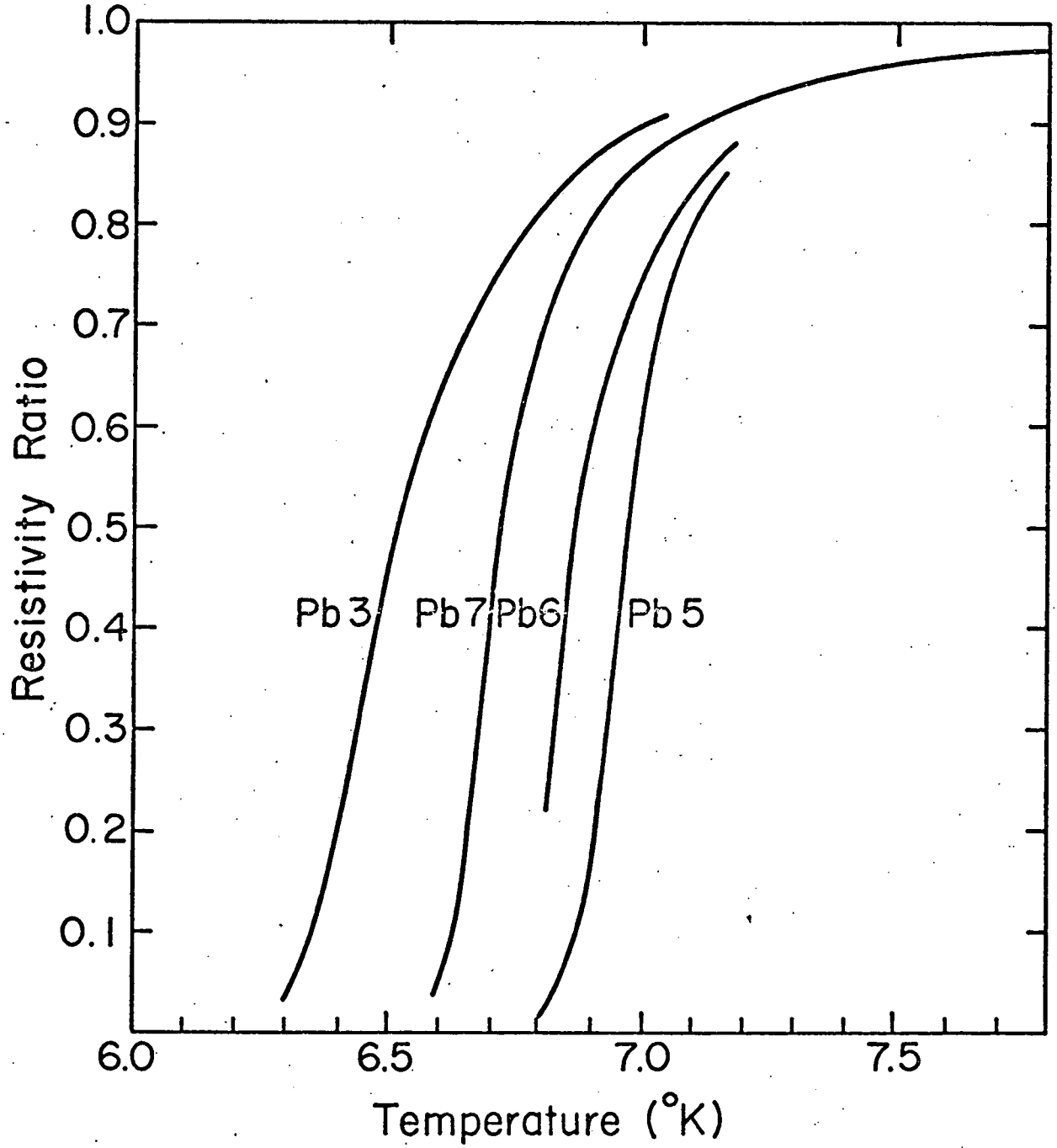

Fig. 9. Resistive Transition of the films.

are given in the ninth and tenth rows of the table. The final value for T_c was between 1 and 30 millidegrees K below the first graphical estimate, not a major change. All of the films had values for τ_o within 5% of the average $.93 \times 10^{-5}$.

In Fig. 10, then, is plotted the conductivity ratio, $\frac{\sigma}{\sigma_N}$, versus distance from the transition, $T-T_c$. The solid line shows the calculated conductivity from the Aslamazov-Larkin formula (using the smaller value of τ_o). The dotted line shows the result of replacing $\frac{T-T_c}{T_c}$ in this equation by Patton's η. The value for η_c that was necessary to fit the data was in all cases $.06\tau_o$. This is shown in the eleventh row of the table. This is an order of magnitude less than calculated above but using the larger value produced far too small a value for the conductivity ratio (less than one at T_c) in all of the films. It should be emphasized that η is never zero at finite temperatures. Hence the conductivity in the films due to fluctuations is never infinite.

There is an unfortunate amount of scatter in the conductivity points but it appears that Patton's expression gives a better fit to the data. Most of the errors in the data are due to uncertainties in measuring the temperature. Temperature errors are always $.01^{\circ}$ K. In the case of Pb 6 they are larger than this because the substrate was poorly anchored to the copper block on which was mounted the heater and thermometers. This weak thermal connection allowed the film temperature to drift somewhat as the infrared radiation heated it and the exchange gas coupling to the 4.2° helium bath cooled it. This thermal contact was a

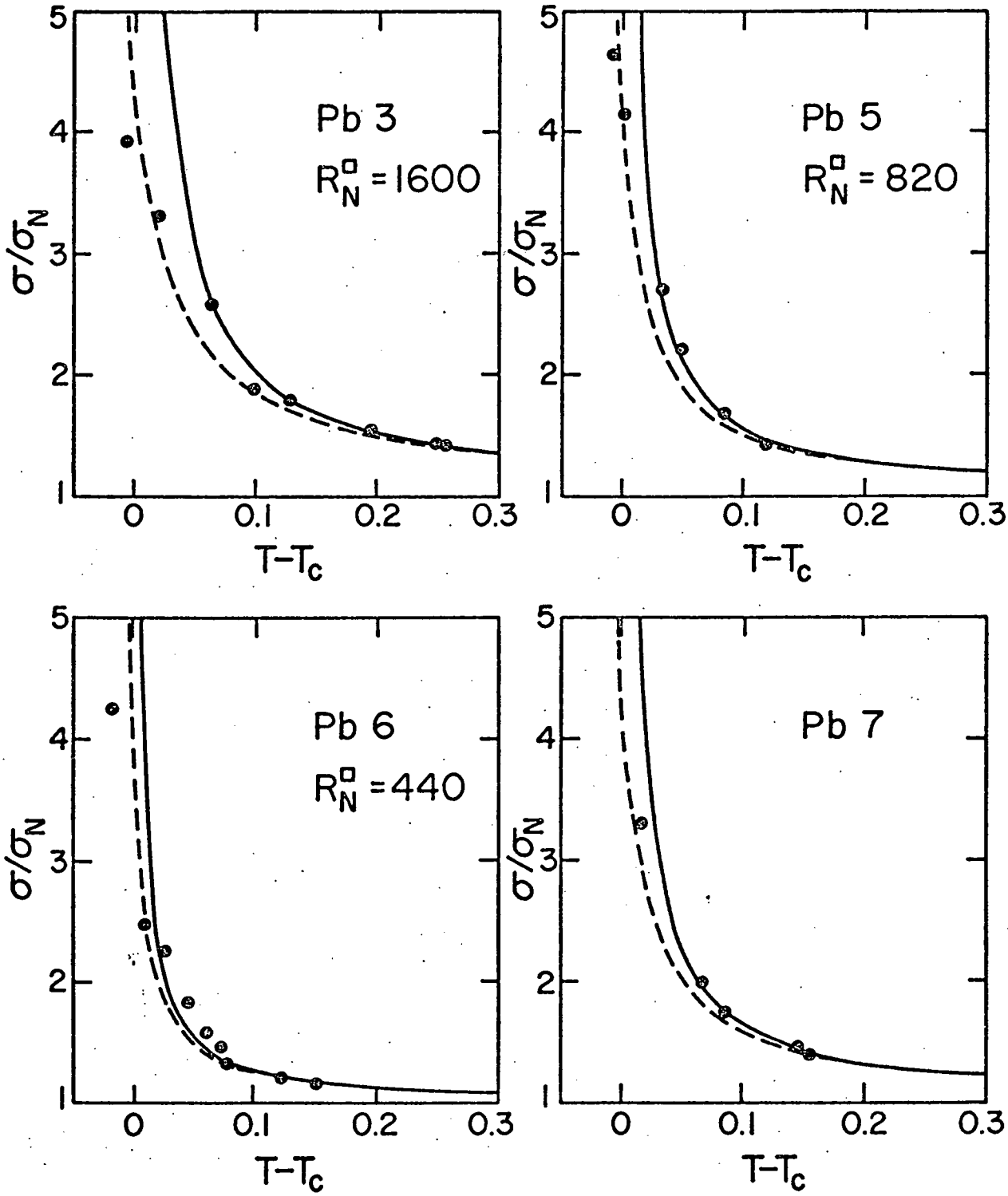

Fig. 10. The total conductivity of the films versus temperature. The temperature is measured from the transition temperature. The solid line is the Aslamazov-Larkin equation; the dashed line is from Patton's theory.

somewhat smaller problem in the case of Pb 3 and Pb 6 and was no problem at all in the case of Pb 7. At the bottom of the table is the critical width. This is $\Delta T = \tau_o R_N^{\square} T_c$

All of the dc resistance measurements were made using the standard four probe techniques. The current was provided by dry cells and measured as a voltage across an external precision resistor having a resistance near that of the film. The voltages were all measured on a Rubicon portable potentiometer. The current used was typically 4 microamperes.

10. Far Infrared Transmission Data.

In the next several figures are presented the results of the far infrared measurements. The data are presented in two ways: as transmission ratio versus frequency at a given temperature or as transmission ratio versus temperature at a given frequency. In the first case the various temperatures are the experimental temperatures; in the second the frequencies are chosen at even intervals. The measurements were, of course, all made as a function of frequency at constant temperature using the far infrared techniques described in Chapter II. The interferograms were all of low resolution and as many as twelve of them were averaged to produce one spectrum.

The following system was used to take the data. After the evaporation (see Chapter II) the films were cooled to 4.2^{o} K by adding exchange gas to the evaporator section. After a couple of interferograms had been recorded at this temperature, the samples

were warmed up through the transition to around 9.5° K, where three or four normal state runs were made. Then the temperature was reduced until the film resistance began to drop and the first fluctuation régime data were taken. The temperature was gradually reduced through the transition, with three interferograms taken at each temperature. Between five and ten temperature points were taken for each film. The temperature was controlled by an Artronix temperature controller which has the capability of maintaining the temperature within 20 millidegrees during the time it took to do the interferogram. The film resistance was monitored constantly throughout the run and fine adjustments to the temperature controller were made manually to maintain the resistance at the desired value. The film resistance is a very sensitive thermometer in the transition region. In this way the drift while an interferrogram was taken could be held to ±.005° k. After the lowest desired temperature had been done the temperature was raised to the normal state value again and three or four interferograms were recorded. From there the temperature was lowered to the lowest value and the transition region gone through in the increasing temperature direction with the film resistance used to regain the desired temperature. Next came the normal state measurements again and then, if time permitted, came another pass through the transition. The last interferograms were always taken at the normal state temperature. After the measurements were made on one film, the other film was rotated into the beam and the outer liquid helium container (the 4.2° bath)

was refilled. The entire sequence was repeated on the second film.

In all of the figures the vertical axis is the transmission ratio, $\frac{\mathcal{T}_F}{\mathcal{T}_N}$ and the horizontal axis is either the frequency (in cm^{-1} along the bottom and hertz along the top) or temperature difference, $T-T_c$, (in ^oK). The experimental data are shown as points and the theoretical curves as solid lines. Now, the transmission curves have all been shifted vertically so as to separate them; the places where the experimental curves all cross one are indicated by the figures 1 on the left-hand side of the plots and also by the dashed horizontal line on each side of the data. On the left hand side is a scale or sort of ruler which shows the magnitude of the changes in the transmission. Each division corresponds to a one percent change in the transmission.

In all of the plots of $\frac{\mathcal{T}_F}{\mathcal{T}_N}$ versus frequency the theoretical curves have been slid upwards by a small amount in order to make them fall along the experimental points. By fall along I mean fit with the experimental points in the six to eight wave number range. The theoretical curves never cross one for $T>T_c$ while the experimental curves all do. The amount of the required upward shift varies with temperature, being .6% at the high temperatures and 1.4% at the low temperatures.

There are error bars on representative points in all of the figures. These are calculated from the standard deviation of the spectrum and the value of the spectrum at the given frequency. Because of the low pass filter used to give a high frequency

cutoff, the last few points of the spectrum are always nearly zero and their standard deviation can be computed to give a measure of the noise.

The conductivities used to calculate the theoretical curves are found by adding the two dimensional fluctuation conductivities calculated above and the appropriate regular conductivity: the normal conductivity σ_N, above the transition and the BCS conductivity, $\sigma_1 + \sigma_2$, below it. As discussed in Appendix B the normal state conductivity has a real part equal to the dc conductivity and an imaginary part equal to zero. The superconducting state conductivity can be calculated from the tables published by Miller.[52] These give the conductivities, $\frac{\sigma_1}{\sigma_N}$ and $\frac{\sigma_2}{\sigma_N}$, as a function of frequency. For the four highest temperatures, these conductivities are shown plotted in Figures B1 and B2. From these, plots of conductivities versus temperature for integer wave number were prepared and the numbers for calculating the total conductivities were taken from these curves.

The formulae used to calculate these curves are listed below. The total conductivities for $T>T_c$ are

$$\frac{\sigma_1}{\sigma_N} = 1 + \tau_o R_N \left(\frac{T_c}{T-T_c}\right) \frac{k_B T}{\hbar\omega} \left(1-e^{-\frac{\hbar\omega}{k_B T}}\right) \frac{\omega_F}{\omega} \left(\pi - 2\tan^{-1}\frac{\omega_F}{\omega} - \frac{\omega_F}{\omega} \ln\left(1+\frac{\omega^2}{\omega_F^2}\right)\right)$$

$$\frac{\sigma_2}{\sigma_N} = \tau_o R_N \left(\frac{T_c}{T-T_c}\right) \frac{k_B T}{\hbar\omega} \left(1-e^{-\frac{\hbar\omega}{k_B T}}\right) \frac{\omega_F}{\omega} \left(-2 + \pi\frac{\omega_F}{\omega} - 2\frac{\omega_F}{\omega}\tan^{-1}\frac{\omega_F}{\omega} + \ln\left(1+\frac{\omega^2}{\omega_F^2}\right)\right)$$

for $T<T_c$

$$\frac{\sigma_1}{\sigma_N} = \frac{\sigma_1^{MB}}{\sigma_N} + \tau_o R_N \left(\frac{T_c}{T_c - T}\right) \frac{k_B T}{\hbar\omega}\left(1 - e^{-\frac{\hbar\omega}{k_B T}}\right) \frac{\frac{\omega_F}{\omega}}{1 + \frac{\omega^2}{\omega_F^2}} \times$$

$$\times \left(\pi - 2\tan^{-1}\left(\frac{\omega_F}{\omega}\right) - \frac{\omega_F}{\omega} \ln \tfrac{1}{4}\left(1 + \frac{\omega^2}{\omega_F^2}\right)\right)$$

$$\frac{\sigma_2}{\sigma_N} = \frac{\sigma_2^{MB}}{\sigma_N} + \tau_o R_N \left(\frac{T_c}{T_c - T}\right) \frac{k_B T}{\hbar\omega}\left(1 - e^{-\frac{\hbar\omega}{k_B T}}\right) \frac{1}{1 + \frac{\omega^2}{\omega_F^2}} \times$$

$$\times \left(\pi - 2\tan^{-1}\frac{\omega_F}{\omega} + \frac{\omega}{\omega_F} \ln \tfrac{1}{4}\left(1 + \frac{\omega^2}{\omega_F^2}\right)\right)$$

The transmission and reflection of the film (the first surface coefficients) are

$$\mathcal{T}_1 = \frac{4n}{(n+1+Z_o\sigma_1 d)^2 + (Z_o\sigma_1 d)^2}$$

$$\mathcal{R}_1 = \frac{(n-1+Z_o\sigma_1 d)^2 + (Z_o\sigma_2 d)^2}{(n+1+Z_o\sigma_1 d)^2 + (Z_o\sigma_2 d)^2}$$

The transmission and reflection coefficients of the rear surface are

$$\mathcal{T}_2 = \frac{4n}{(n+1)^2}$$

$$\mathcal{R}_2 = \left(\frac{n-1}{n+1}\right)^2$$

The transmission of the entire substrate assembly is

$$\mathcal{T}^A = \frac{\mathcal{T}_1 \mathcal{T}_2}{1-\mathcal{R}_1\mathcal{R}_2}$$

where n is the index of refraction of the quartz (n= 2.11), z_o is the impedance of free space (z_o = 377Ω) and

$$\omega_F = \begin{cases} \frac{16k_BT}{\pi\hbar} \frac{T-T_c}{T_c} & T>T_c \\ \frac{16k_BT}{\pi\hbar} \frac{T_c-T}{T_c} & T<T_c \end{cases}$$

The theoretical curves were generated from these equations using a simple BASIC language program on a PDP 11 computer.

Figure 11 presents the results for Pb 3 as a function of frequency. Pb 3 was the thinnest film ($R_N^{\square}$ = 1600Ω) and had the most different temperatures. With the exception of the upward shift, there has been no fitting of the data. The values of τ_o and T_c used are those from the dc resistance measurements. The fit between the experimental points and the theoretical calculations is close to within the noise.

The four curves that extend to higher frequencies are the result of overlapping measurements with three different high frequency limits or cutoffs, taking the average in the overlap region. The cutoffs were 50, 21, and 14 cm^{-1}. The numerical values of the transmission ratios differed by no more than .2% in the overlap region. The 21 cm^{-1} cutoff runs were used as a standard and the others were fitted to them. The curves that

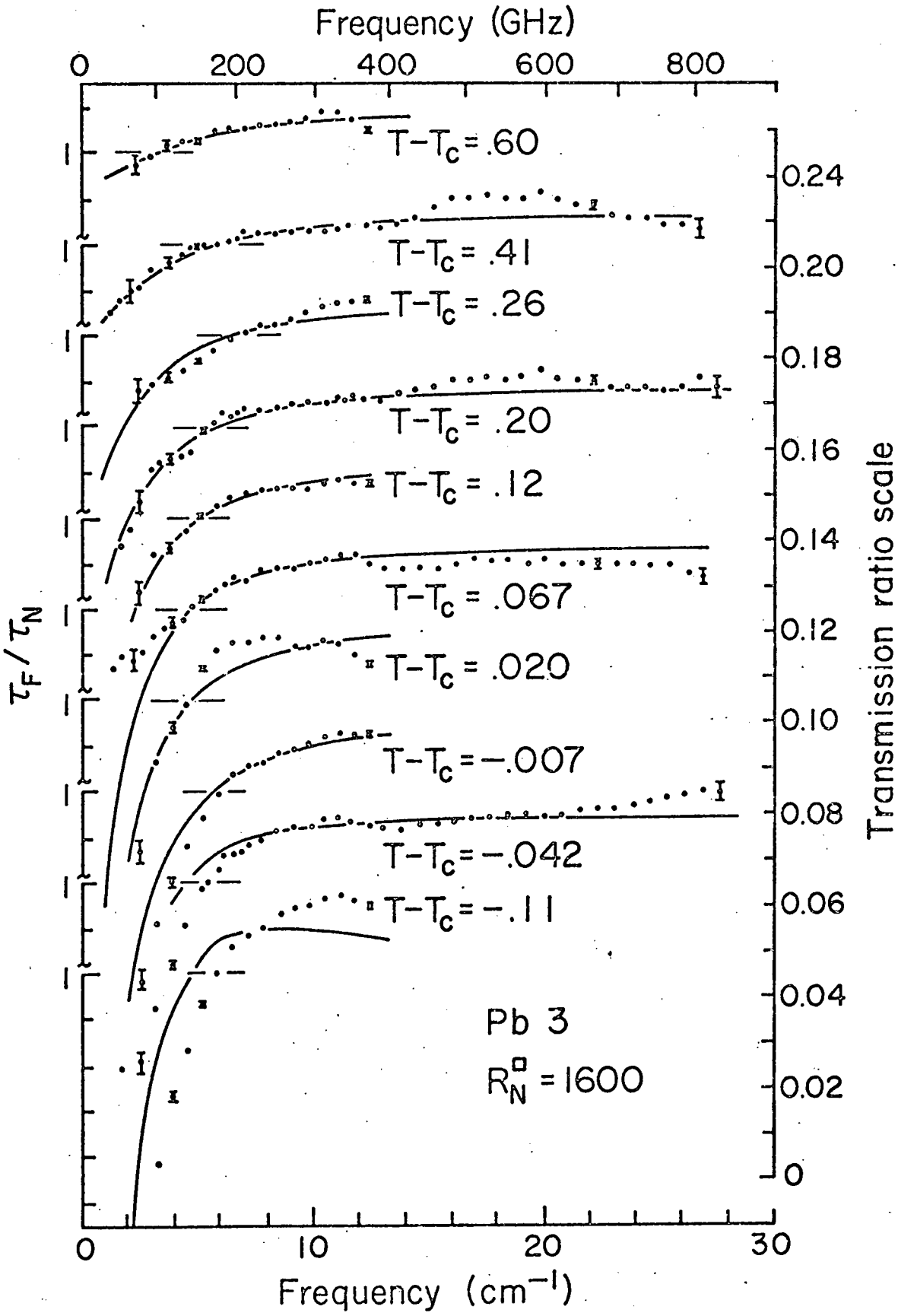

Fig. 11. Transmission ratio versus frequency for Pb 3.

stop at the lower frequencies were measured only with the 21 cm^{-1} cutoff.

Figure 12 shows the transmission data for the same film plotted against $T-T_c$. The reader should first direct his attention to the lowest curve. This shows the transmission at 12 cm^{-1}. The experimental points are taken unchanged from the transmission data in Figure 11. As can be seen there is some scatter, but the primary feature is a gradual decline in transmission as the temperature is increased. To eliminate this shift in baseline, all of the high frequency ends of the data were set to the theoretical value at 12 cm^{-1} for the appropriate temperature. Then the points at the other frequencies are calculated using this value of the 12 cm^{-1} transmission ratio. That is, the points at the other frequencies are found by subtracting from their value in Figure 11 their value at 12 cm^{-1} and then adding the theoretical value at 12 cm^{-1}

$$\frac{\mathcal{T}_F^{ergs}(\omega,T)}{\mathcal{T}_{N'}} = \frac{\mathcal{T}_F^{exp}(\omega,T)}{\mathcal{T}_N} - \frac{\mathcal{T}_F^{exp}(12\ cm^{-1}T)}{\mathcal{T}_N} + \frac{\mathcal{T}_F^{theo}(12\ cm^{-1},T)}{\mathcal{T}_N}$$

This is equivalent to a renormalization of the normal state transmission data. It appears from all this that either the detector sensitivity or the transmission of the sample assembly is affected by near 1%/^oK, by changing the sample temperature.

After this correction, the agreement between the experimental points and the theoretical line is adequate (±1.2%) above T_c if not as satisfying as in the plots of transmission ratio versus frequency. The reason for this is that in the former the data

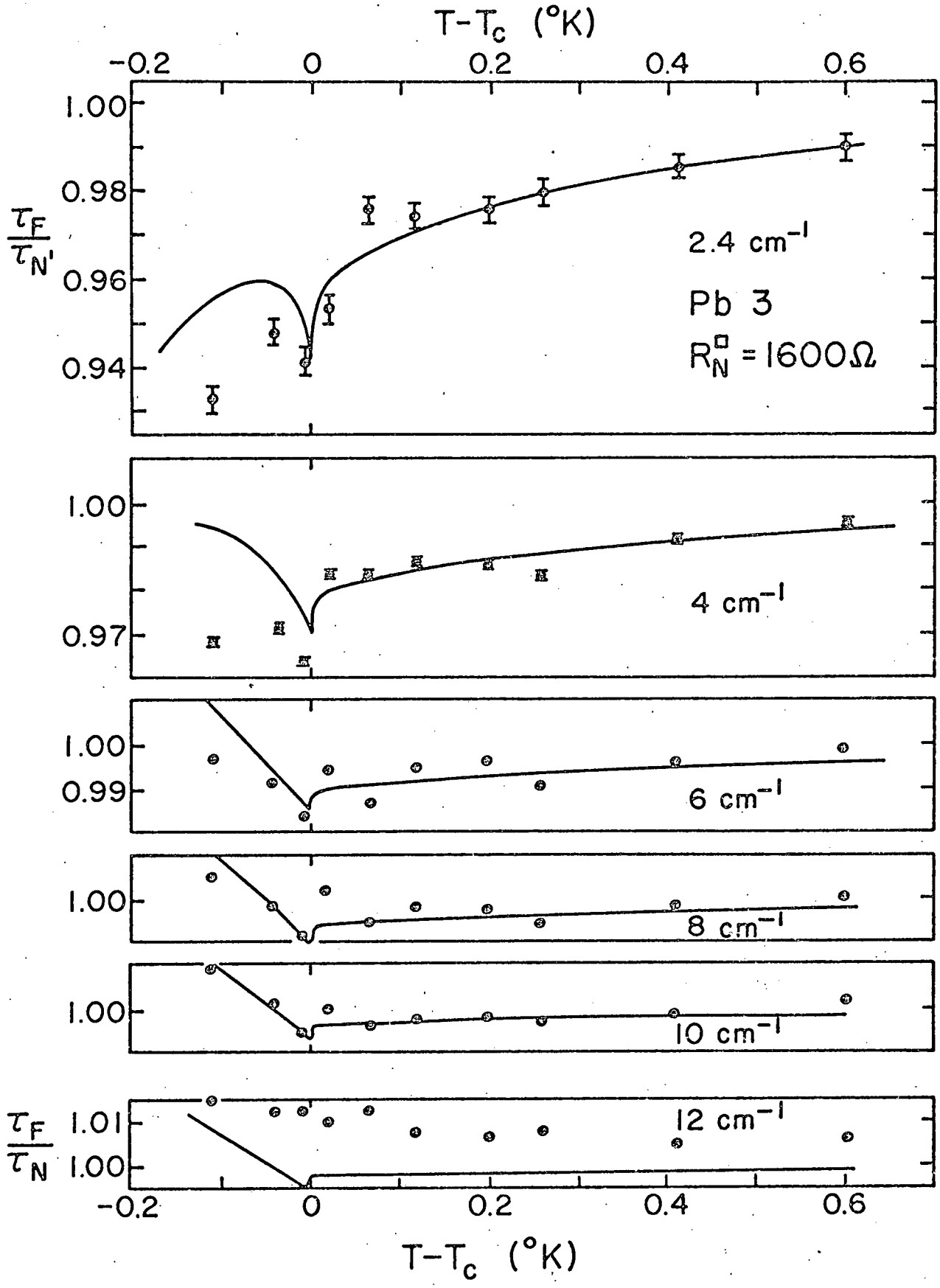

Fig. 12. Transmission ratio versus temperature for Pb 3.

points are from a single intensity ratio, whereas in the latter they are each from a different one. In general, the larger deviations appear at the same temperature difference, and are probably systematic on the normalization. The spike at T_c is a breakdown of the theory and should be ignored.

The next three figures, Figures 13, 14 and 15, show the transmission data for the other films, Pb 5, Pb 6, and Pb 7 respectively. In Pb 5 all of the runs were made at temperatures above the transition temperature and with an 18 cm^{-1} high frequency cutoff. Pb 6 was the thickest film on which data were taken. All of the temperatures were above T_c again although the error in the lowest temperature run ($T-T_c = .001^o$ K) is $.005^o$ K at least. It could be either above or below T_c. Both 18 cm^{-1} and 66 cm^{-1} cutoff runs were made. Pb 7 was the only all lead film. There was no bismuth in the evaporant. One of the interferograms was recorded for temperatures below T_c and both 16 and 40 cm^{-1} cutoffs were used.

11. Discussion of the Data.

There are some seven questions about these experiments which might be raised at this point. I will discuss them one at a time.

Why are the experimental points invariably higher than the theoretical curves and is this serious?

There are three possibilities why this might occur. The Ferrell-Glover[45] sum rule, which requires that the integral over all frequency of the real part of the conductivity be independent of the phase transition, is not satisfied by the

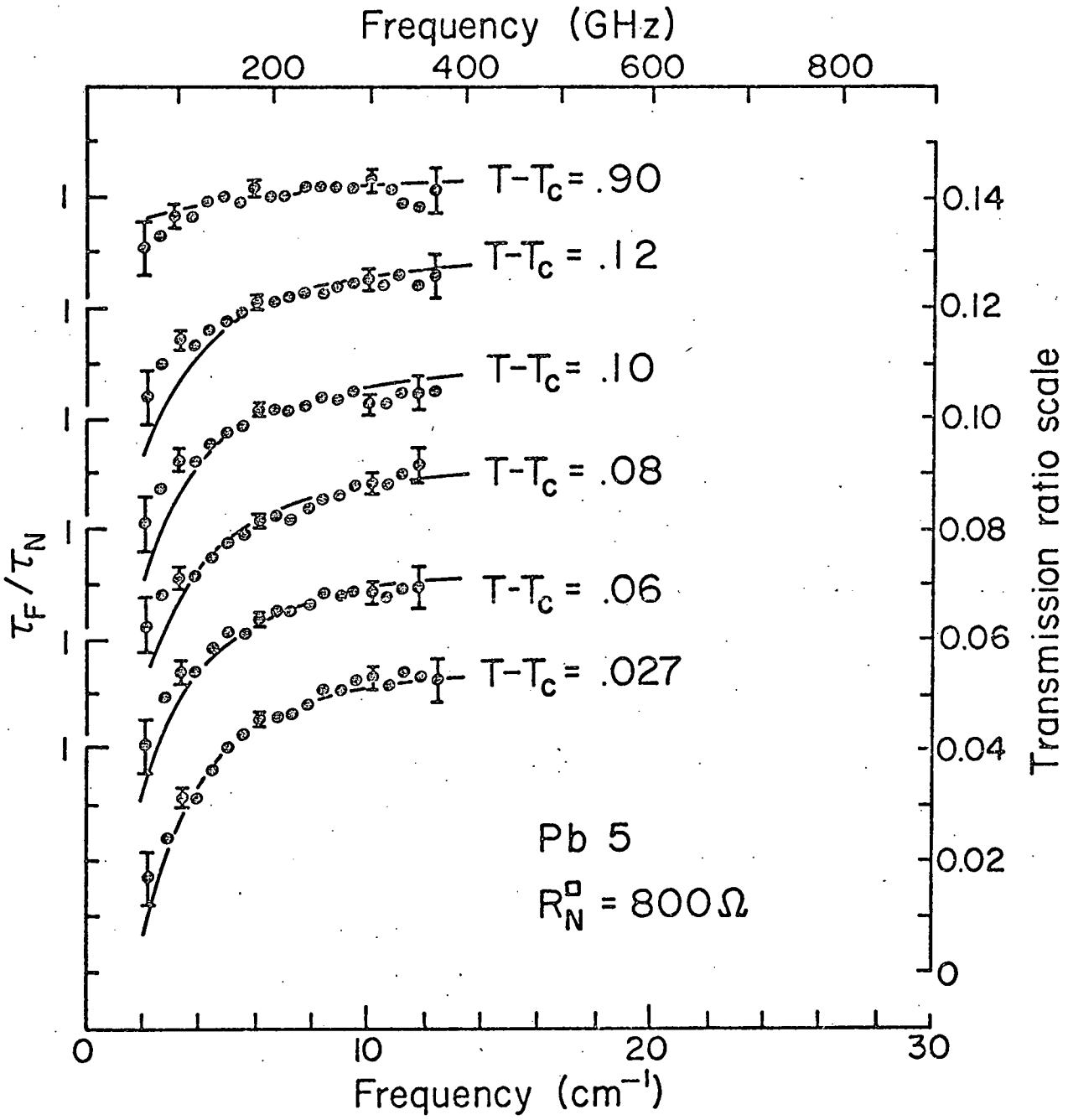

Figure 13. Transmission ratio versus frequency for Pb 5.

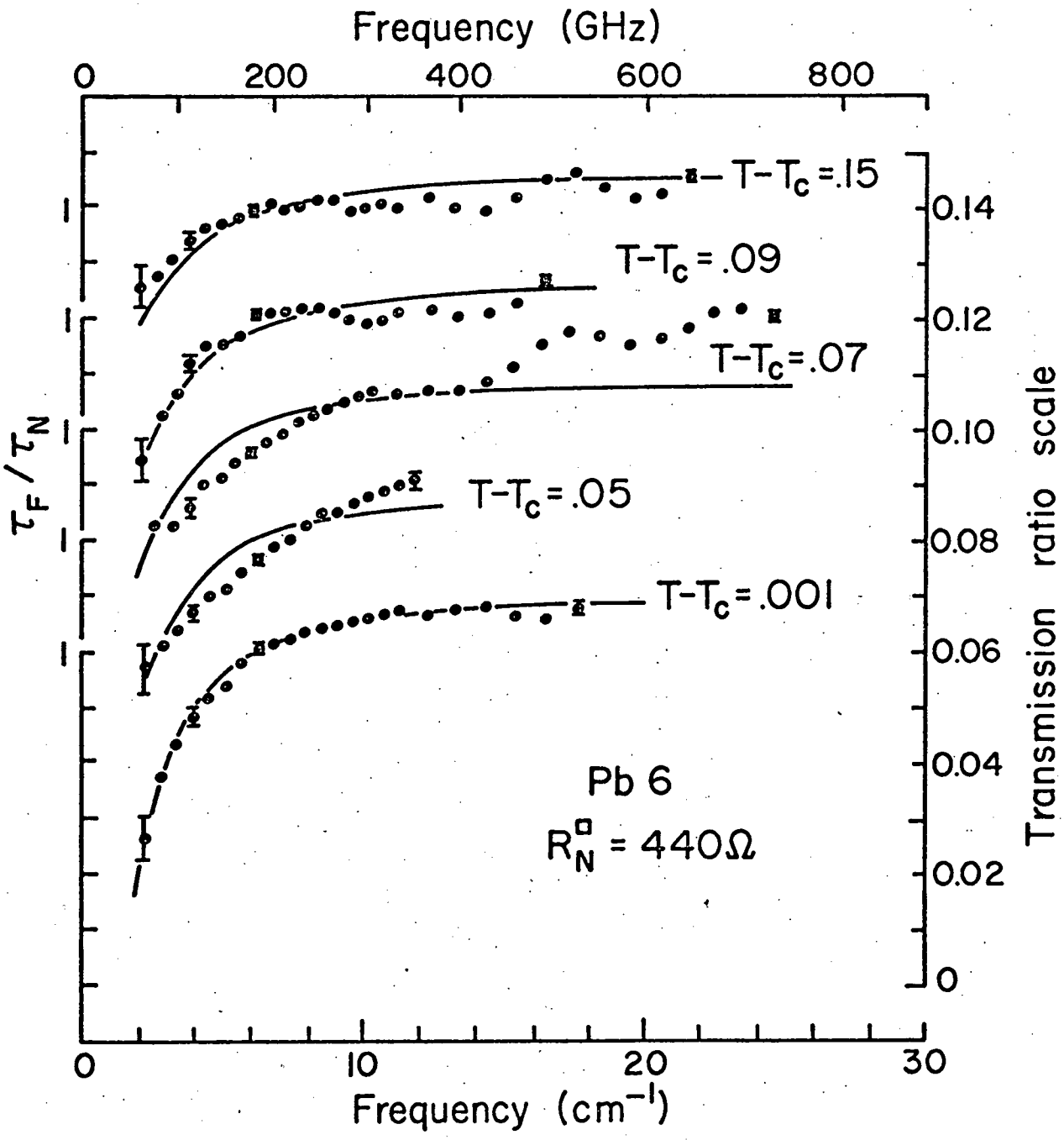

Figure 14. Transmission ratio versus frequency for Pb 6.

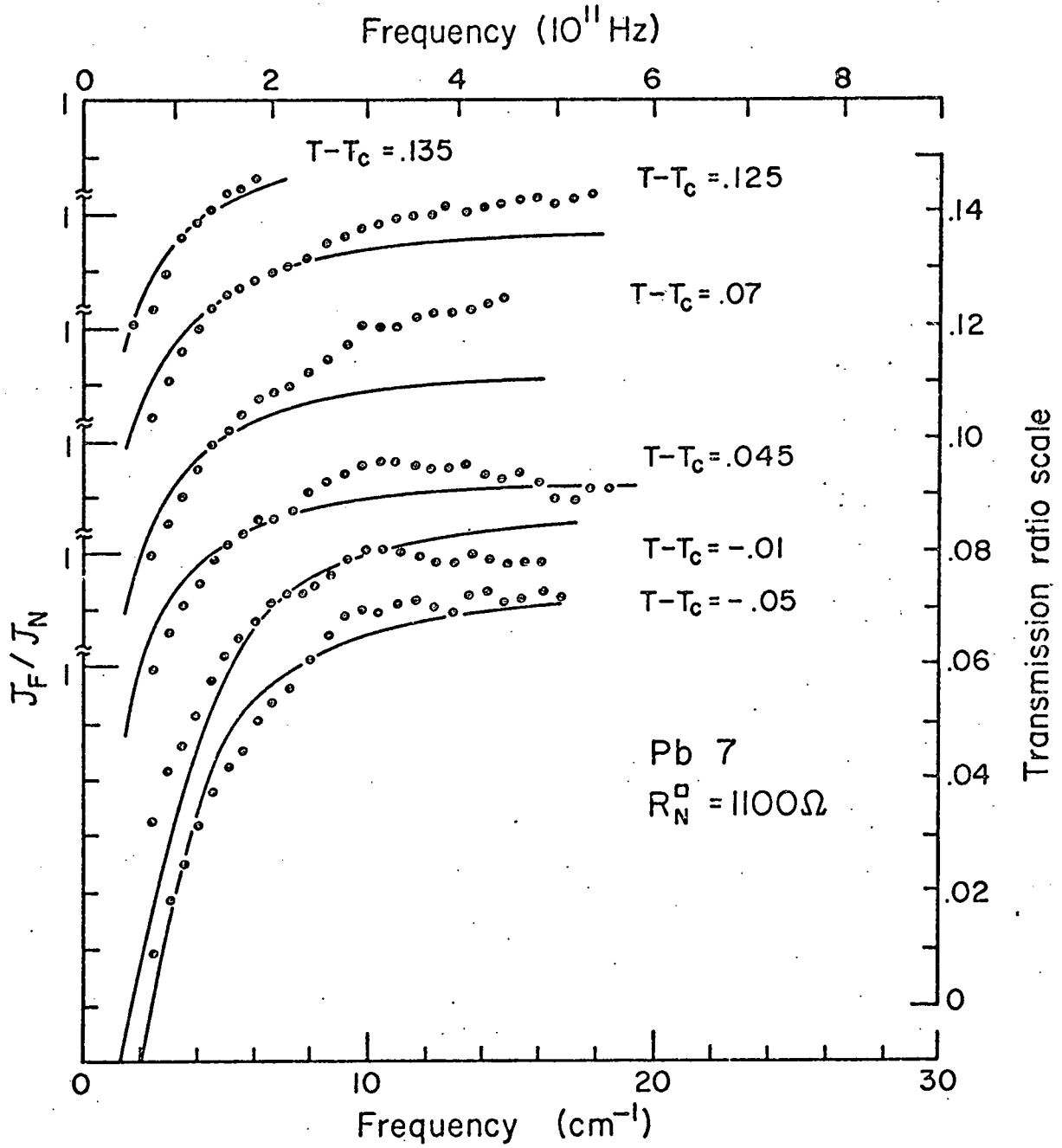

Fig. 15. Transmission ratio versus frequency for Pb 7.

conductivities used here. The area under the conductivity curve grows as the transition is approached and then drops again below it. (See Figures 6 and 7) The easiest way to fix this up would be to have the conductivity ratio drop to slightly below one and then rise slowly back to one. If this happened the transmission ratios would be greater than one. Another possibility is that the normal state transmission as measured at 9.5^{o} K is not the same as that at the transition temperature (determined, say, by applying a magnetic field). If the conductivity were to increase slightly upon reducing the temperature the normal state transmission would be lowered. The other possibility is that when the sample is warmed up the detector is also warmed up. This would reduce its sensitivity and thereby reduce the measured normal state transmission value. The first of these three possibilities is serious, but the others are not, merely requiring a renormalization of the normal state transmission data.

How are the results affected by changes in the magnitude of ω_F ?

The principal object of these experiments has been a measurement of the frequency dependence of the fluctuations, to see if the description given by the time dependent Ginsburg-Landau equation is applicable. This equation is not on as good a footing as the rest of the Ginsburg-Landau theory. Most of the frequency dependence in the conductivities depends on ω_F, the relaxation rate in this equation.

$$\omega_F = \frac{16 k_B T}{\pi \hbar} \quad \frac{|T-T_c|}{T_c}$$

An attempt was made to fit the measured transmission data for Pb 3, above T_c, with ω_F replaced by 1.5 ω_F and by .6ω_F. In neither case did the resultant transmission curves agree with the data as well as those calculated using ω_F. The discrepancy was largest at the temperatures closest to T_c. For the larger value of ω_F the transmission curve was too steep and too small at low frequencies, and the frequency where it had its greatest curvature was at too high a frequency. The lower value produced deviations in the other direction. From these considerations ω_F must be within 20% of the nominal value.

What is the effect of σ_2 above T_c?

Schmidt does not calculate σ_2 for the case of $T>T_c$ and the data of Lehoczky and Briscoe do not require any such term. On the other hand the Kramers Kronig transforms do. The effect of including it in the calculation of the transmission ratios is to depress the curve somewhat at frequencies near the peak in σ_2, around ω_F, and at higher frequencies. This increases the curvature in the vicinity of ω_F and flattens the curves above it. In order to fit the far infrared measurements, σ_2 must be included in the transmission ratio calculation.

Is the term $\frac{k_B T}{\hbar\omega}\left(1-e^{-\frac{\hbar\omega}{k_B T}}\right)$ necessary?

This factor in the conductivities is a result of the time dependent perturbation theory used to calculate the conductivities. For $\hbar\omega >> kT$ it falls off as $1/\omega$. If $T = 6.5^{o}K$, the turnover frequency is 4.5 cm^{-1}. Measurements made below this frequency

would not show any need for this term. Above this frequency it is quite important. It forces the conductivities to zero faster than they would otherwise go. The transmission ratios then rise to one and flatten out faster than they otherwise would. This is required by the data.

What is the behavior in the critical region?

The critical region is defined as

$\Delta T = \tau_o R_N T_c$

In this temperature distance from the transition temperature at least half of the conductivity is due to fluctuations so that the volume of the fluctuations is large and they should be interacting with each other. The simple theory is expected to break down. However film Pb 3 has three of the spectra above T_c and two below in this critical region ($.1^o$ K wide). The calculations agree with the measurements as well within the critical region as without. The reason may well be that within the critical region ω_F is very small. ($\omega_F = .35\ cm^{-1}$ at the verge of it in the case of Pb 3). The measurements are all on the high frequency tails of the conductivities and these must be unaffected by interactions between the fluctuations. Further, the deviations in the dc resistance from the Aslamazov-Larkin result are often small.

Why is the difference between the experimental data and the theoretical curves larger below the transition?

Again in reference to Pb 3 (Figure 11), these differences seem to be due to the Mattis Bardeen conductivities rather than the fluctuation conductivities. The data taken closest to the transition ($T-T_c = -.007$) where the fluctuations are the largest

and the contribution from the quasi-particles the smallest give the best agreement between experiment and theory. The situation deteriorates as the temperature is reduced away from T_c. To fit the data, the energy gap needs to increase faster than the BCS expression

$$\Delta(T) = 1.67\Delta(0)\ \left(\frac{T_c - T}{T_c}\right)^{\frac{1}{2}}$$

as the temperature is decreased.

In any event, the fluctuation conductivities are required to fit the data. Figure 16 shows plotted the data and the calculated transmission ratios using the Mattis-Bardeen conductivities alone (dashed line) and the fluctuation conductivities plus the Mattis-Bardeen conductivities (solid line). Two of the spectra for Pb 3 are used. In this figure there has been no fitting of data in any way; the points and theoretical curves are all numerically equal to the values on the figure. At low frequency the fluctuations give good agreement; at high frequencies neither do well. If it is allowed to shift the points up and down, they can be made to fit fairly well with the fluctuations, but never with Mattis-Bardeen alone.

What is the magnitude of the fluctuation effects compared to the transmission ratio of the superconducting state (at 4.2^{o} K) to the normal state?

The fluctuation effects are quite small. For instance, in the case of Pb 6 the maximum distance the transmission ratio in the fluctuation temperature range above T_c ever gets from one is .96, a 4% variation. The transmission ratio for superconducting normal

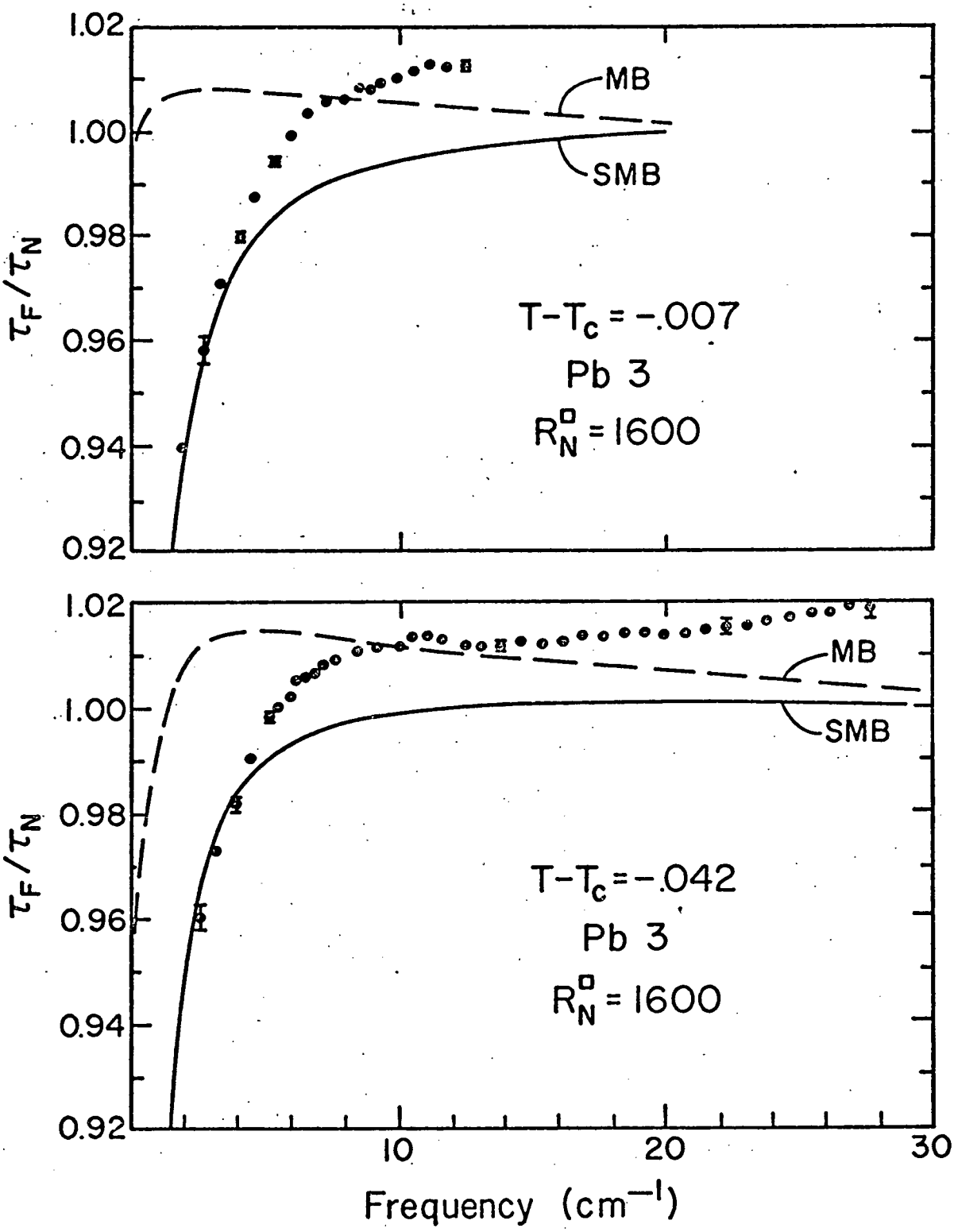

Fig. 16. Transmission ratio versus frequency for two temperatures below T_c for Pb 3. The solid line is from the fluctuation conductivities plus the Mattis Bardeen conductivities (SMB); the dashed line the MB conductivities alone.

$(4.2^{o}/9^{o})$ of this same film is .75 at 2 cm^{-1}. It rises to 1.27 at 22 cm^{-1} (the energy gap) and then falls off towards one. It varies 25% on either side of one. On this scale the transmission ratios near T_c would appear virtually flat.

12. Summary and Conclusions.

In this chapter I have presented calculations and measurements of the frequency dependence of the fluctuation induced conductivity of thin lead films in the vicinity of the superconducting transition temperature. The real and imaginary parts of the conductivities were calculated in the time dependent Ginsburg-Landau theory both above and below the transition temperature.

Measurements of the transmission of far infrared radiation through four thin lead films, as a function of temperature were made. The dc resistance of the films was also measured. Both types of measurements showed an increase in the conductivity near T_c.

The experimental data is well described by the conductivities calculated from the Ginsburg-Landau thoery. The relaxation rate in the time dependent equation

$$\omega_F = \frac{16k_BT}{\pi\hbar}\left(\frac{T-T_c}{T_c}\right)$$

is that which best fits the results of the measurements.

CHAPTER IV

SMALL PARTICLES

1. General.

This chapter describes experiments on the far infrared transmission of arrays of small metallic particles. The particles are on the order of 100 Å in diameter and their infrared response is drastically affected by the size limitation of the electron energies. The mean energy level spacing at the Fermi surface is, for non-degenerate levels, just the inverse of the density of states of the free electron gas for one spin direction[53]

$$\Delta = \frac{12\pi\hbar^2}{D^3 m^* k_F} = \frac{4}{3}\,\frac{\varepsilon_F}{N}$$

where D is the diameter of the particle, k_F and ε_F the Fermi momentum and energy, and N the number of electrons.

Kubo[53] was the first to point out that the energy level spacing changes the macroscopic behavior of the particles; he calculated the specific heat and the magnetic susceptibility of the particles. Further calculations were reported by Gor'kov and Éliashberg[54] and by Denton et al.[55] Measurements of the spin lattice relaxation time and of the static magnetic susceptibility have been carried out by Kobayashi et al[56] and by Buhrman.[58] The situation with respect to these static properties is somewhat fluid at present.

The main theoretical difficulty in the problem comes in

deciding what kind of ensemble average to use in calculating the partition function. It is necessary to put into the calculation a probability function; the probability that, given a level at energy ϵ, there is another level δ away. The simplest form would have an exponential form:

$\frac{1}{\delta} e^{-\frac{\delta}{\Delta}}$. The problem of averaging over ensembles of randomly separated energy levels has been extensively studied for the case of level statistics in large nucleii. Dyson[59] discussed it for various symmetries; he found three distinct ensembles. Gor'kov and Éliashberg[54] applied these to the case of small metallic particles to calculate, among other things, the electromagnetic response. The applicability of the ensembles depends on the strength of the spin orbit coupling. In the case of "small" spin orbit coupling the orthogonal ensemble applies, for "large" spin orbit coupling the symplectic ensemble is used, and for a large magnetic field and "large" spin orbit coupling the unitary ensemble is used. The exact meaning of the terms "large" and "small" is not completely clear. When the spin orbit coupling is "large" there are big interactions among the levels; they are expected to repell each other and fall into a more uniform arrangement; in this case a more periodic behavior is expected than in the orthogonal ensemble.

2. Electromagnetic Response.

The result of the calculation by Gor'kov and Éliashberg is that the dielectric polarizability is (for small electric fields and the diameter, D, less than the bulk mean free path)

$$\chi_e = \frac{16}{5}\frac{e^2D^2}{\Delta} + \frac{139}{900\pi}\frac{e^2D^3}{hV_F}A(\omega)$$

where the first term is the static polarizability, and is frequency independent. V_F is the Fermi-velocity. The function $A(\omega)$ is determined by the ensemble average used.

For light metals ("small" spin orbit coupling) the orthogonal ensemble applies. Expressed in terms of the integral sin (Si(χ)) and cosine (Ci(χ))

$$\Delta(\omega) = 2 - \frac{\Delta}{\pi\hbar\omega}\sin\frac{2\pi\hbar\omega}{\Delta} - \frac{2\Delta}{\pi\hbar\omega}\mathrm{Ci}\left(\frac{\pi\hbar\omega}{\Delta}\right)\left(\sin\frac{\pi\hbar\omega}{\Delta} - \frac{\pi\hbar\omega}{\Delta}\cos\frac{\pi\hbar\omega}{\Delta}\right)$$

$$+i\left(\frac{2\pi\hbar\omega}{\Delta}\frac{\Delta}{\pi\hbar\omega} + \frac{\Delta}{\pi\hbar\omega}\cos\frac{2\pi\hbar\omega}{\Delta} - \frac{\Delta}{\pi\hbar\omega}\mathrm{Si}\left(\frac{\pi\hbar\omega}{\Delta}\right)\left(\sin\frac{\pi\hbar\omega}{\Delta} - \frac{\pi\hbar\omega}{\Delta}\cos\frac{\pi\hbar\omega}{\Delta}\right)\right)$$

The limiting forms of this are; for low frequencies $\hbar\omega << \Delta$

$$A(\omega) = \frac{2\pi^2}{3}\frac{\hbar^2\omega^2}{\Delta^2}\left(2 - \ell n\,\frac{\pi\gamma\hbar\omega}{\Delta}\right) + \frac{i\pi^3}{3}\frac{\hbar^2\omega^2}{\Delta^2}\ ;\ \gamma = 1.781\cdots$$

and for high frequecies $\hbar\omega >> \Delta$

$$A(\omega) = 2 - 2\left(\frac{\Delta}{\pi\hbar\omega}\right) - 2\left(\frac{\Delta}{\pi\hbar\omega}\right)^3\sin\frac{2\pi\hbar\omega}{\Delta} + i\left(\frac{2\pi\hbar\omega}{\Delta} - \frac{2\Delta}{\pi\hbar\omega} + \left(\frac{\Delta}{\pi\hbar\omega}\right)^3 x\right.$$

$$\left. x\left(3 + \cos\frac{2\pi\hbar\omega}{\Delta}\right)\right)$$

For heavy metals ("large" spin orbit coupling) the symplectic ensemble is used.

$$A(\omega) = 2 - \frac{\Delta}{2\pi\hbar\omega}\sin\frac{2\pi\hbar\omega}{\Delta} - \frac{\pi\hbar\omega}{\Delta}\left(\frac{\pi}{2} + \mathrm{Si}\left(\frac{\pi\hbar\omega}{\Delta}\right)\right)\left(\cos\frac{\pi\hbar\omega}{\Delta} + \frac{\pi\hbar\omega}{\Delta}\sin\frac{\pi\hbar\omega}{\Delta}\right)$$

$$+i\left\{\frac{\pi\hbar\omega}{\Delta} - \frac{\Delta}{\pi\hbar\omega}\sin^2\frac{\pi\hbar\omega}{\Delta} + \frac{\pi\hbar\omega}{\Delta}\left(\frac{\pi}{2} + \mathrm{Si}\left(\frac{\pi\hbar\omega}{\Delta}\right)\right)\left(\frac{\pi\hbar\omega}{\Delta}\cos\frac{\pi\hbar\omega}{\Delta} - \sin\frac{\pi\hbar\omega}{\Delta}\right)\right\}$$

The limiting forms of this are, $\hbar\omega << \Delta$

$$A(\omega) = \frac{2}{9}\left(\frac{\pi\hbar\omega}{\Delta}\right) + \frac{i}{45}\left(\frac{\pi\hbar\omega}{\Delta}\right)^5$$

and $\hbar\omega >> \Delta$,

$$A(\omega) = 2 - \frac{\pi}{2}, \sin\frac{\pi\hbar\omega}{\Delta} + i\left(\frac{\pi\hbar\omega}{\Delta} + \frac{\pi}{2}\cos\frac{\pi\hbar\omega}{\Delta}\right)$$

In the case of the symplectic ensemble there are large periodic variations in the polarizability with frequency while the orthogonal ensemble yields a smooth function.

The dielectric constant is

$$\varepsilon = \varepsilon_1 + i\varepsilon_2 = 1 + 4\pi\frac{N}{V}\chi e$$

where N/V is the number of particles/unit volume and the absorption coefficient can be calculated from

$$\alpha = \frac{2\omega}{c}\left(\frac{\varepsilon_1}{2}\sqrt{1+\varepsilon_2{}^2/\varepsilon_1{}^2} - \frac{\varepsilon_1}{2}\right)^{\frac{1}{2}}$$

In the case that $\varepsilon_2 << \varepsilon_1$ then $\varepsilon_1 \simeq 1$ since $\mathrm{Im}\chi_e \simeq \mathrm{Re}\chi e$

$$\alpha = \frac{\omega\varepsilon_2}{c}$$

$$= \frac{139}{225}\frac{N}{V}\frac{\omega e^2 D^3}{\hbar c V_F}\,\mathrm{Im}\,A(\omega)$$

This should be compared with the result for classical absorption by small particles (Mie theory)[60] as discussed in Appendix 2.

$$\alpha = \frac{2\pi^2}{3}\frac{N}{V}\frac{\omega^2\sigma_1 D^3}{c}\left(\frac{9}{16\pi^2\sigma_1{}^2} + \frac{D^2}{4Dc^2}\right)$$

Figure 17 shows the dielectric constant as a function of frequency calculated in this theory for the orthagonal and symplectic ensembles. These curves are calculated for a diameter of 100 $\mathring{A}$, a filling factor for the particles, f,

$$f = \frac{N}{V} \frac{\pi D^3}{6}$$

of .03, and a Fermi velocity of 1.5×10^8 cm/sec. The mean energy level spacing using these numbers is

$$\Delta = 10.8 \text{ cm}^{-1} = 1.35 \text{ meV} = 15.6^{\circ} \text{ K}$$

and $N/V = 5.7 \times 10^{16}$ particles/cm^3. Notice that since $N/V \sim 1/D^3$ and the frequency dependent part of the polarizability, $\chi_e \sim D^3$ these dielectric constants as a function of the ratio ω/Δ are independent of frequency. To find the value of the dielectric constant for a different particle size, merely multiply the frequency axis by $\frac{10.7 \text{cm}^{-1}}{\Delta(D)}$ to get the appropriate frequency scale for the other size.

In Figure 17 the orthogonal ensemble is shown as a solid line and the symplectic ensemble as a dashed line. The real parts of the dielectric constant, ε_1, are not very interesting having a value of 1.13 at high frequencies, and falling to 1 at zero frequency. The orthogonal case is smooth between while the symplectic one oscillates a small amount. The imaginary parts rise with increasing frequency, becoming quite large at high frequencies, with medium size oscillations in the orthogonal ensemble and rather large ones in the symplectic case. The

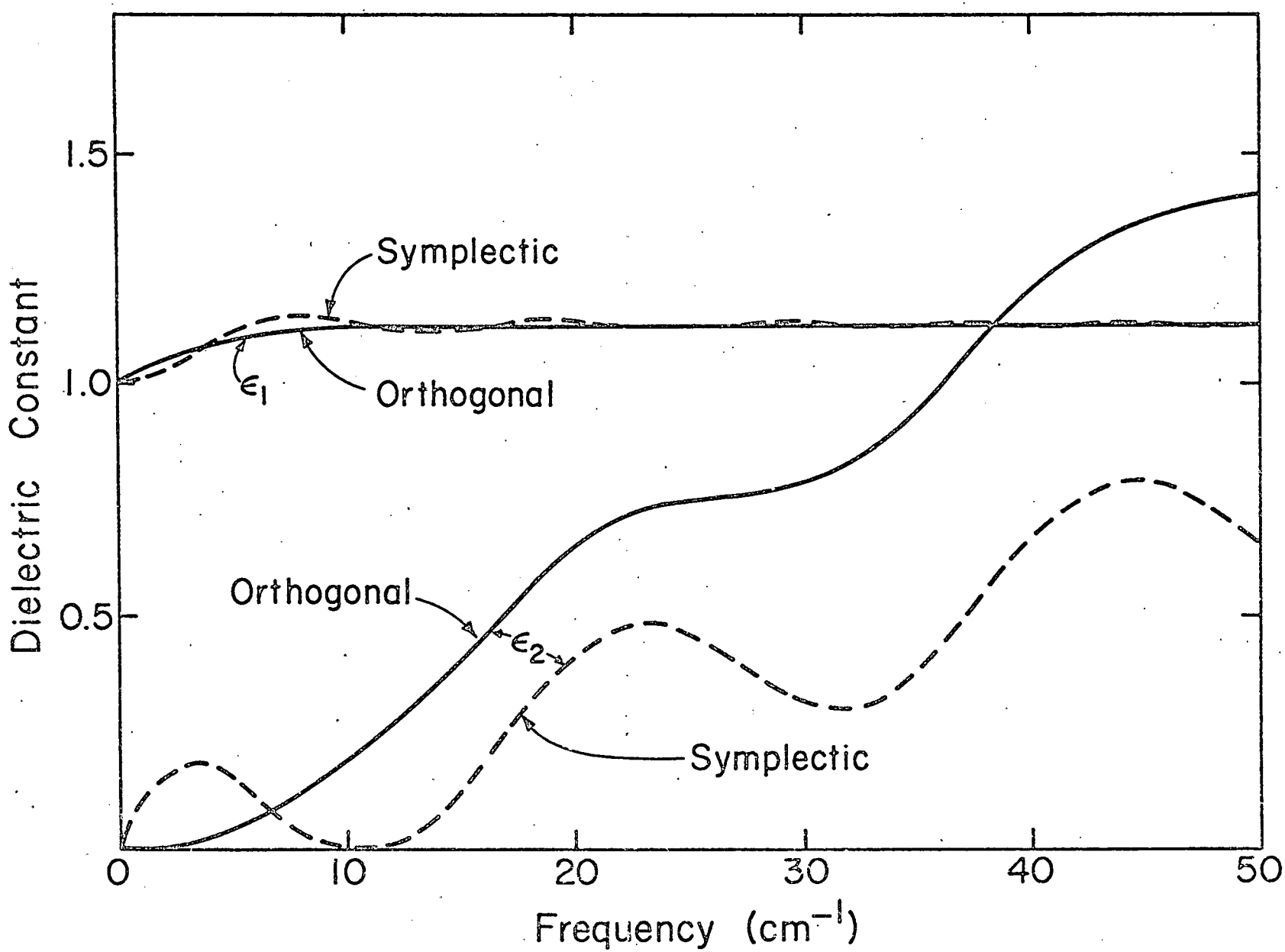

Fig. 17. Real (ε_1) and imaginary (ε_2) parts of the dielectric constant of small particles in the Gor'kov-Éliashberg model.

magnitude of the imaginary part of the dielectric constant in the case of the orthogonal ensemble is about twice that of the symplectic ensemble.

Figures 18 shows the absorption coefficients, α, versus frequency for both cases (solid line for the orthogonal ensemble and dashed for the symplectic one). These absorption coefficients are calculated for two different diameters, 100 $\mathring{A}$ and 200 $\mathring{A}$. The curves are similar in shape for the two sizes; the frequency scales are just different. The orthogonal ensemble shows smaller wiggles than the symplectic and is twice as large. If the wiggles are smoothed out, the high frequency absorption coefficient is linear in frequency and extrapolates to zero at $\omega = \Delta$. In the cases when this theory applies, this gives a way to measure the mean energy level spacing in the small particles. A log-log plot of the absorption coefficients shows that the low frequency tail in the absorption coefficient goes to zero as $\omega^{3.7}$ in the orthagonal case and something like ω^{10} in the symplectic case, although the little bump in the latter case makes determination of this a bit difficult.

Figure 19 is a plot of the absorption coefficient of particles which obey the Mie theory (see Appendix B). Here the absorption coefficient, which increases as ω^2, is three orders of magnitude below that in the Gor'kov-Eliashberg case. This was calculated for D = 100 $\mathring{A}$, $\sigma_1 = 5\times10^{16}$ and $N/V = 5.7\times10^{16}/cm^3$.

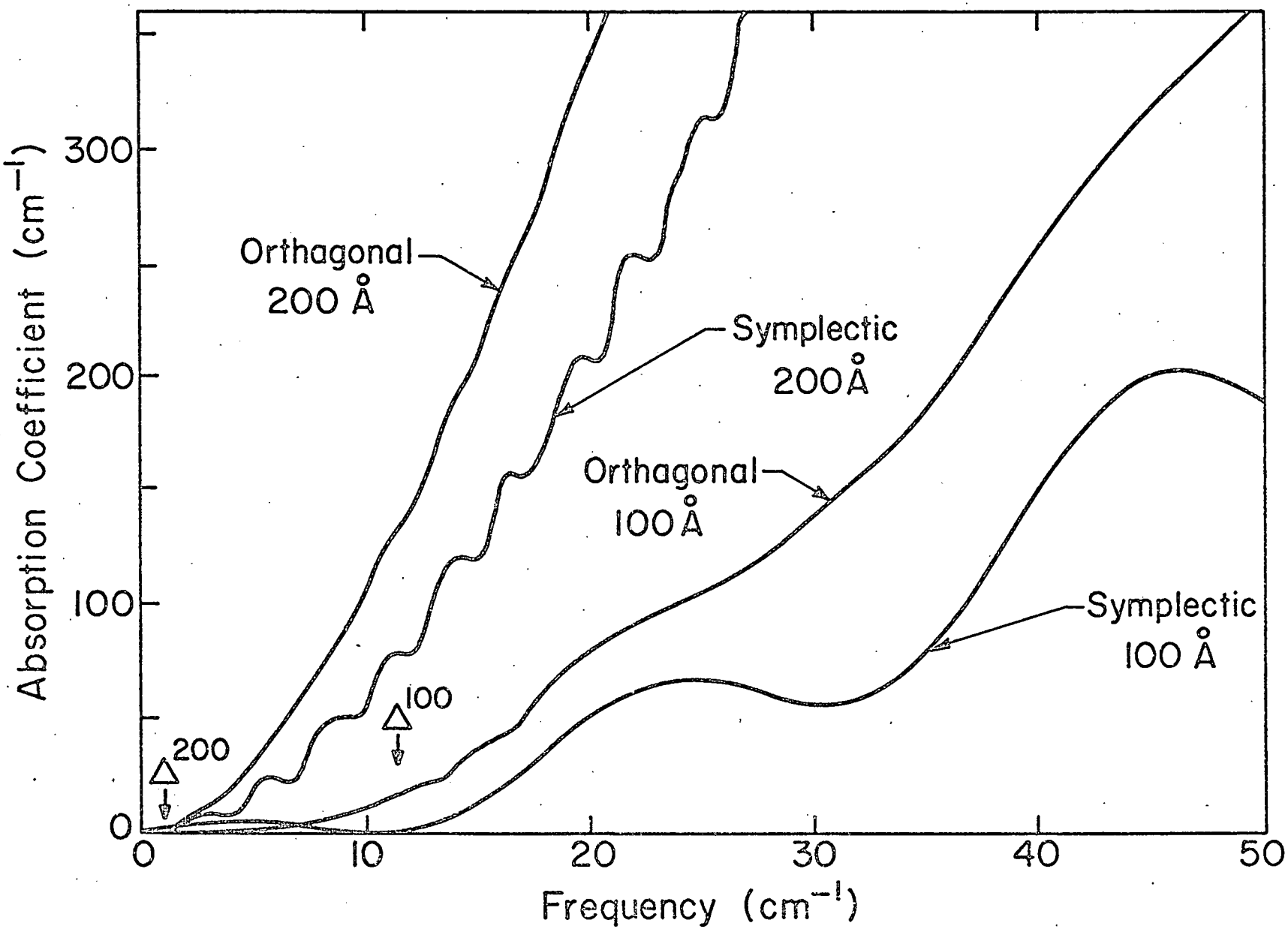

Fig. 18. Absorption coefficient versus frequency for small particles in the Gor'kov-Eliashberg model.

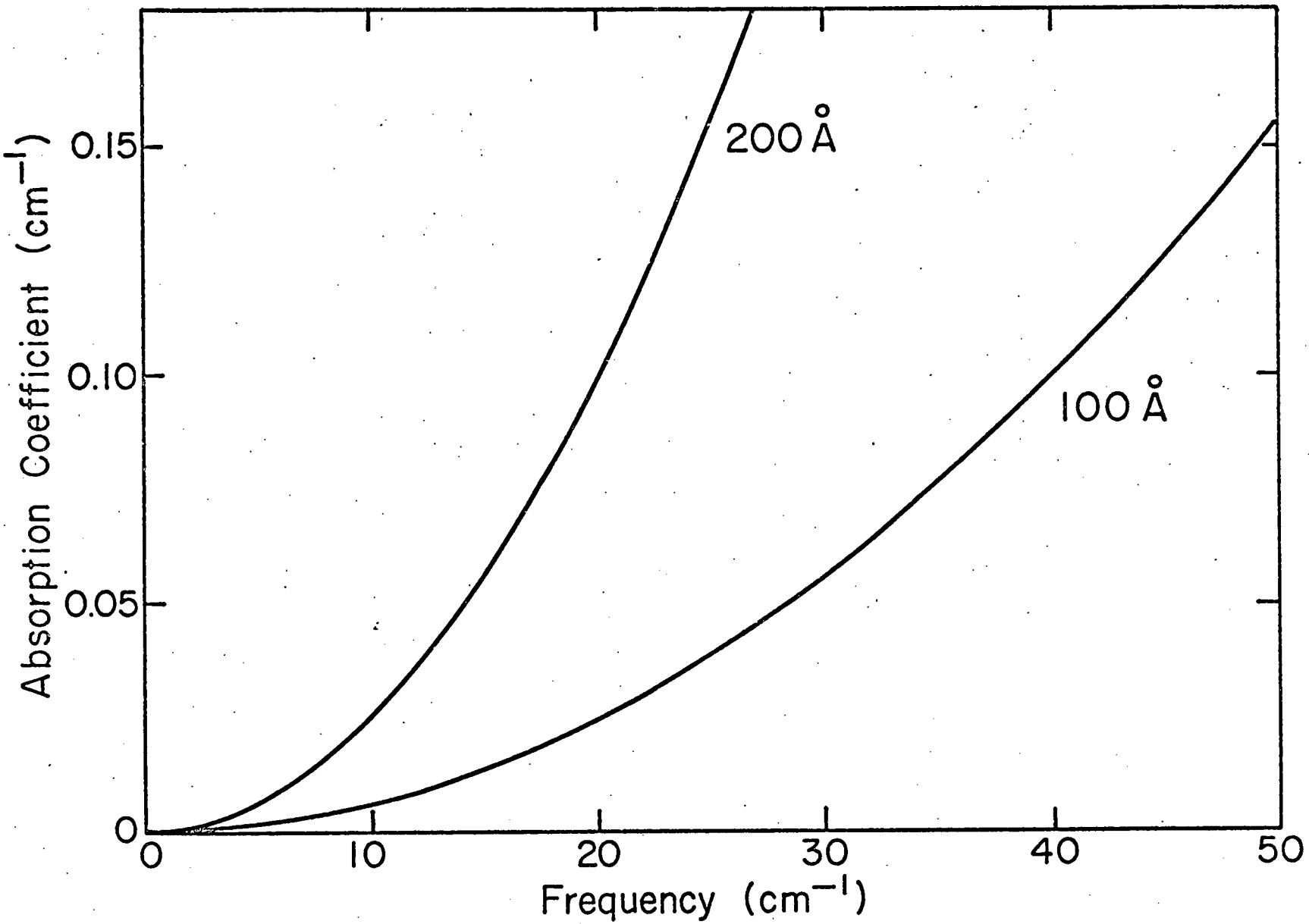

Fig. 19. Absorption coefficient versus frequency for small particles in the Mie-Debye theory.

3. Superconductivity.

The size of the small particles might be expected to affect superconducting behavior for two reasons. If the diameter is on the order of 100 Å then the mean energy level spacing is on the order of kT_c. Further, if the diameter of the particle is less than the coherence length of the electrons, the conditions for long range order do not exist. Anderson[61] and Strongin et al[62] have considered this and have concluded that if $\Delta > 2\ kT_c$, there is no superconductivity. (The effective transition temperature of the particles is zero). The particles exhibit the bulk transition temperature when $\Delta = kT_c$.

Schmid[63] has discussed the existance or lack thereof of the energy gap in a superconductor without long range order. His conclusion is that there is no energy gap; the density of electron states at T = 0 rises linearly from zero at zero frequency to a peak near the BCS energy gap after which it falls off to the normal state value. This discussion ignores any influence of finite energy level spacing (compared to the BCS gap).

Hurault[64] et al considered the effect of fluctuations above the transition temperature on small particles. A simple calculation from Schmidt's[66] theory (see Chapter III) yields only small fluctuation conductivities above the transition temperature. Hurault et al included other diagrams than the Aslamazov-Larkin one in their calculations and found an extra conductivity proportional to $1/\ln(T/T_c)$. They have left out any effects of size quantization; this limits consideration of their calculations to particles of above 1000 Å diameter.

Buhrman[58] has observed both fluctuations above T_c and superconducting behavior below T_c in the dc magnitization of the very small particles upon which these far infrared experiments were performed. The magnitude of these contributions to the susceptibility is quite small compared to the susceptability of bulk superconductors. One might expect it to be reduced by the ratio of the volume of the particle to the "volume" of a Cooper pair, e.g. by D^3/ξ_o^3 or 10^{-4}. Other superconducting effects would be reduced by the same amount. The point is that the surface acts as a very strong pair breaker; an electron must be scattered when it strikes the surface of an isolated particle.

The appearance of an energy gap in an array of small particles would change the transmission of radiation with frequencies near the gap in similar fashion to a thin film. Relative to the transmission in the normal state, there would be a peak in the transmission at the gap frequency and a decrease below it.

4. Noninfrared Properties of the Samples.

During the course of these experiments far infrared measurements were made on samples of carbon, copper, aluminum, tin, and lead. Table II collects pertinant data on these samples. The carbon was commercial lampblack, obtained from the Carbolac Corp.[66] All of the numbered metallic samples were made by the smoke method; the other two were sludge. The sample designation is in the first column of the table. In the second is the helium gas pressure, in Torr, that was in the bell jar during the smoke evaporation. In all of the smoke except Cu 1 oxygen was bled into the bell jar during the evaporation. To make Al 3 the helium was replaced by argon.

TABLE II

PROPERTIES OF SMALL PARTICLES

Sample	He Press. p Torr	Diam. D A	Var. D A	Energy Level Spacing cm^{-1}	Energy Level Spacing meV	Filling Factor f	Number Density 10^{17} cm^3
C	--	90		--		.043	1.1
Cu 1	5	65	15	39 21-86	4.9 2.6-11	.025	5.2
Cu 2	.5	70	10	31 21-50	3.9 2.6-6.2	.028	4.2
Cu 3	2.5	270	30	.55 .40-.97	.068 .049-.121	.027	.055
Cu sludge	--	100	30	11 5-30	1.3 .6-4	.12	36
Al 1	.5	150	12	4.2 3.3-5.3	.51 .41-.66	.04	.38
Al 2	.5	400	40	.22 .16-.30	.027 .020-.037	.04	.023
Al 3	2 (Ar)	375	25	.27 .22-.32	.033 .027-.041	.04	.022
Sn 1	1	140	15	8.9 6.5-12	1.1 .81-1.5	.018	.25
Sn 2	5	150	25	7.2 4.5-12	.90 .56-1.5	.018	.34
Pb sludge	--	100?	30?	15 7-40	1.8 .8-5	.12	36

The diameter is that determined by electron microscopy of the samples. For each smoke evaporation there were two electron microscope grids in the bell jar. These were examined by Buhrman[58] under appropriate magnification and pictures were taken. From these the diameter and its variation could be found. The variation in size given in the table is a plus or minus amount on the diameter which contains about 75% of the particles. The electron microscope slide for the copper sludge was prepared by placing a drop of the colloid on the grid and letting it dry. There were no pictures taken of the lead; its size is estimated from experience[58] to be about that of the copper.

The next two columns give the energy level spacing in cm^{-1} and meV. The upper number is that calculated from the average size; the lower two come from adding and then subtracting the variation from this size. The last two columns in the table show the packing density or filling factor of the particles, and the number per unit volume. These are calculated from

$$f = \frac{W}{\rho V}$$

$$\frac{N}{V} = \frac{6f}{\pi D^3}$$

where ρ is the density of the bulk metal, W the weight of the sample, V its volume and D the diameter of the particles.

There is one other important sample property that is not included in the table because it is the same in all samples. This is the electrical resistance of the samples which is in all cases greater than 100 Meg Ω at 300° K. This is the limit of the

of the measuring apparatus and corresponds to a resistivity in the powder of $10^6 \Omega$cm. Our samples are well isolated and should be distinguished from those called granular films where there is considerable tunneling between individual particles yielding resistivities on the order of 10^{-3} to $10^{-4} \Omega$cm. This is an important distinction; particles which are closely connected by tunneling will show quite different superconducting properties as the Cooper pairs can easily pass from particle to particle. Size quantization will be affected also.

The typical weight of the samples was .01 to .03 grams, this was spread over an area of 1.5 cm^2 so that the samples were .1 to .2 cm thick. Perhaps the most surprising result of these experiments is that metals of this thickness show large infrared transmissions.

5. Far Infrared Results.

The absorption coefficient, α, in the far infrared is shown in the next several figures for some of the samples. It is defined as

$$\alpha = -\frac{1}{\ell} \ln \frac{I}{I_o}$$

where I is the intensity transmitted through the sample, I_o is the incident intensity, measured by replacing the sample with an empty sample holder, and ℓ is the length of the sample. For small particles ℓ is defined as

$$\ell = \frac{W}{\rho f A}$$

where W is the weight of the sample, A its cross sectional area, ρ is the density of the bulk metal, and f is the filling factor of the powder.

The plots are of α in cm^{-1} versus frequency in cm^{-1} along the bottom and GHz along the top. There has been one readjustment to the data. This arises because the particles are such strong absorbers at high frequencies that replacing the particles with a blank hole causes the detector sensitivity to decrease slightly. The signal is lower than it should be and the result is that the particles appear to be more transparent than they really are or could possibly be. The absorption coefficients before adjusting are negative. Either the above explanation is correct, in which case the addition of a constant value to the data is justified, or the particles emit radiation at low frequencies. The readjustment typically comes to 20% of the value of the absorbtion coefficient at 50 cm^{-1}.

Figure 20 shows the results for carbon particles, 90 $\mathring{A}$ in diameter. This is intended to show the behavior of non-metallic particles. It shows a smooth almost linear increase ($\sim\omega^{3/2}$) in absorption coefficient with frequency indicating nearly a constant non-zero value for the imaginary part of the dielectric constant. Since the carbon was handled in the same fashion as the metallic particles any effects from adsorbed gasses on the surfaces should show up here; if there are any they add no structure to the dielectric constant. The data were taken at 2^{o} K, but there is no difference between this and 1.2^{o} K and 4.2^{o} K.

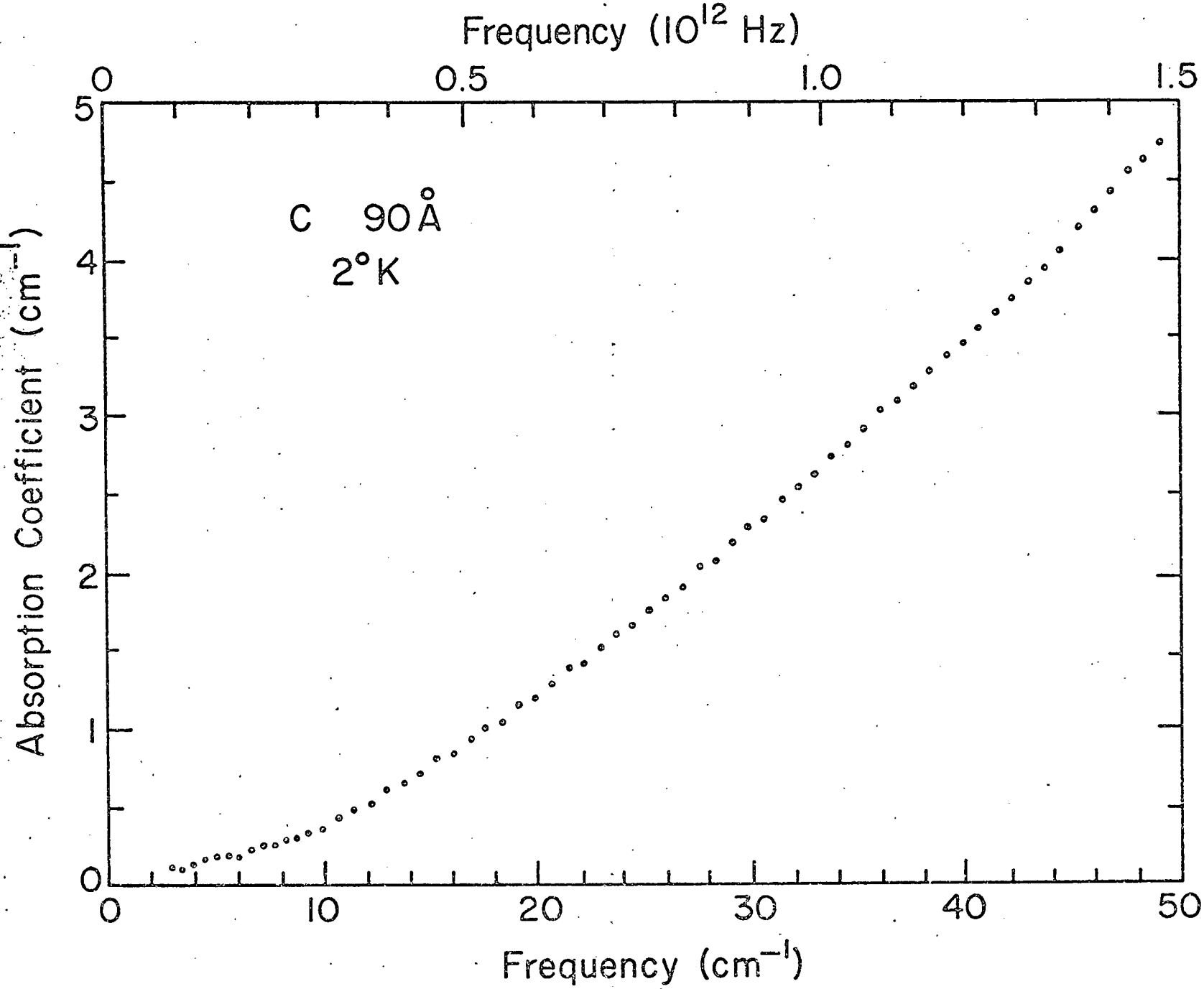

Fig. 20. Absorption coefficient versus frequency for C small particles.

Figure 21 gives the absorption coefficient for 65 Å copper smoke, Cu 1, at 4.2° K. This sample shows a high absorption coefficient (higher than any other smoke sample). It shows more structure than the carbon, looking quite like the absorption coefficient of the orthagonal ensemble but with a lower value by a factor of two. The nearly linear section has a slight wiggle and extrapolates to zero at 6.0 ±.5 cm^{-1}.

The absorption coefficients at 4.2°K of both Cu 2 and Cu 3 are shown in Figure 22. Cu 2 has an average diameter of 70 Å and Cu 3 of 270 Å. The absorption coefficients are much lower in these than in Cu 1. Cu 2 has a horizontal (zero) value at low frequencies and then rises nearly linearly at high frequencies. The bend is not as sharp as in Cu 1. The linear section extrapolates to zero at 19 ± 1 cm^{-1}. Cu 3 is already rising linearly at the lowest frequencies. This section extrapolates to zero near zero frequency. There is a big bend at 30 to 35 cm^{-1} and then it goes off linearly but more steeply than before. As expected the larger particles absorb more at a given frequency than the smaller ones but the difference is only a factor of two instead of the factor of four to eight expected.

Figure 23 gives the absorption coefficient at 4.2° K of the 100 Å copper made by the sludge method. This has a large absorption coefficient (due in part to the denser array this manufacturing method yields) which is linear at high frequencies and has the leveling off at low frequencies. The high frequency data extrapolates to zero at 11 + 1 cm^{-1}.

In Figure 24 is shown the data for 150 Å aluminum, Al 1, at

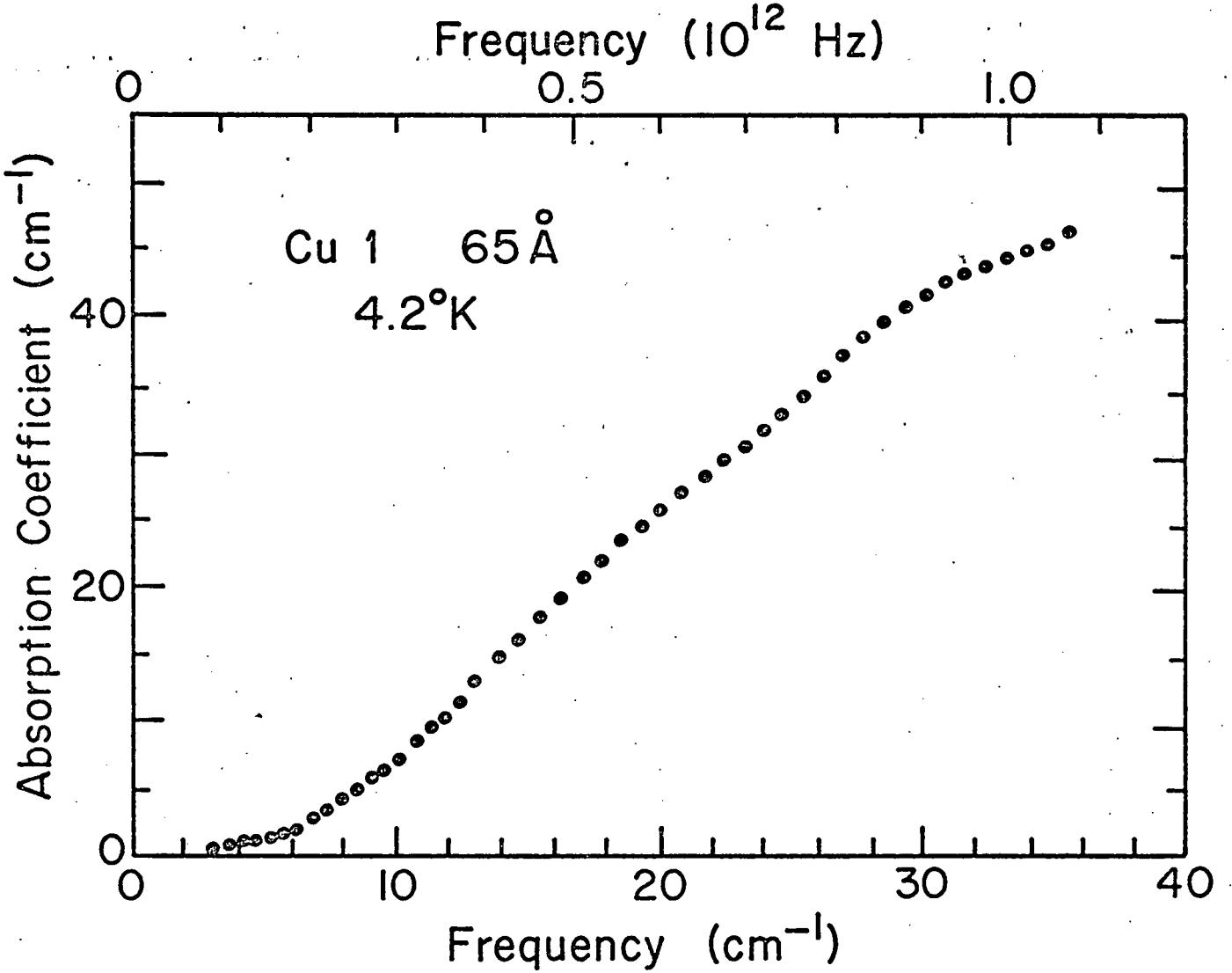

Fig.21. Absorption coefficient versus frequency for Cu 1.

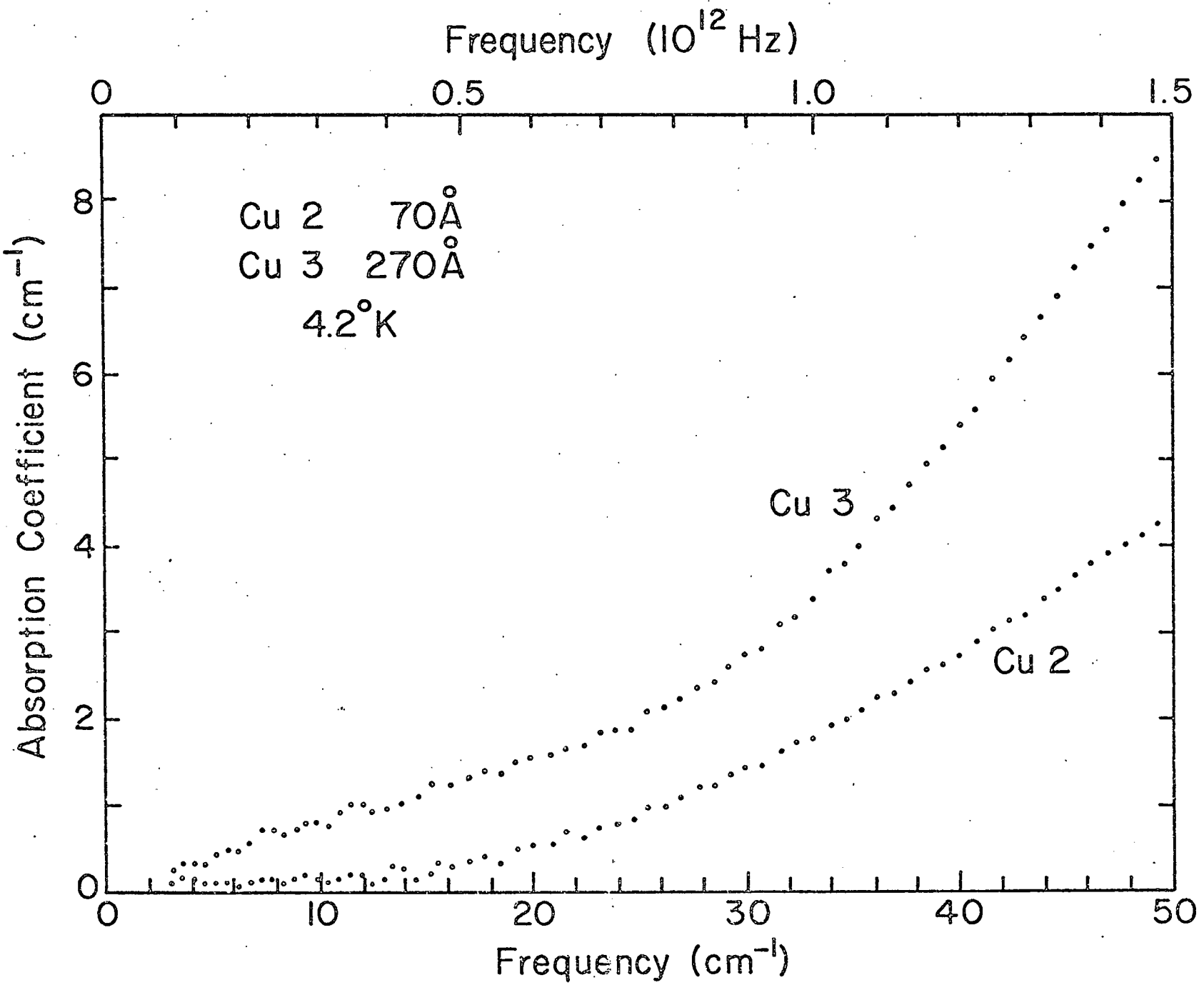

Fig. 22. Absorption coefficient versus frequency for Cu2 and Cu3.

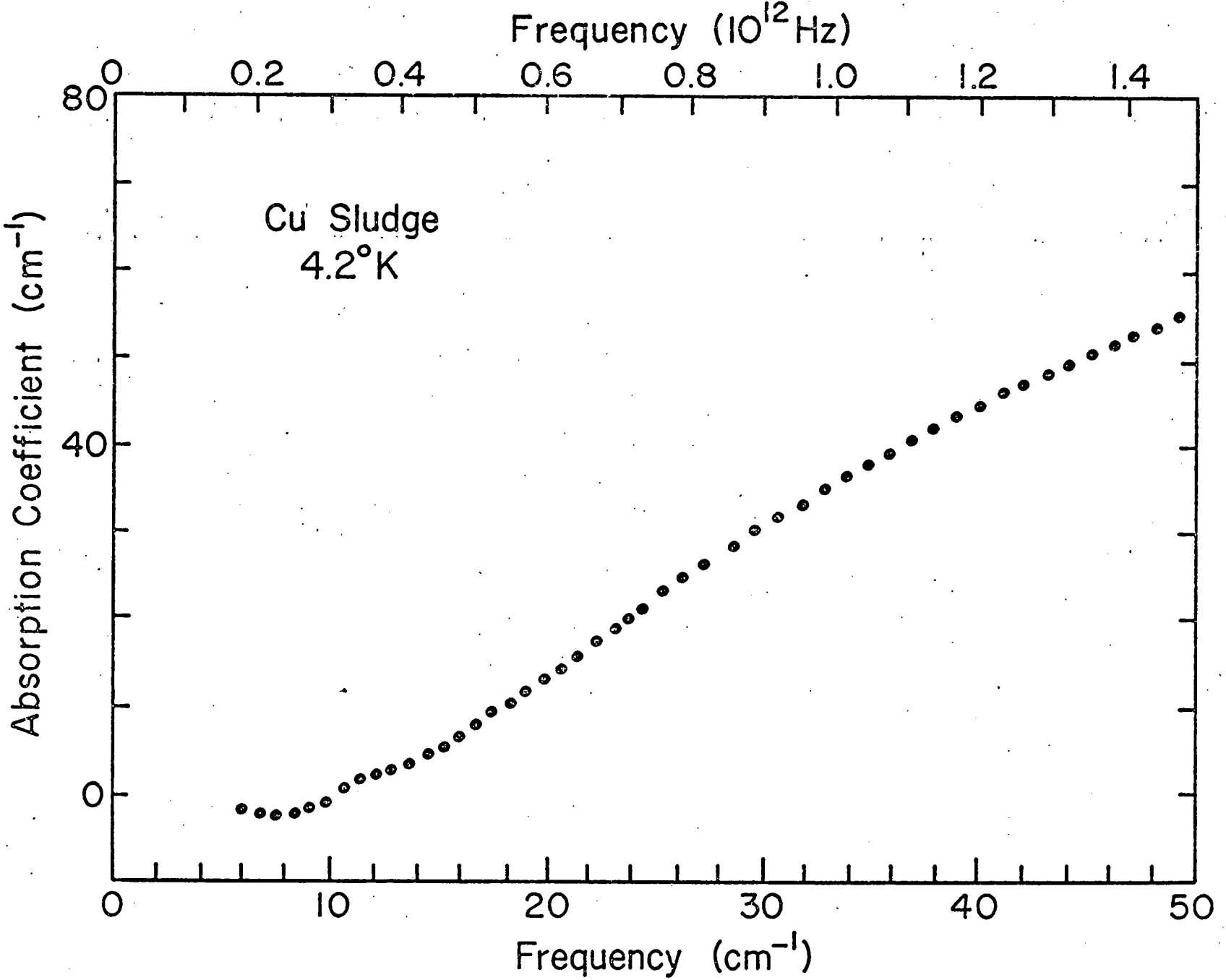

Fig. 23. Absorption coefficient versus frequency for Cu sludge.

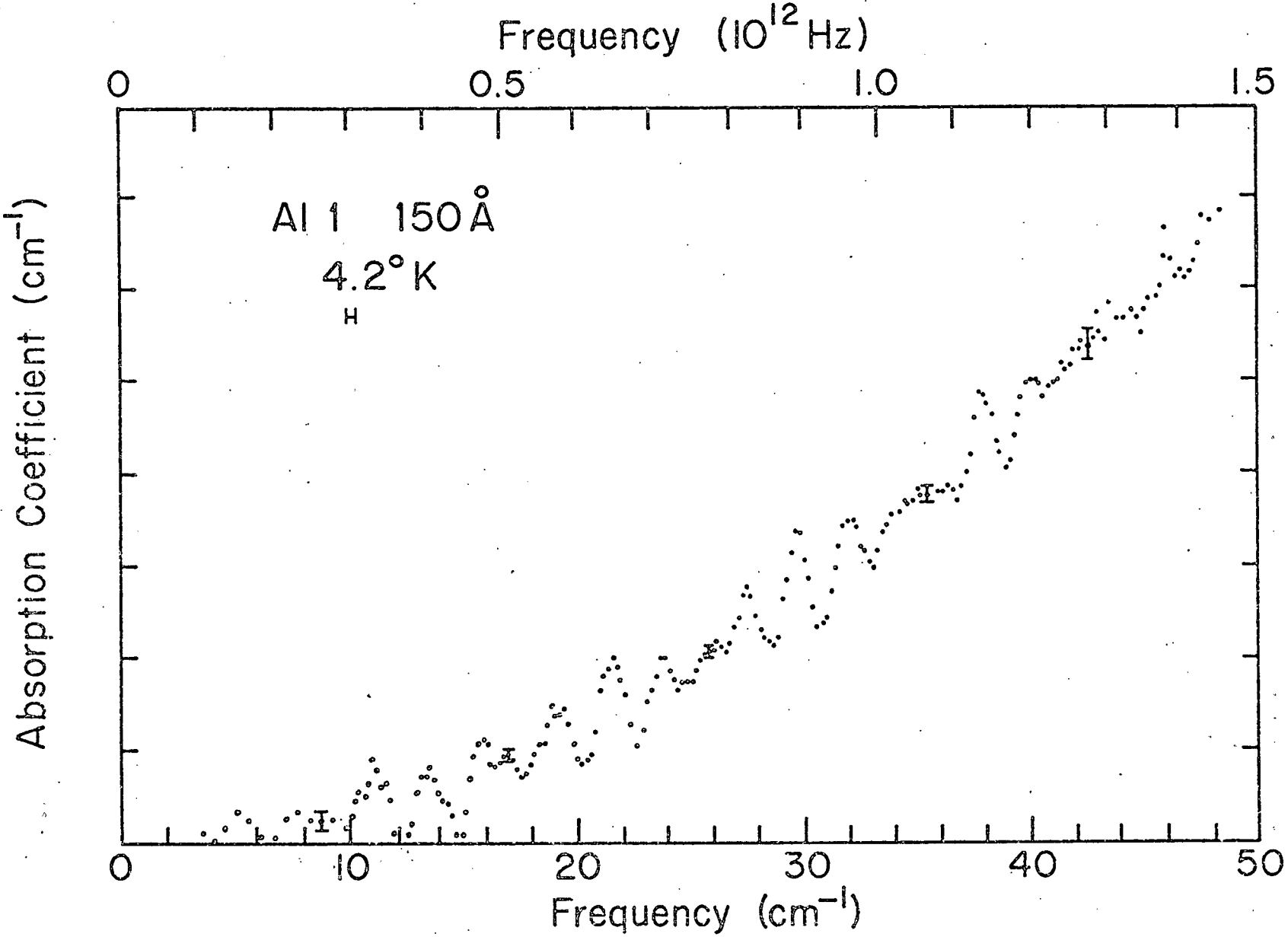

Fig. 24. Absorption coefficient versus frequency for Al 1. The resulution is higher than in the other figures.

4.2^{o} K. This is a high resolution run ($r = .4\ cm^{-1}$) and there is a large amount of structure. This consists of short straight sections separating three cycles of large oscillations. The oscillations are at 2.3 $\pm .1\ cm^{-1}$ intervals. The pattern repeats at 8.1 $\pm .2\ cm^{-1}$ intervals. There are error bars in a few places showing the noise on the data, which is much smaller than the oscillations are. If the upper section is extrapolated to zero, ignoring the oscillations, it intersects at 13 $\pm 1\ cm^{-1}$. The spectrum shown was taken at 4.2^{o} K but there is no noticible difference between this and one at 2^{o}K.

Figure 25 displays the results for the other two aluminum samples, Al 2 (400 Å) and Al 3 (370 Å), at 2^{o} this time. Both have absorption coefficients considerabley larger than Al 1. Neither absorption coefficient levels out at low frequencies. Both extrapolate to zero below the lowest frequency measured.

Figure 26 gives the results for 140 Å tin particles, Sn 1, at two temperatures, 4.2^{o} K and 1.2^{o} K. It shows the usual behavior, with the straight upper section extrapolating to zero at 13 $\pm 1\ cm^{-1}$. There are some very small oscillations here, with period 8 to 9 cm^{-1}. The low frequency end is almost flat. The inset at the upper left shows the absorption in the same region at 1.2^{o} K. The superconducting transition temperature of tin is 3.4^{o} K and the energy gap is at 9.2 cm^{-1} in bulk or thin film tin samples. Any effect of the superconductivity should show up here. The two curves at the two temperatures are almost identical point by point; no effect due to the superconductivity can be seen. The data for Sn 2 was pretty much the same.

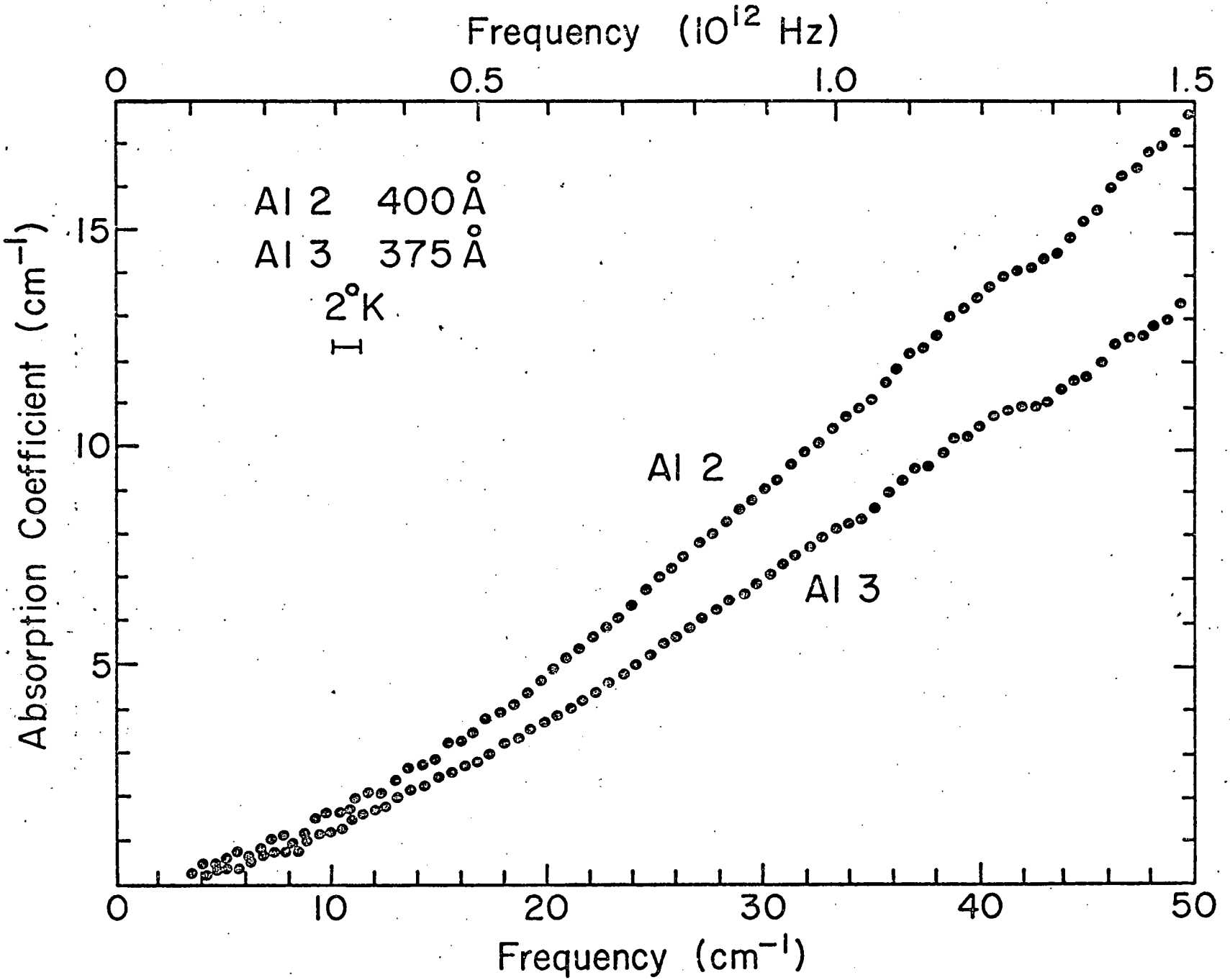

Figure 25. Absorption coefficient versus frequency for Al 2 and Al 3.

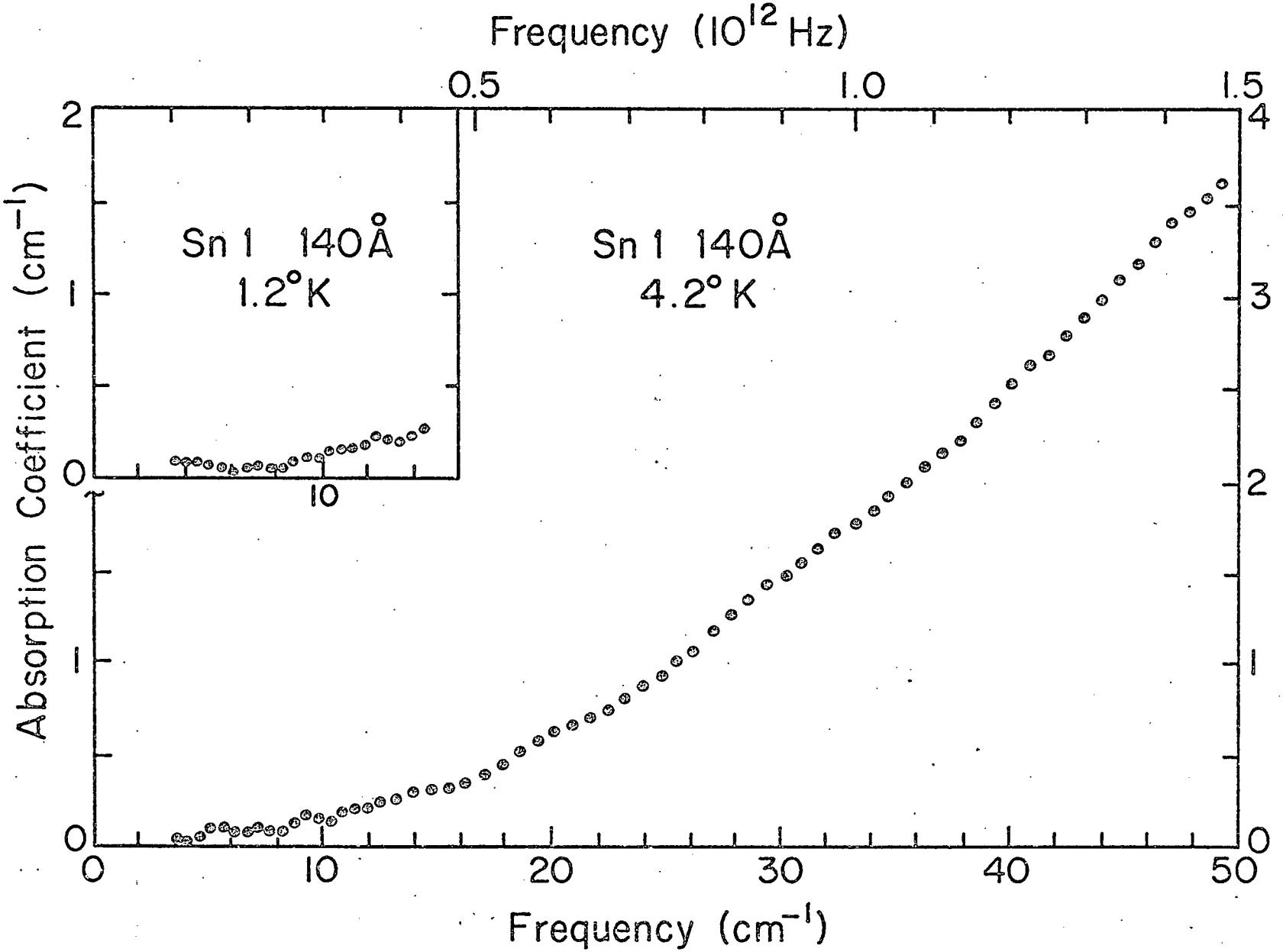

Fig. 26. Absorption coefficient versus frequency for Sn 1 at two temperatures.

In Figure 27 similar results are shown for lead sludge samples, 100 Å diameter at 4.2° K. The transition temperature in lead is at 7.2° K and the bulk energy gap is at 22.5 cm^{-1}. This curve is practically indistinguishable from one taken at 9° or at 20° or at 1.2° K. These samples simply exhibit no temperature dependence nor effects of superconductivity.

The straight upper section extrapolates to zero at 12.5 ±1 cm^{-1} and there is the usual tail at low frequencies.

6. Discussion of the Data.

Table III gathers together the important points from the measurements. The first column gives the sample designation, the second its average diameter, the third the calculated value of Δ (all of these from Table II), the fourth the intercept of the more or less straight section with the x-axis which is an experimental value for Δ, the fifth the measured absorption coefficient at 40 cm^{-1}, and the last this absorption coefficient divided by f. Since the absorption coefficient more or less scales with f this might help to eliminate any effects of different packing densities on the data.

Considering the strong dependence of Δ on the diameter, the rough agreement of most of the samples between the calculated and experimental value is quite satisfactory. In the copper smoke the calculated value comes out quite a bit high; in the aluminum and tin somewhat low. The two sludge samples, surprisingly, were very close.

Although the absorption coefficients at 40 cm^{-1} do not follow

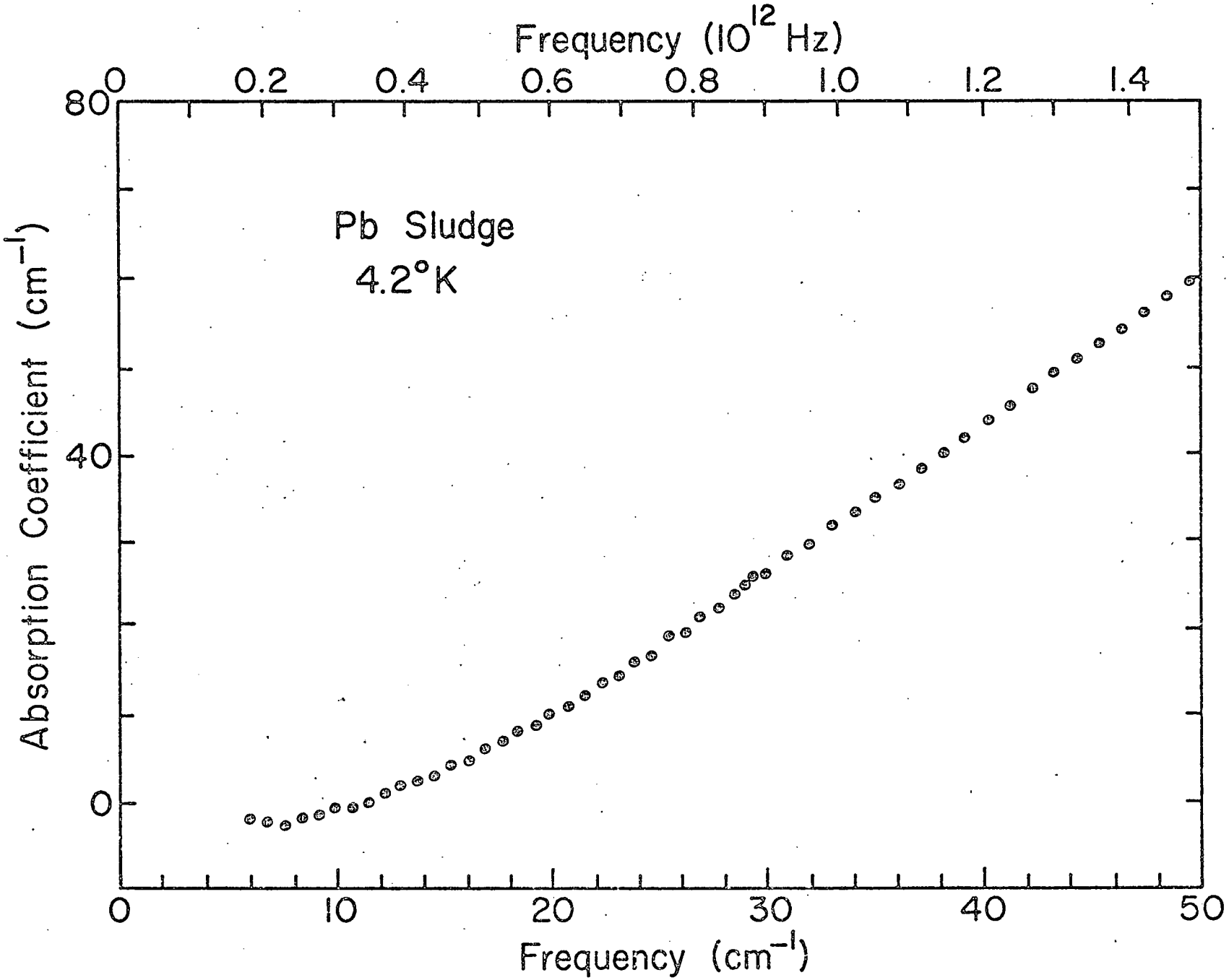

Fig. 27. Absorption coefficient versus frequency for Pb sludge below the bulk transition temperature.

TABLE III

EXPERIMENTAL DATA ON SMALL PARTICLES

Sample	Diameter A	Theoretical Δ cm^{-1}	Theoretical Δ meV	Experimental Δ cm^{-1}	Experimental Δ meV	Experimental Absorption at 40 cm^{-1} $\alpha(40\ cm^{-1})$	$\alpha(40\ cm^{-1})/f$
C	90	--	--	--	--	3.4	79
Cu 1	65	39	4.9	6.0±.5	.74	(50)	(2000)
Cu 2	70	31	3.9	19±1	2.4	2.7	97
Cu 3	270	.55	.068	<3	<.3	5.3	190
Cu sludge	100	11	1.3	11±1	1.4	46	370
Al 1	150	4.2	.51	13±1	1.6	5.0	125
Al 2	400	.22	.027	<3	.3	13.6	340
Al 3	375	.27	.033	<3	.3	10.4	260
Sn 1	140	8.9	1.1	13±1	1.6	2.4	130
Pb sludge	100	15	1.8	12.5±1	1.5	43	340

any pattern, dividing them by the filling factor, f, does bring them into order with a couple of exceptions. This number, α/f, is proportional to the absorption per particle rather than the absorption per centimeter of the collection and is shown in Figure 28. This is a log-log plot of the ratio of absorption coefficient to filling factor versus diameter for the particles. These data are shown as crosses in the figure and a dashed line is drawn through them. The line has a slope of 2/3 meaning that the absorption increases as $D^{2/3}$. Also in Figure 28 are the same data with the number for carbon subtracted off. These are shown as circles and fall into a somewhat straighter solid line with slope 3/2 ($\alpha \sim D^{3/2}$). Subtracting off the value for carbon is done in an attempt to eliminate the absorption from non-metallic causes and is of some value if the absorption due to carbon is independent of diameter. This is a somewhat shaky assumption. At any rate, the theory of Gor'kov and Eliashberg predicts that the absorption should increase in the metallic particles as D^3. The classical Mie theory predicts an absorption proportional to D^2. The result here of slope 2/3 or 3/2 is smaller than either. The numerical values of the absorption coefficients of the particles fall almost on the geometric mean between the Gor'kov-Eliashberg theory and the Mie theory. For 100 Å particles, a filling factor of .03 and at 40 cm^{-1}, the former gives an absorption coefficient of 200-350 cm^{-1}, the latter gives .1 and the experimental number, from Figure 28, is 3.

There are three samples that do not fit this variation of absorption versus diameter at all. The two sludge samples are

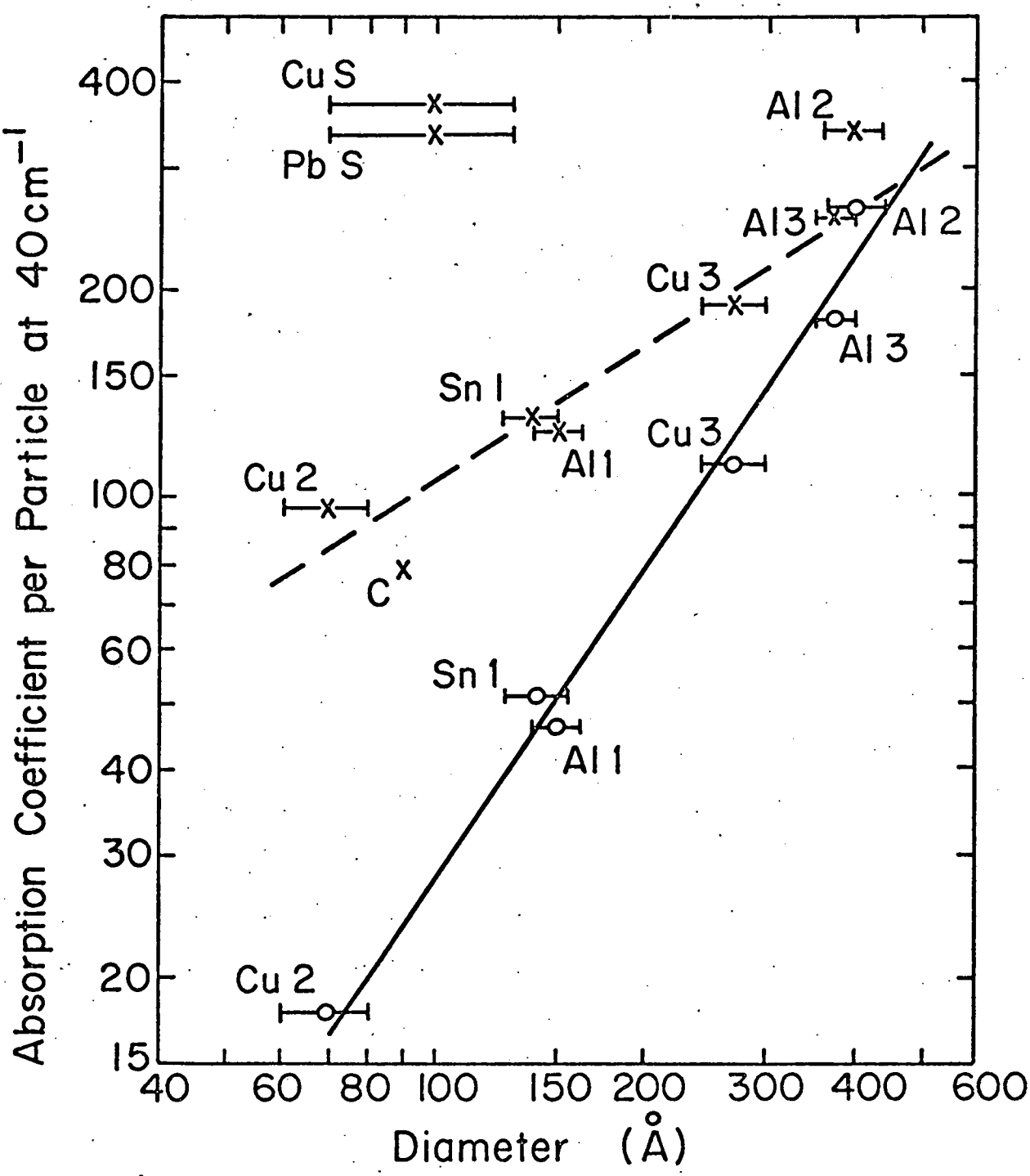

Fig. 28. Absorption coefficient divided by filling factor, at 40 cm^{-1}, versus diameter. The crosses and dashed line are the data; the circles and solid line are the data with the value for C subtracted off.

both a factor of three too large. These samples are not as clean as the others and this may be the result of a residue of acetone in them. Acetone is a strong absorber above 30 cm^{-1} but opens up and becomes transparent below 20 cm^{-1}. A much more serious difficulty arises in the case of Cu 1. This sample has an absorption coefficient some 20 times larger than Cu 2 which is about the same size. This was the only smoke sample measured which was made without oxygen in the bell jar. The electron microscope pictures seemed to show that the particles had clumped together. If these particles were not insulating they would act as larger particles and, with the absorption increasing with diameter these would make an impression on the measurement out of all proportion to their size. If this were true, however, the absorption coefficient should not level out at low frequencies but continue downwards as in Cu 3. The large value in Cu 1 remains a mystery.

The other major anamoly in the data is the structure in Al 1. This consists of very regular well resolved oscillations at 2.3 cm^{-1} intervals modulated by ones at 8.1 cm^{-1} intervals, producing a beating effect. In Fourier transform spectroscopy one must always be on guard against such behavior because it can be caused by two bad points in the interferogram or by two interference patterns in the sample. Both would be Fourier transformed into such a pattern. Neither of these is the case in Al 1. The pattern was visible in all of the spectra taken on Al 1 during two different runs separated by a period of a month and on none of the other samples run simultaneously. Because nine interferograms were recorded for Al 1 and because the pattern was

visible in all of them it was not due to two bad points in the interferogram. If it were due to an interference pattern, the pattern could only be in the Al 1 sample itself. Al 1 was one of five samples on a brass rotator disc which were placed in the far infrared beam successively. As the pattern was not observed in any of the other samples it must be localized in Al 1. Now, the way the samples were mounted was a piece of 1 mil thick polyethlene was placed over the hole in the brass sample rotator, a short section (perhaps one mm thick) of brass or nalgene tubing was put on it and the powder poured in, another sheet of polyethelene was used to cover the powder and the whole assembly held down with a piece of brass shim stock by screwing it to the rotator. It seems inconceivable that the two polyethelene sheets would be sufficiently flat and parallel to cause standing waves between them. It seems that the structure seen in Figure 25 is a property of the powder itself. The period of the oscillations is just about half of the calculated mean energy level spacing in Table II. Al 1 had the smallest percentage variation in size of any of the samples. It is the sample in which structure is most likely to be found.

As might be guessed, Al 2 was an attempt to duplicate the results of Al 1 with another sample. It turned out to be too large and too uneven in size. Al 1 must stand alone and is not completely understood.

A careful persual of Table II will show what is by now clear: that sample preparation is still somewhat of a hit or miss affair. For example, Al 2 while made in the same He pressure as Al 1 is larger than Al 3. Sn 2 was made in quite a bit larger pressures

than Sn 1 but is almost the same size. However, since all of the samples were examined under the electron microscope the diameters are well known and most of the features of the samples are a function of the diameter.

There is also some question about the oxygen on the surface of the particles. Electron microscope diffraction pictures show a double ring pattern typical of fcc copper and outside it a single ring identified as sc Cu_2O.[58] The density of this line is less than the copper line, implying that perhaps 10% of the particle is composed of the oxide. This oxide should be completely transparent at the far infrared frequencies of interest. It will reduce the diameter of the metallic small particle though. Two layers of oxide on the surface will reduce the diameter of the metal by 15 Å or so. This is not an insubstantial amount in the smaller particles. But, it is likely that the electrons can easily penetrate two layers of oxide (this being a typical layer in tunnel junctions) to reach the surface so that the volume of the small particle will be the same whether oxidised or not. The density of the electrons will be reduced proportionally to the number of electrons bound to oxygen atoms. The effect of the oxide will be to increase the energy level spacing.

One unexpected result of these experiments was the total lack of temperature dependence in the samples, at the temperatures studied. The copper and lead sludge samples were studied at 1.2°, 4.2°, 9°, and 20° K; the Cu 1 sample at 4.2°, 9°, and 25° K; Al 1 at 2° and 4.2° K; and Sn 1 and Sn 2 at 1.2° and 4.2° K. None of these showed any effects of temperature although a previously unknown temperature dependent absorption in quartz was found

during the course of these investigations. The superconducting samples did not change when cooled below their transition temperature.

As the frequency is increased the absorption continues to increase. Most of the samples studied were optimised in thickness for the 10 to 40 cm^{-1} region and did not transmit sufficient far infrared at higher frequencies to permit measurement of α there. One very thin copper sludge sample was measured in the near infrared at room temperature; it showed a continuing increase in the absorption with increasing feequency between 1000 and 4000 cm^{-1} (10 to 2.5 micron wavelength). In the visible at room temperature almost all of the small particle samples are black. Some of the larger ones show a slight blue-grayish tinge.

7. Summary and Conclusions.

Measurements of the absorption of small particles of copper, aluminum, tin, and lead in the frequency range of the mean energy level spacing of the electrons show qualitative agreement with the calculations of Gor'kov and Éliashberg. The absorption coefficient is near zero at low frequencies, bends up at the mean energy level spacing, and then increases with slight upward curvature as the frequency increases. One sample of aluminum showed structure at about the right interval to be due to the energy levels.

The magnitude of the absorption coefficient is much smaller than that calculated by Gor'kov and Éliashberg but larger than given by the classical Mie theory. The magnitude of α on a per

particle basis increases steadily with increasing diameter but does so more slowly than predicted by either theory.

The far infrared behavior of the small particles is found to be independent of temperature in the region 1.2^{o} to 25^{o} K. In particular the samples made of superconducting material do not change when cooled below their bulk transition temperature.

REFERENCES

Chapter I. Introduction

1. C. Kittel, Introduction to Solid State Physics, (Wiley, 1966), p. 206ff.
2. K. Wilson, Bull. Am. Phys. Soc. 17, 232 (1972).
3. R.E. Glover, Phys. Letters 25A, 542 (1967).
4. A. Schmid, Z. Physik 215, 210 (1968).
5. H. Schmidt, Z. Physik 216, 336 (1968).

Chapter II. Far Infrared Techniques and Apparatus.

6. W. Wolfe, ed. Handbook of Military Infrared Technology, (ONR, 1965), p. 10.
7. E. Hagen and H. Reubens, Ann. Physik 1, 352 (1900); 11, 873 (1903).
8. P. Fellgett, J. Phys. Radium 19, 187,237 (1958).
9. L. Strong and G.A. Vanasse, J. Opt. Soc. Am. 49, 844 (1959).
10. L. Genzel, J. Mol. Spectry 4, 241 (1960).
11. I.G. Nolt, Ph.D. Thesis, Cornell University (1967), Materials Science Center Report 765.
12. P.L. Richards, J. Opt. Soc. Am. 54, 1474 (1964).
13. R.D. Kirby, Ph.D. Thesis, Cornell University (1969), Materials Science Center Report 1122.
14. I.G. Nolt, R.D. Kirby, C.D. Lytle, and A.J. Sievers, Appl. Opt. 8, 309 (1969).
15. H.D. Drew and A.J. Sievers, Appl. Opt. 8, 2067 (1969).
16. H.D. Drew, Ph.D. Thesis, Cornell University (1968), Materials Science Center Report 939.
17. F.J. Low, J. Opt. Soc. Am. 51, 1300 (1961).
18. Digital Equipment Co., Maynard, Mass.
19. A.M. Kahan, Infrared Physics (to be published); Cornell University (1971), Materials Science Center Report 1697.

20. Arthur B. Little Co., Boston, Mass.

21. Princeton Applied Research Corp., Princeton, N.J.

22. John Fluke Co., Seattle, Wash. ("If it works its a Fluke").

23. R.A. Burhman, one of many private communications.

24. R.E. Glover and M. Tinkham, Phys. Rev. 108, 243 (1957).

25. R.E. Glover, Phys. Letters, 25A, 542 (1967).

26. R.A. Ferrell and H. Schmidt, Phys. Letters 25A, 542 (1967).

27. L.G. Aslamazov and A.I. Larkin, Phys. Letters 26A, 238 (1968); Sov. Phys. Solid State 10, 875 (1968).

28. D.C. Naugle and R.E. Glover, Phys. Letters 28A, 110 (1968).

29. M. Strongin, O.F. Kammerer, J. Crow, R.S. Thompson, and H.L. Fine, Phys. Rev. Letters 20, 922 (1968).

30. W.E. Masker and R.D. Parks, Phys. Rev. B 1, 2164 (1970).

31. K. Maki, Progr. Theoret. Phys. (Kyoto) 39, 897 (1968).

32. R.O. Smith, B. Serin, and E. Abrahams, Phys. Letters 28A, 224 (1968).

33. L.R. Testardi, W.A. Reed, P.C. Hohenberg, W.H. Haemmerle, and G.F. Brennert, Phys. Rev. 181, 800 (1969).

34. R.S. Thompson, M. Strongin, O.F. Kammerer, and J.E. Crow, Phys. Letters 29A, 194 (1969).

35. A. Schmid, Z. Physik 215, 210 (1968).

36. H. Schmidt, Z. Physik 216, 336 (1968).

37. H. Schmidt, Z. Physik 232, 442 (1970).

38. R.V. D'Aiello and S.J. Freedman, Phys. Rev. Letters 22, 515 (1969).

39. S.L. Lehoczky and C.V. Briscoe, Phys. Rev. B 4, 3938 (1971). Preliminary results were reported in Phys. Rev. Letters 23, 695 (1969) and Phys. Rev. Letters 24, 880 (1970).

40. For a discussion of the Ginsburg-Landau theory see P.G. de Gennes, Superconductivity of Metals and Alloys, (Benjamin, 1966), Chapter 6, or L.D. Landau and E.M. Lifshitz, Statistical Physics, (Addison-Wesley, 1958), Section 116.

41. E. Abrahams and T. Tsuneto, Phys. Rev. 152, 416 (1966).

42. C. Caroli and K. Maki, Phys. Rev. 159, 306 (1967).

43. A. Schmid, Phys. Kondens. Materie 5, 302 (1966).

44. P.C. Martin in DeWitt and Balian, eds., Many Body Physics, (Gordon and Breach, 1968).

45. R.A. Ferrell and R.E. Glover, Phys. Rev. 109, 1398 (1958).

46. G. Eilenberger, Z. Physik 236, 1 (1970).

47. B.R. Patton, Phys. Rev. Letters 27, 1273 (1971); Ph.D. Thesis, Cornell University (1971), Materials Science Center Report 1673; private communication.

48. M. Strongin, R.S. Thompson, O.F. Kammerer, and J.E. Crow, Phys. Rev. B 1, 1078 (1970).

49. K.L. Chopra, Thin Film Phenomena, (McGraw-Hill, 1969), p. 351ff.

50. E.H. Sondheimer, Advan. Phys. 1, 1 (1952).

51. G.D. Cody and R.E. Miller, Phys. Rev. 173, 481 (1968).

52. P.B. Miller, Phys. Rev. 118, 928 (1960).

Chapter IV. Small Particles

53. R. Kubo, J. Phys. Soc. Jap. 17, 975 (1962).

54. L.P. Gor'kov and G.M. Eliashberg, Sov. Phys. JETP 21, 940 (1965).

55. R. Denton, B. Muhlschlegel, and D.J. Scalapino, Phys. Rev. Letters 26, 707 (1971).

56. S. Kobayashi, T.Takahashi, and W. Sasaki, Phys. Letters 33A, 429 (1970), and to be published.

58. R.A. Buhrman, one of many private communications.

59. F.J. Dyson, J. Math. Phys. 3, 140, 157, 166 (1962) also M.L. Metha and F.J. Dyson, J. Math. Phys. 4, 713 (1963).

60. This is worked out in the simple case of interest here by L.D. Landau and E. M. Lifshitz, Electrodynamics of Continuous Media, (Addison-Wesley, 1960), Sections 72 and 73, and in more detail than anyone could ever want by M. Born and E. Wolf, Principles of Optics, (Pergamon, 1964), Section 13.5.

61. P.W. Anderson, J. Phys. Chem. Solids 11, 26 (1959).

62. M. Strongin, R. S. Thompson, O.F. Kammerer, and J.E. Crow, Phys. Rev. B 1, 1078 (1970).

63. A. Schmid, Z. Physik 231, 324 (1970).

64. J.P. Hurault, K. Maki, and M.T. Beal-Monod, Phys. Rev. B 3, 762 (1971).

65. H. Schmidt, Z. Physik 216, 336 (1968) and 232, 442 (1970).

66. Carbolac Corp., Boston, Mass.

APPENDIX A

FAR INFRARED MEASUREMENT OF THE ENERGY GAP OF V_3Si

1. Introduction

V_3Si is one of a family of binary intermetallic compounds which have some of the highest superconducting transition temperatures yet known. These compounds have the form M_3Y where M is a transition metal and Y is usually a semimetal or semiconductor. Certain of them, including V_3Si, undergo a cubic to tetragonal lattice phase transition[1] at temperatures above the superconducting transition. The two temperatures in the case of V_3Si are $T_m = 21\ ^oK$ (for the lattice or martensic transition) and $T_c = 17.1\ ^oK$ (for the superconducting transition).

Previous measurements of the energy gap of V_3Si and its sister compound Nb_3Sn have given varying results. Levinstein and Kunzler[2] measured both compounds by tunnelling from a sharp point contact into the sample. The Nb_3Sn was polycrystalline and gave the result $2\Delta = 3.6kT_c$. The V_3Si was a single crystal with the tunnelling in the 110 direction and usually gave $2\Delta = 1.8kT_c$ but the value $2\Delta = 3.8kT_c$ was also found. Hauser et al[3] measured the energy gap of a sputtered polycrystalline V_3Si film via the proximity effect on an Al-Pb tunnel junction and found $2\Delta = 3.8kT_c$. Hoffstein and Cohen[4] measured the gap in Nb_3Sn by tunnelling using the point contact method. The sample was a single crystal and the results varied depending on the direction of the tunnelling. The gap was a maximum in the 100 direction with $2\Delta = 2.8\ kT_c$. There was a minimum in

the 111 direction, with $2\Delta = 1.0kT_c$. In the 110 direction an intermediate result was found, $2\Delta = 2.2kT_c$. Bosomworth and Cullen[5] measured the far infrared reflectivity of a polycrystalline Nb_3Sn film. They found that the measured gap was strongly dependent on the state of preparation of the surface. It was initially at $2\Delta = 3.8kT_c$, was reduced by half by sanding, and then restored by chemical etching.

The crystal structure of V_3Si is called the β- tungsten or A15 form. It is basically cubic with Si atoms at each of the cube corners and one at the center. There are two V atoms on each of the cube faces, with two pairs (those on opposite faces) parallel to each of the cube edges. The result is that, when the cubes are stacked up to make a crystal, there are three mutually orthagonal groups of linear chains of vanadium atoms. These chains are pretty well separated from each other.

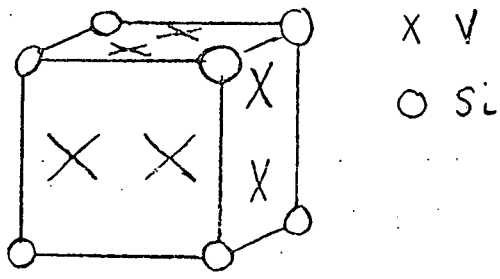

Figure A1. Crystal structure of V_3Si

It was this feature that led Labbé and Friedel[6] to propose their linear chain model for these compounds. In the case of V_3Si, the Fermi energy lies just above the bottom of a nearly empty d-band. There is a narrow peak in the density of states at the bottom of this band. The distance between the bottom of the band and the Fermi energy, $E_F - E_M$, is about 22 °K. This is much less than the Debye energy. Labbé and Friedel propose that it is this narrowness of the electronic spectrum

that provides the energy range limitations in these compounds, rather than the narrowness of the phonon spectrum. If so, the energy gap depends fairly closely on this difference. This simple model has been reasonably successful in explaining many of the properties of these compounds.

2. Experimental Techniques.

The experiments were done in the cryostat shown in Fig. A2. The samples were single crystal slabs of V_3Si which were grown in the MSC Materials Preparation facility at Cornell. The boule was generally cylindrical and it was sliced lengthwise several times with a spark cutter. The resulting thin slabs were chemically etched with a 50-50 mixture of HF and HNO_3. These pieces were then glued to the walls of the non-resonant cavity.

The incoming far infrared radiation from a lamellar grating interferometer enters the cavity through a condensing cone. This demagnifies the radiation and increases its half angle, as calculated by Williamson's[7] equation, from 18^o to 90^o. Once inside the radiation bounces around a few hundred times off of the sample and finds its way to the exit cone which converts it back to an 18^o half angle. From there it goes down a standard light pipe, through a quartz vacuum window to a helium three temperature bolometer-detector. A heater and carbon resistor are attached to the cavity, to allow the temperature to be adjusted and measured. Temperature isolation of the cavity from the detector was good enough that the

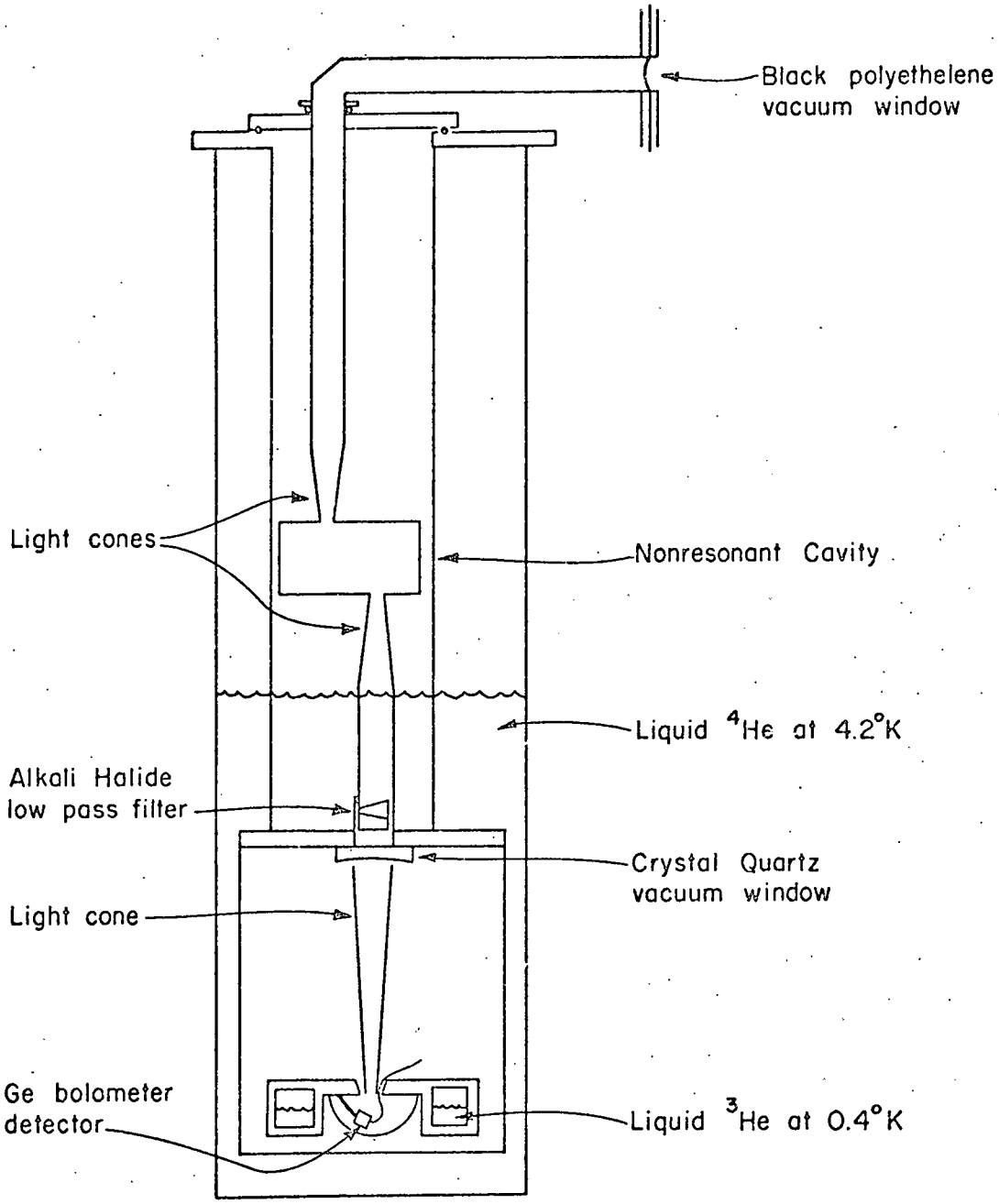

Fig. A2. Cryostat containing ^{3}He cooled bolometer and non-resonant cavity.

cavity could be heated above 30^{o} K without adversely affecting the detector.

The cavity is shown in cross section in Figure A2. It is a right circular cylinder, 1.5 cm in diameter and 4 cm long. The cones enter on the cylinder wall. The V_3Si slabs covered roughly ½ of the surface area.

The non-resonant cavity can be analysed in terms of its quality factor, Q, as discussed by Lamb[8] or Townes and Schallow.[9] This is defined as

$$Q = \frac{2\pi(\text{Energy Stored in Cavity})}{(\text{Energy lost per cycle}}$$

$$= \frac{\omega E}{-\frac{dE}{dt}}$$

If there are several loss mechanisms in the cavity they are just added reciprocally to find the reciprocal of the total Q. There are three such in this experiment: losses out the two holes, losses in the exposed brass walls of the cavity, and losses in the V_3Si samples mounted on the walls. For the holes

$$Q_{holes} = \frac{8\pi V}{\lambda A}$$

where V is the volume of the cavity and A the total area of the holes. For the walls

$$Q_{walls} = \frac{3\pi V R_o}{2\lambda\ SR}$$

where S is the surface area and R the surface impedance of the walls (whether brass or V_3Si) and R_o is the impedance of free space ($R_o = \frac{4\pi}{c} = 377\Omega$). Then

$$\frac{1}{Q} = \frac{1}{Q_{holes}} + \frac{1}{Q_{brass\ walls}} + \frac{1}{Q_{V_3Si\ walls}}$$

The transmitted intensity going to the detector is

$$I = \frac{Q}{\frac{1}{2}Q_{holes}} I_o$$

In this experiment the transmission of the cavity was measured at two temperatures, one with the V_3Si superconducting and one with it normal, and the ratio of these taken to eliminate any frequency dependence not due to the sample. So,

$$\frac{I_S}{I_N} = \frac{Q_S}{Q_N} = \frac{3AR_o + 16S_BR_B + 16SR_N}{3AR_o + 16S_BR_B + 16SR_S}$$

In the event that $\frac{16S_BR_B}{3AR_o} << 1$ $\frac{16SR_N}{3AR_o} << 1$

$$\frac{I_S}{I_N} = 1 + \frac{16S}{3AR_o}(R_n - R_s)$$

and the impedance difference, $R_n - R_s$, is proportional to the intensity ratio minus one.

What these inequalities mean is that the transmission of the cavity must not change a great amount if the simple formula is to hold. This is indeed the case in these experiments.

3. Experimental Results.

The difference in surface impedance between the normal and the superconducting states in ohms as a function of frequency in cm^{-1} is shown in Figure A3. The experimental points are shown as points; a few have error bars on them. Resolution is 1.5 cm^{-1} The superconducting data were taken at 4.2° K and the normal state data at 20° K. The rise at the lowest frequencies is due to absorption in the normal metal, which increases with

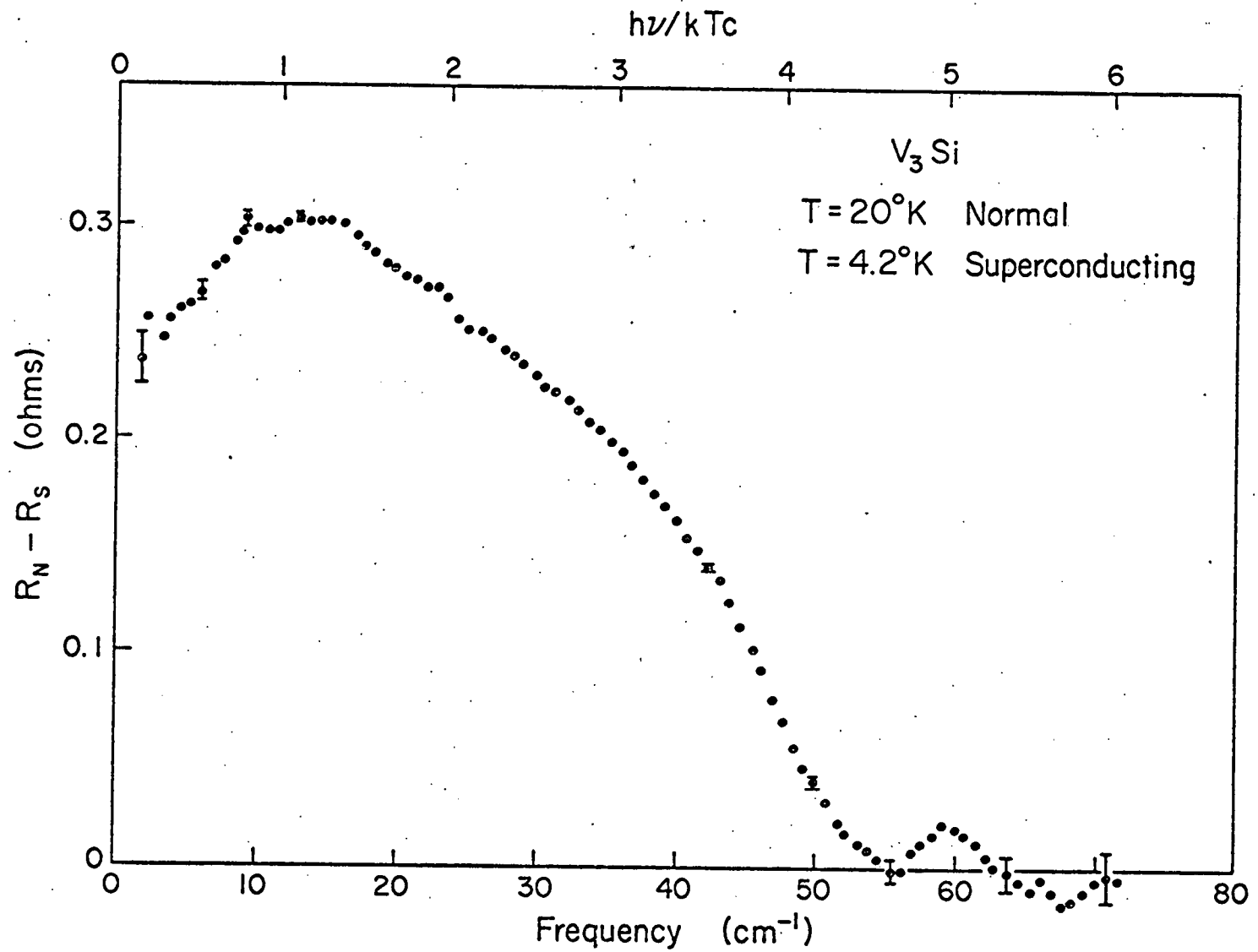

Fig. A3. Difference between normal and superconducting states surface impedance versus frequency for V_3Si.

frequency. The peak at 12 cm^{-1} (=1.0 kT_c) indicates the frequency at which the superconductor begins to absorb; the surface impedance of the normal metal continues to rise, but that of the superconductor rises more steeply still, so that the difference falls as the frequency increases. This fall attains its steepest slope at 46 cm^{-1} (=3.8kT_c). At 53 cm^{-1} the superconductor absorbs as strongly as the normal metal, and the difference continues near zero to our upper frequency limit.

Now, in any superconductor the surface impedance does not jump immediately to the normal state value at the gap frequency, but rather rises with finite slope, these being typically, by experiment[10]

$$\left(\frac{\omega_g}{R_N}\frac{dR_S}{d\omega}\right)_{\omega=\omega g} = 4$$

This slope decreases at higher frequencies. Acording to the BCS form of the conductivities the surface impedance should reach the normal state value at twice the gap frequency; it generally does so much sooner. The maximum slope of the surface impedance occurs at the gap frequency. It is probably justified to take the maximum value of the energy gap in V_3Si at the frequency where the surface impedance difference has the maximum slope.

The next figure (Figure A4) shows the surface impedance difference at various temperatures. As the temperature is increased the height of the peak is reduced and shifts to lower frequencies. The zero impedance difference and the point of maximum slope also shift to lower frequencies, although the latter is difficult to see on this figure. In the little box at the bottom of the figure shows the results when the metal is normal at both temperatures. The surface impedance at 27° K

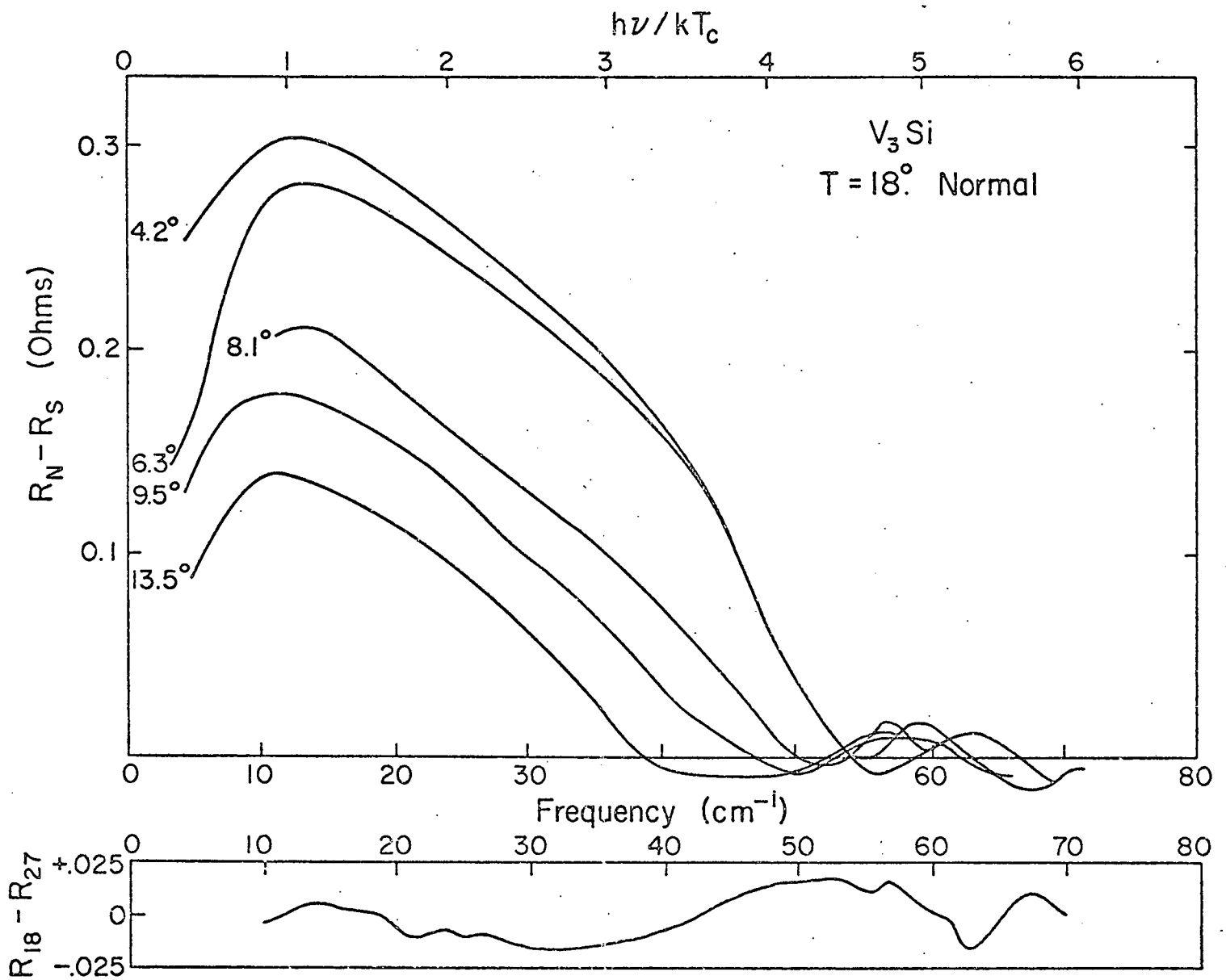

Fig. A4. Surface impedance difference versus frequency for V_3Si at several temperatures.

differs from that at 18° K by at most a small amount. It was once suggested that the lattice phase transition was driven by a soft optic mode. This should be visible as an extra absorbtion if this were the case. Within the limits of the far infrared sensitivity there is no evidence for this; no consistent structure is seen in such normal-normal differences. This is pretty much of a dead horse though as there has been shown to be a soft acoustic mode instead.

In Figure A5 is shown the temperature dependence of the three important frequencies. The upper curve is for the zero impedance difference intercept, ν_3, the middle curve for the maximum slope of the surface impedance, ν_2, and the lower curve for the peak, ν_1, where the superconductor begins to absorb. The solid lines show the BCS expression for the temperature dependence of the energy gap, scaled to go through T_c and the points at 4.2° K.

4. Summary and Conclusions.

Measurements of the surface impedance as a function of far infrared frequency at various temperatures on single crystal V_3Si show a very anisotropic energy gap. The gap at 4.2° K extends from $2\Delta = 1.0kT_c$ to $2\Delta = 3.8kT_c$. This takes in the whole range of reported gap values from tunnelling measurements in V_3Si. Both the upper and the lower value for the energy gap seem to follow the BCS form as a function of temperature and both have the same transition temperature.

A disadvantage of these experiments is that it is not

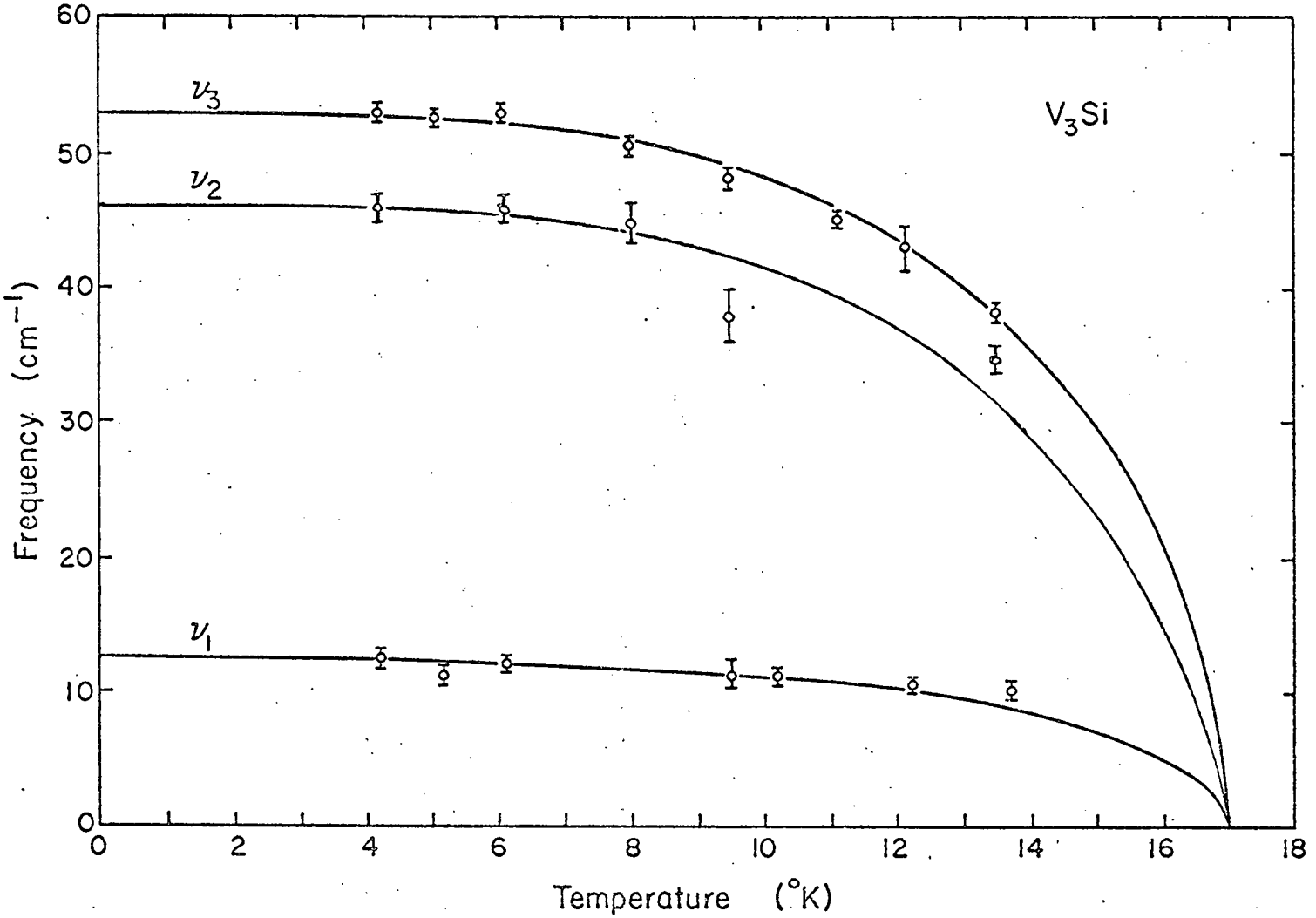

Figure A5. Temperature dependence of the peak (ν_1), the point of maximum slope (ν_2), and the zero intercept (ν_3) of the impedance difference curves.

possible to assign a particular gap value to a given crystal direction as was done in tunnelling experiments.[4] A counter-balancing advantage is that the state of the surfaces is less important. In these extreme type II superconductors the coherence length is much less than the penetration depth. In V_3Si $\xi_o \sim 40$ Å while $\lambda \sim 2000$Å. Tunnelling measurements probe the material to the depth of the coherence length while far infrared radiation goes into the penetration depth. It would be expected then that the far infrared measurements would be much less affected by damage to the surface.

APPENDIX B

INFRARED PROPERTIES OF METALS

1. Maxwell's Equations

The purpose of this appendix is to discuss how the conductivity of a metal is connected to the measured properties thereof. The conductivity is generally the result of a theoretical calculation whereas it is not usually directly measured in the far infrared frequency region. What is measured is variously the reflection, transmission, impedance, phase shift, or optical constants of the metal,depending of the geometry. The connection may be made between the experimental and theoretical quantities by solving Maxwell's equations in the metal and applying the appropriate boundary conditions.

The first step is to stick the complex conductivity into Maxwell's equations. As soon as one begins to talk about the conductivity it means that the discussion is limited to the local limit, when there is a point relation between the currents and the fields; the metal is in the normal skin effect region. Fortunately, all of the systems discussed in this thesis are in this limit. There will be no discussion here of the anamolous skin effect here.

Maxwell's equations are a set of four differential and three constituative equations relating the four field vectors, $\vec{D}$, $\vec{E}$, $\vec{B}$, and $\vec{H}$, to each other and to the charge density, ρ, and current, $\vec{j}$. In Gaussian units they are

$$\nabla \cdot \vec{D} = 4\pi\rho$$

$$\nabla \cdot \vec{B} = 0$$

$$\nabla \times \vec{E} = -\frac{1}{C}\frac{\partial \vec{B}}{\partial t}$$

$$\nabla \times \vec{H} = \frac{4}{C}\vec{J} + \frac{1}{C}\frac{\partial \vec{D}}{\partial t}$$

$$\vec{D} = \varepsilon_1 \vec{E} \quad \vec{J} = \sigma_1 \vec{E} \quad \vec{B} = \mu \vec{H}$$

where ε_1 is the (real) dielectric constant, σ_1 is the (real) conductivity, and μ is the permeability ($\mu = 1$ from now on) of the medium. Using an $e^{-i\omega t}$ time dependence, the curl equations become

$$\nabla \times \vec{E} = \frac{i\omega}{C}\vec{H}$$

$$\nabla \times \vec{H} = \frac{4\pi}{C}\sigma_1 \vec{E} - i\frac{\omega}{C}\varepsilon_1 \vec{E}$$

At this point various authorities diverge. Tinkham[11] defines the imaginary parts of the conductivity and dielectric constant by

$$\sigma = \sigma_1 + i\sigma_2 = \frac{i\omega}{4\pi}(\varepsilon_1 + i\varepsilon_2) = -\frac{i\omega}{C}\varepsilon$$

$$\sigma_2 = -\frac{\omega\varepsilon_1}{4\pi}$$

so that

$$\nabla \times \vec{H} = \frac{4\pi}{C}(\sigma_1 + i\sigma_2)\vec{E}$$

Sokolov[12] does the same thing with the complex polarizability, χ_e, defined by $\varepsilon = 1 + 4\pi\chi e$

$$\sigma = \sigma_1 + i\sigma_2 = -i\omega(\chi_{e_1} + i\chi_{e_2}) = -i\omega\chi_e$$

$$\sigma_2 = -\omega\chi_{e_1} = -\frac{\omega(\varepsilon_1 - 1)}{4\pi}$$

and

$$\nabla x\vec{H} = \frac{4\pi}{C}(\sigma_1+i\sigma_2)\vec{E}-\frac{i\omega}{C}\vec{E}$$

The first term is the current arising from free (mobile) charges, the second from bound charges (polarization current) and the third has to do with pure displacement current (not involving charges).

Donovan[13] merely puts

$$\sigma = \sigma_1 + i\sigma_2$$

directly into the equation in place of σ_1, which seems pretty simple. But then he has to argue that ε_1 is the dielectric constant of the bare lattice. It is then around one and

$$\nabla x\vec{H} = \frac{4\pi}{C}(\sigma_1 + i\sigma_2)\vec{E} - \frac{i\omega}{C}\vec{E}$$

We should now compare $4\pi\sigma_2$ with ω

$$\frac{4\pi\sigma_2}{\omega} = \frac{4\pi\sigma_o\tau}{1+\omega^2\tau^2} = \frac{\omega_p{}^2\tau^2}{1+\omega^2\tau^2}; \qquad \omega_p{}^2 = \frac{4\pi ne^2}{m} = 4\pi\sigma_o/\tau$$

The pure displacement term in Maxwell's fourth equation only becomes important in the vicinity of the plasma frequency, e.g. up in the visible or near ultraviolet. It may be safely ignored. Finally,

$$\nabla x\vec{E} = \frac{i\omega}{C}\vec{H}$$

$$\nabla x\vec{H} = \frac{4\pi}{C}(\sigma_1+i\sigma_2)\vec{E}$$

There are two commonly used models for the conductivity are the Drude model for a normal metal and the BCS model of a superconductor.

2. Drude Model

In the drude model the electrons are treated as a gas of noninteracting particles which are damped by collisions with defects or phonons in the lattice. The collisions result in a relaxation time τ. The conductivities may easily be calculated by writing an equation for the drift velocity, $\vec{v}_d$ of an electron.

$$m\left(\frac{d}{dt} + \frac{1}{\tau}\right) \vec{v}_d(t) = \vec{F} = e\vec{E}e^{i\omega t}$$

If $\vec{v}_d(t) = \vec{v}_d(0)e^{i\omega t}$

$$m\left(-i\omega + \frac{1}{\tau}\right) \vec{v}_d = -eE$$

The current is

$$\vec{J} = \sigma\vec{E} = -ne\vec{v}_d = \frac{ne^2\tau}{m} \quad \frac{1}{1-i\omega\tau}$$

where n is the number of freee electrons per unit volume. Then

$$\sigma = \sigma_o \frac{1}{1-i\omega\tau}$$

where $\sigma_o = \frac{ne^2\tau}{m}$ in the dc conductivity. Taking the real and imaginary parts yields

$$\sigma_1 = \frac{\sigma_o}{1+\omega^2\tau^2} \qquad \sigma_2 = \frac{\sigma_o \omega \tau}{1 + \omega^2\tau^2}$$

The same result can be obtained with a little more difficulty from the Bolzman equation.[13]

3. Superconductors

A superconductor has no dc electrical resistance while the reflectivity in the near infrared or visible regions is not affected as the metal passes from the normal to the superconducting states.[11] There is an energy gap in the excitation

spectrum of a superconductor and a photon can only be absorbed if it has energy greater than the energy gap. The energy gap of most superconductors lie, at T = 0^{o} K, in the far infrared or microwaves. For example, that of lead is at 22.5 cm^{-1}.

The conductivity of a superconductor was first calculated in the BCS model by Mattis and Bardeen,[14] and by Abrikosov, Gor'kov, and Khalatnikov.[15] Mattis and Bardeen calculated the real and imagninary parts of the conductivity at T = 0^{o} K in terms of complete elliptic integrals. Numerical calculations at finite temperature have been performed by Miller.[16] These are shown in Figures B1 and B2 in the case of a superconductor with T_c = 7.2^{o} K and an energy gap of 22.5 cm^{-1}(lead).

At zero temperature there is a delta function in the real part of conductivity at $\omega = 0$. It is then zero until the gap frequency where it begins to rise up towards the normal state value. The imaginary part goes as $1/\omega$ and is one at the gap frequency. As the temperature is raised the delta function in σ_1 broadens and the gap is reduced towards zero. The overall magnitude of the imaginary part is reduced but the shape remains pretty much the same.

A sum rule for the real part of the superconducting conductivity has been discussed by Ferrell and Glover[17] and Tinkham and Ferrell.[18] It follows from the Kramers Kronig transforms and from requiring that the imaginary part of the conductivity be independent of the superconductivity if the frequencies are taken to infinity (an experimentally observed effect) that the integral over frequency of the real part of

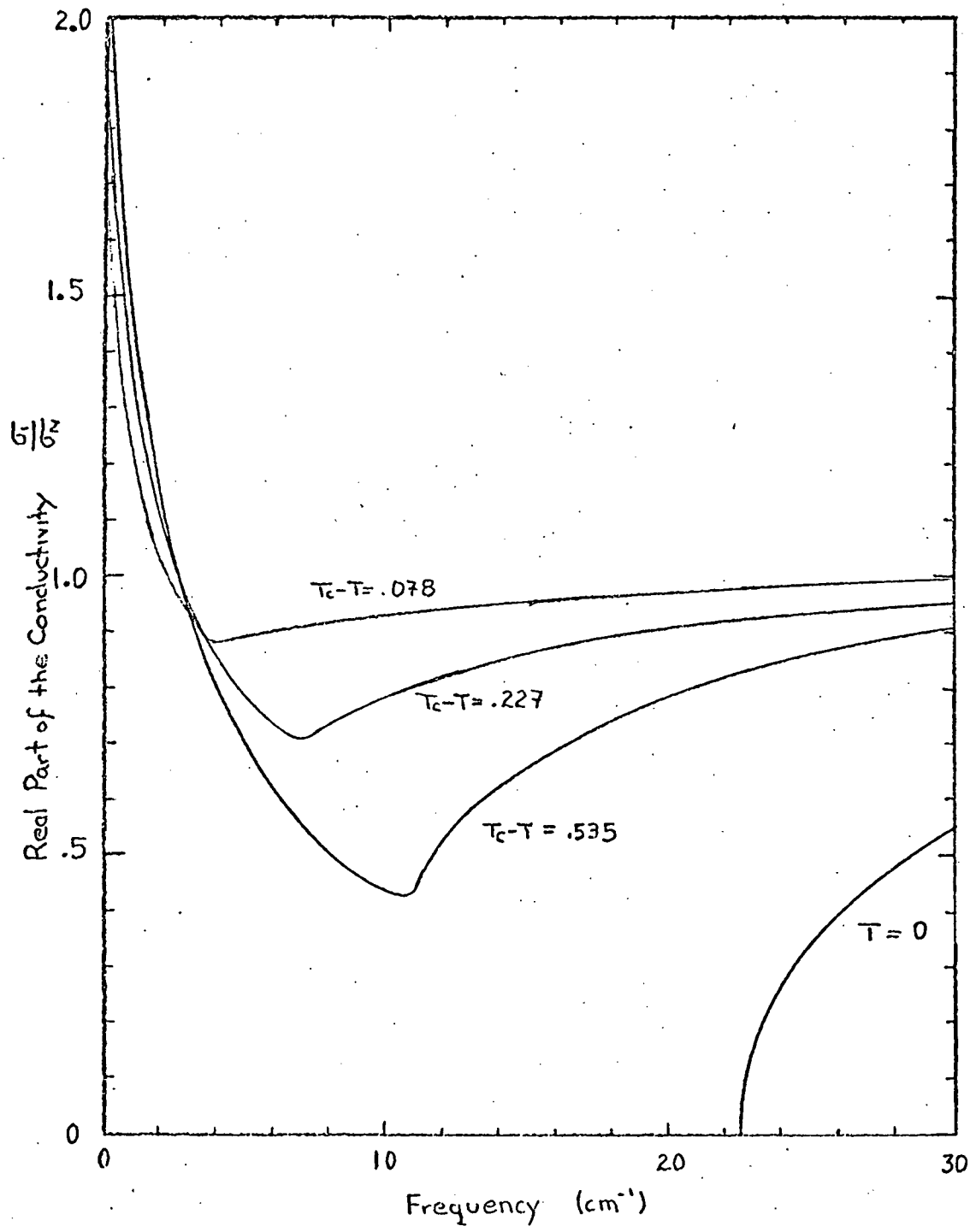

Fig. B1. Real part of the conductivity of a superconductor versus frequency.

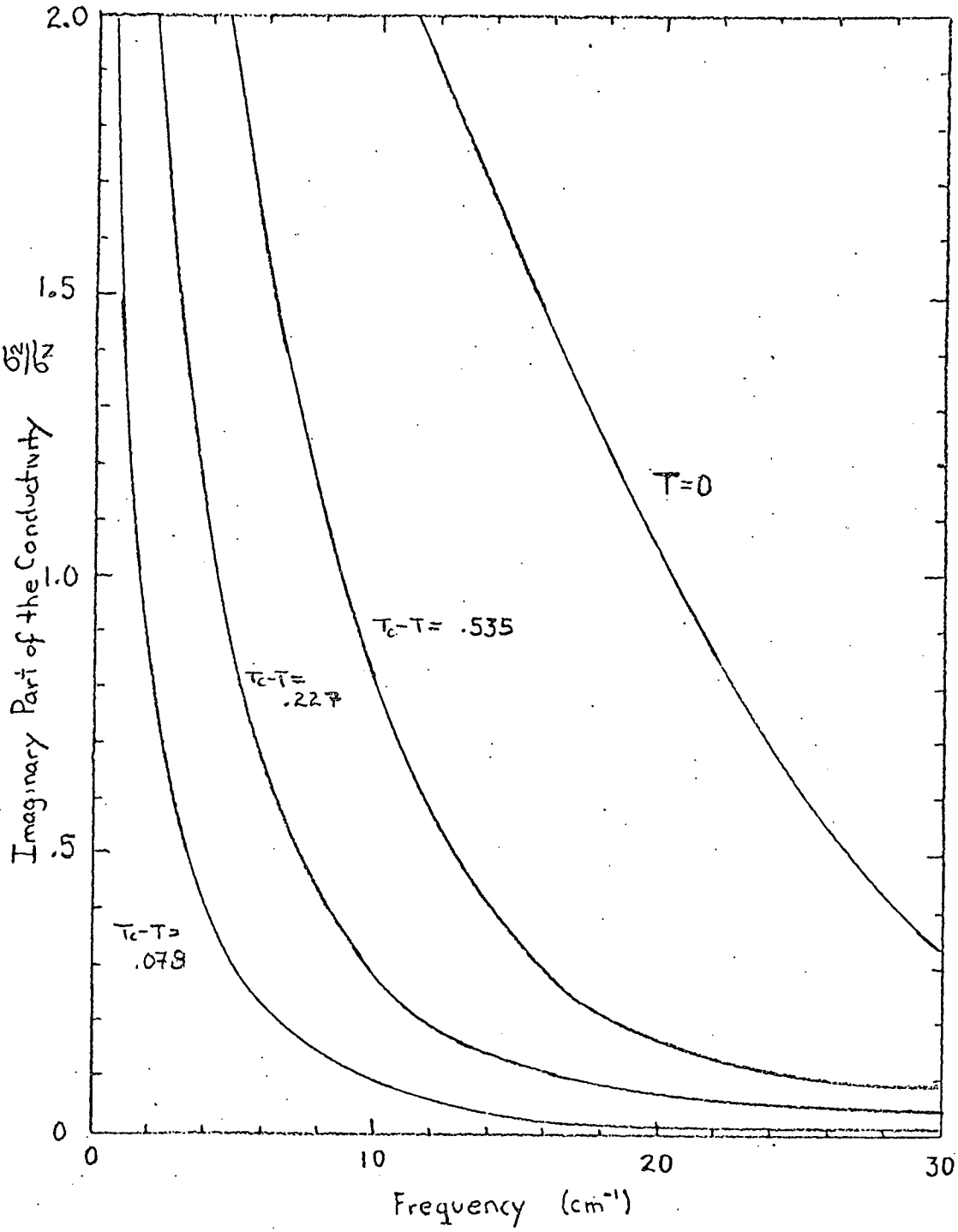

Figure B2. Imaginary part of the conductivity of a superconductor versus frequency.

the conductivity is independent of the superconducting transition.

$$\int_0^\infty \sigma_S(\omega)\,d\omega \quad \int_0^\infty \sigma_N(\omega)\,d\omega = \frac{\pi}{2}\,\frac{ne^2}{m}$$

4. Bulk Material.

This is the first of several sections dealing with the classical electromagnetic behavior of samples of various geometries and dimensionalities. In it will be discussed the reflectivity, skin depth, surface impedance and fields in the interior of a bulk metal. Later will come discussions of thin films and small particles.

Consider the arrangement shown in Figure B3 at right. This is the geometry that will be used in the rest of this appendix. All waves will be propagating in the plus or minus z direction, the normal to the interface (the x-y plane). The radiation is plane polarized with the electric field along the x direction and the magnetic field along the y direction. The propagation direction, the electric field and the magnetic field

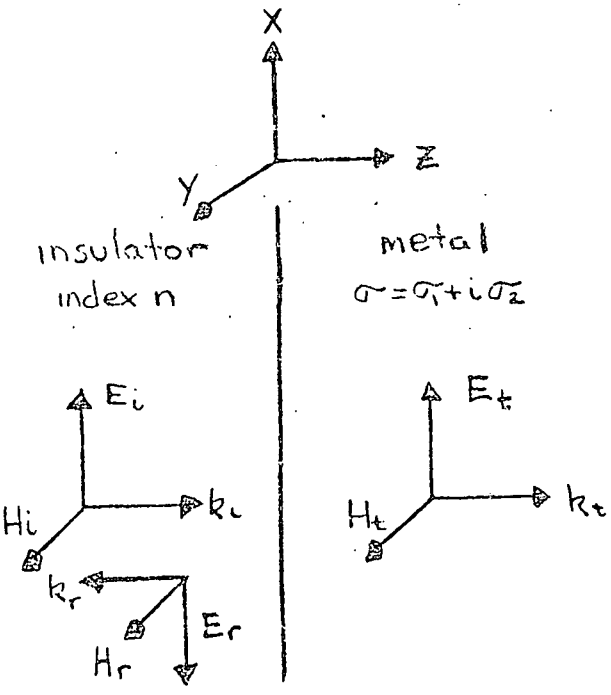

Figure B3. Metal-insulator Boundary

form a right handed set. Inside the insulator, of index n, there is an incoming wave

$$\vec{E}_i = E_o \hat{x} e^{i\frac{n\omega}{c} z} \qquad \vec{H}_i = nE_o \hat{y} e^{i\frac{n\omega}{c} z}$$

and a reflected wave

$$\vec{E}_r = -r E_o \hat{x} e^{-i\frac{n\omega}{c} z} \qquad \vec{H}_r = nr E_o \hat{y} e^{-i\frac{n\omega}{c} z}$$

where we have had to decide the phase of the reflected electric vector. There is a 180^o phase reversal on reflection from a more dense medium. One way to see this is to say that for a perfect conductor, which is a perfect reflector, the tangential component of the electric field at the surface must be zero. This requires the electric field in reflected wave at the surface to be in the opposite direction to that in the incoming wave, i.e. a 180^o phase reversal.

Inside the metal there is a damped transmitted wave

$$\vec{E}_t = E\hat{x} e^{iN\frac{\omega}{c} z} \qquad \vec{H}_t = H\hat{y} e^{iN\frac{\omega}{c} z}$$

where E and H are constants to be determined by the boundary conditions at the surface. N is a complex propagation constant. Then,

$$\nabla x \vec{E}_t = \hat{y}\, i \frac{N\omega}{c} E = \frac{i\omega}{c} \hat{y} H$$

$$H = NE$$

$$\nabla x \vec{H}_t = -\hat{x} i \frac{N\omega}{c} E = \frac{4\pi}{c}(\sigma_1 + i\sigma_2)\hat{x}E$$

$$N^2 = i\frac{4\pi}{\omega}(\sigma_1 + i\sigma_2)$$

If $N = \eta + ik$

$$\eta^2 - k^2 = -\frac{4\pi}{\omega}\sigma_2 \qquad 2\eta k = \frac{4\pi}{\omega}\sigma_1$$

and

$$\eta = \left(\frac{2\pi}{\omega}\right)^{\frac{1}{2}} \left(\sqrt{\sigma_1^2 + \sigma_2^2} - \sigma_2\right)^{\frac{1}{2}}$$

$$k = \left(\frac{2\pi}{\omega}\right)^{\frac{1}{2}} \left(\sqrt{\sigma_1^2 + \sigma_2^2} + \sigma_2\right)^{\frac{1}{2}}$$

The boundary conditions on E and H are that the tangential components of both be continuous across the boundary ($z = 0$).

$$E_o(1-4) = E$$

$$nE_o(1+r) = NE = N\,E_o(1-r)$$

$$r = \frac{N-n}{N+n}$$

This is the amplitude reflection component. To find the intensity or power reflection coefficient the Poynting vector for the incoming and reflected waves must be calculated. At present it doesn't matter, because both incoming and reflected waves are in the same medium, but it will matter later so I will do it correctly now. The Poynting vector is

$$\vec{S} = \frac{c}{4\pi}\,\vec{E} \times \vec{H}^*$$

The intensity reflection coefficient is the ratio of magnitudes of reflected and incoming Poynting vector. If n is a unit normal vector

$$\mathcal{R} = \frac{\vec{S}_r \cdot \hat{n}}{\vec{S}_i \cdot \hat{n}} = \frac{(rE_o)(nr^*E_o)}{(E_o)(n\,E_o)} = |r|^2$$

$$\mathcal{R} = \frac{(\eta - n)^2 + k^2}{(\eta + n)^2 + k^2}$$

as expected. This is the usual result. Notice that if $\omega t << 1$ (low frequency or bad conductor) and if $n = 1$ then $\sigma_2 = 0$, $\sigma_1 = \sigma_o >> \omega$ and

$$\eta = k = \left(\frac{2\pi}{\omega}\sigma_o\right)^{\frac{1}{2}}$$

$$\mathcal{R} = \frac{(1-(\frac{\omega}{2\pi\sigma_o}))^2 + 1}{(1 + (\frac{\omega}{2\pi\sigma_o}))^2 + 1} \approx 1 - 2\left(\frac{\omega}{2\pi\sigma_o}\right)^{\frac{1}{2}}$$

The absorptivity is

$$\alpha = 1 - \mathcal{R} \approx 2\left(\frac{\omega}{2\pi\sigma_o}\right)^{\frac{1}{2}}$$

This is the result found by Hagen and Reubens[19] in the first far infrared experiments on metals.

The propagation constant N is, reasonably enough, called the complex index of refraction. There are two other concepts that come out of it very easily. The skin depth is a measure of the distance that radiation penetrates into the metal. If one substitutes N into the equation for $\vec{E}_t$

$$\vec{E}_t = \hat{x}\,\frac{2n}{N+n}\,E_o e^{i\frac{\omega}{C}Nz} = \hat{x}\,\frac{2n}{N+n}\,E_o\, e^{i\frac{\omega}{C}\eta z}\, e^{-\frac{\omega}{C}kz}$$

The skin depth δ is defined as the damping length of the field in the metal

$$\delta = \frac{c}{\omega k}$$

In the low frequency limit, when $k = \left(\frac{2\pi\sigma_o}{\omega}\right)^{\frac{1}{2}}$

$$\delta_o = \left(\frac{c^2}{2\pi\sigma_o\omega}\right)^{\frac{1}{2}}$$

is the classical skin depth.

The surface impedance is defined in terms of the ratio of the electric to magnetic fields at the surface of the metal.

$$z = R + i\chi \equiv \frac{4\pi}{C}\frac{E(0)}{H(0)} = \frac{4\pi}{c}\frac{1}{N}$$

$$= \frac{4\pi}{c}\frac{\eta - ik}{\eta^2+k^2}$$

The quantity $\frac{4\pi}{c} \equiv Z_o$ is called the impedance of free space and is equal to 377 Ω in practical units.

In the low frequency limit, when $\eta = k = \left(\frac{2\pi\sigma_o}{\omega}\right)^{\frac{1}{2}}$

$$Z = \left(\frac{2\pi\omega}{c^2\sigma_o}\right)^{\frac{1}{2}}(1-i)$$

$$= \frac{1}{\sigma_o\delta}(1-i)$$

5. Simple Theory of the Transmission of a Film.

Before going into the detailed and involved calculation of the transmission of a thin film, I would first like to present a simple calculation based on the boundary conditions of the field vectors as this is easier to follow. The film will be treated as a surface sheet of current. This calculation is valid if the film thickness is much less than the skin depth, the wavelength, and any other characteristic lengths in the system.

The geometry is shown in Figure B4. The incoming wave has

amplitudes E_o and H_o, $H_o = E_o$, the reflected wave has amplitudes E_r and H_r $H_r = E_r$ and the transmitted wave has amplitudes E_t and H_t, $H_t = nE_t$. Then the vectors E_o and E_r are anti-parallel again and

$$E_r = -rE_o$$

$$E_t = tE_o \qquad \text{defining } r, t$$

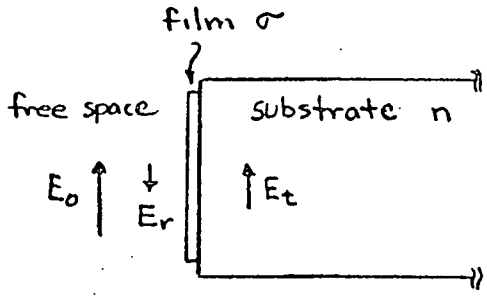

Figure B4. Thin film geometry

The boundary condition on the electric field is that the tangential components are continuous across the boundary (the film)

$$(E_o - E_r) - E_t = 0$$

$$1 - r - t = 0$$

The boundary condition on the magnetic field is that the tangential component be discontinuous by the surface current at the interface (in the film)

$$(H_o + H_r) - H_t = \frac{4\pi}{c} K$$

where K is the surface current. It is the current per unit area and is equal to the current per unit volume times the film thickness

$$\frac{4\pi}{c} K = \frac{4\pi}{c} jd = (1 + r - t)E_o$$

Now $j = \sigma E$ where E is the field in the film. This is either tE_o or $(1-r)E_o$ which are the fields on either side and which are (by the boundary conditions) equal.

$$\frac{4\pi}{c}\, dt = (1 + r - t)$$

$$t = \frac{2}{n + 1 + \frac{4\pi}{c}\sigma d}$$

$$r = \frac{n-1 + \frac{4\pi}{c}\sigma d}{n+1 + \frac{4\pi}{c}\sigma d}$$

These are the amplitude transmission and reflection coefficients. To calculate the intensity coefficients it is again necessary to use the Poynting vector. The transmission is

$$\mathcal{T} = \frac{\vec{S}_t \cdot \hat{n}}{\vec{S}_o \cdot \hat{n}} = \frac{\vec{E}_t x \vec{H}_t^* \cdot \hat{n}}{\vec{E}_o x \vec{H}_o^* \cdot \hat{n}} = \frac{(t\, E_o)(nt^* E_o)}{E_o^2}$$

$$= n|t|^2$$

$$= \frac{4n}{|n + 1 + \frac{4\pi}{c}\sigma d|^2}$$

$$= \frac{4n}{(n+1 + \frac{4\pi}{c}\sigma_1 d)^2 + (\frac{4\pi}{c}\sigma_2 d)^2}$$

The reflection is

$$\mathcal{R} = \frac{\vec{S}_r \cdot \hat{n}}{\vec{S}_o \cdot \hat{n}} = |r|^2$$

$$= \frac{(n-1 + \frac{4\pi}{c}\sigma_1 d)^2 + (\frac{4\pi}{c}\sigma_2)^2}{(n+ 1 + \frac{4\pi}{c}\sigma_1 d)^2 + (\frac{4\pi}{c}\sigma_2 d)^2}$$

And the absorbtion is

$$\mathcal{A} = 1 - \mathcal{R} - \mathcal{T}$$

$$= \frac{\frac{16\pi}{c}\sigma_1 d}{(n + 1 + \frac{4\pi}{c}\sigma_1 d)^2 + (\frac{4\pi}{c}\sigma_2 d)^2}$$

proportional to σ_1 as might be expected.

The above are the results for an infinitely thick substrate. If the substrate has a rear surface (as it usually does) the effects of the reflections at the rear surface, including multiple internal reflections must be taken into account. This is done here for a thick substrate. This is one which is either thick or has the front and rear surfaces out of parallel compared to the wavelength of the radiation in the substrate, eg $d>>\frac{\lambda}{n}$ or $\Delta d>\frac{\lambda}{n}$. If this is the case, then the phase of multiple internal reflections need not be considered, the amplitudes add incoherently, and one merely adds intensities.

With regard to the figure at right, the front surface has coefficients $\mathcal{T}_1$ and $\mathcal{R}_1$ and the rear surface has $\mathcal{T}_2$ and $\mathcal{R}_2$, then by adding up the reflections back and forth inside the transmission and reflection of the entire assembly can be found.

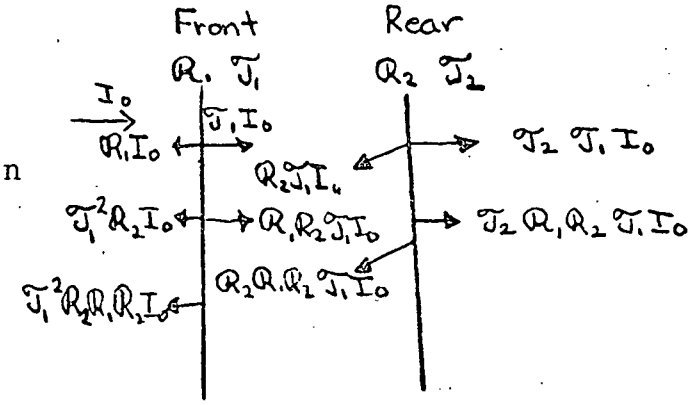

Figure B5. Multiple internal reflections

$$\mathcal{T}_A = \mathcal{T}_1 \mathcal{T}_2 \, (1 + \mathcal{R}_1\mathcal{R}_2 + \mathcal{R}_1^2\mathcal{R}_2^2 + \ldots)$$

$$= \frac{\mathcal{T}_1 \mathcal{T}_2}{1-\mathcal{R}_1\mathcal{R}_2}$$

$$\mathcal{R}_A = \mathcal{R}_1 + \mathcal{T}_1^2 \mathcal{R}_2 \, (1 + \mathcal{R}_1\mathcal{R}_2 + \mathcal{R}_1^2\mathcal{R}_2^2 + \ldots)$$

$$= \mathcal{R}_1 + \frac{\mathcal{R}_2 \mathcal{T}_1^2}{1-\mathcal{R}_1\mathcal{R}_2}$$

For an insulator of index n, no film

$$\mathcal{T}^A = \frac{4n}{(n+1)^2} \qquad \mathcal{R}^A = \frac{(n-1)^2}{(n+1)^2}$$

For a thin film on a substrate

$$\mathcal{T}^A =$$

$$\frac{16n^2}{(n+1)^2\left((n+1 + \frac{4\pi}{c}\sigma_1 d)^2 + (\frac{4\pi}{c}\sigma_2 d)^2\right) + (n-1)^2\left((n-1 + \frac{4\pi}{c}\sigma_1 d)^2 + (\frac{4\pi}{c}\sigma_2 d)^2\right.}$$

The expressions for the reflection and absorption are even more complicated and are not reproduced here. All three coefficients are shown in Figure B6 plotted versus film impedance for a film in which $\sigma_2 = 0$, $\sigma_1 = \sigma_o$ (eg a normal metal film at far infrared frequencies). The substrate has index n = 2 in this calculation. The impedance $R^{\square} = 1/\sigma_o d$ is the resistance that the film would have if it were square. Comparing the far infrared transmission

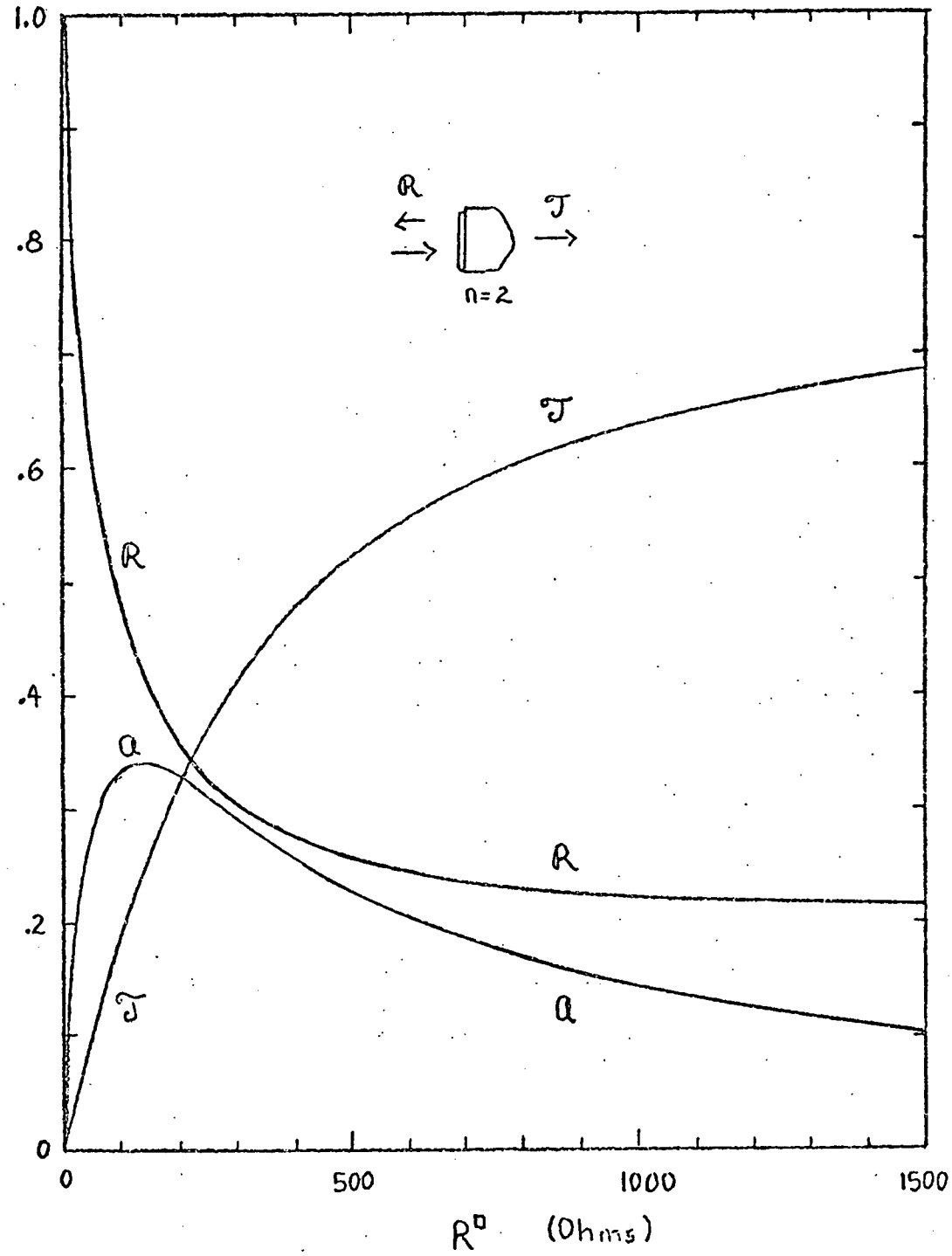

Fig. B6. Transmission, reflection, and absorption coefficients of a thin film on a substrate versus the square resistance of the film.

of the substrate assembly before and after film deposition allows the determination of the square resistance of the normal metal film.

6. Transmission of a film.

The general problem of the transmission and reflection of a film has been worked out by various authors interested in reflection and transmission interference filters. The earliest and clearest modern work that I know of is the paper by Hadley and Dennison.[20]

The problem now is to calculate the fields in three regions for normal incidence. A sketch of the arrangement is shown in Figure B7 at right. The three regions, free space, metal film, and substrate have altogether five travelling waves in them. The whole problem involves matching boundary conditions at the two boundaries z = 0 and z = d.

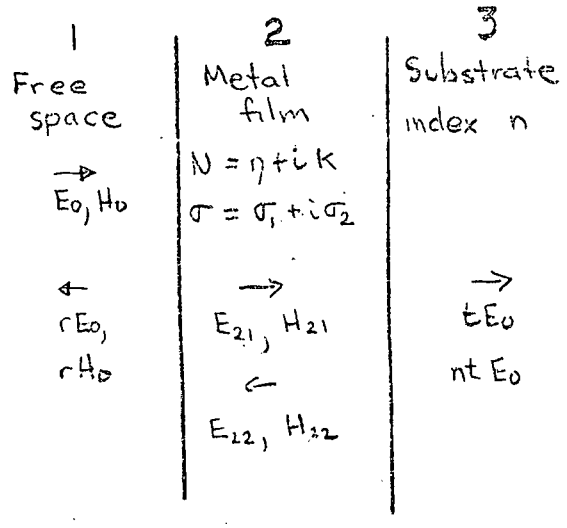

Figure B7. Thin Metal Film on Substrate

In region 1 there is an incoming wave and a reflected wave

$$\vec{E}_1 = E_0 \hat{x}\left(e^{i\frac{\omega}{c}z} - r\, e^{-i\frac{\omega}{c}z}\right)$$

$$\vec{H}_1 = E_0 \hat{y}\left(e^{i\frac{\omega}{c}z} + r\, e^{-i\frac{\omega}{c}z}\right)$$

Similarly in region 2

$$\vec{E}_2 = E_{21}\hat{x}\, e^{iN\frac{\omega}{c}z} + E_{22}\hat{x}\, e^{-iN\frac{\omega}{c}z}$$

$$\vec{H}_2 = H_{21}\hat{y}\, e^{iN\frac{\omega}{c}z} + H_{22}\hat{y}\, e^{-iN\frac{\omega}{c}z}$$

From the solution of Maxwell's equations inside the metal

$$H_{21} = NE_{21} \qquad H_{22} = -NE_{22}$$

where the minus sign is required to keep the right handed plane wave. In region three there is only a single wave

$$E_3 = t\, E_o\hat{x}\, e^{in\frac{\omega}{c}z}$$

$$H_3 = nt\, E_o\hat{x}\, e^{in\frac{\omega}{c}z}$$

The boundary conditions are

$$E_1 = E_2 \qquad H_1 = H_2 \qquad \text{at } z = 0$$

$$E_2 = E_3 \qquad H_2 = H_3 \qquad \text{at } z = d$$

Applying these at $z = 0$

$$E_o(1-r) = E_{21} + E_{22}$$

$$E_o(1+r) = NE_{21} + NE_{22}$$

At $z = d$

$$E_{21}\, e^{iN\frac{\omega}{c}d} + E_{22}\, e^{-iN\frac{\omega}{c}d} = t\, E_o e^{in\frac{\omega}{c}d}$$

$$NE_{21} e^{iN\frac{\omega}{c}d} - NE_{22} e^{-iN\frac{\omega}{c}d} = tn\, E_o e^{in\frac{\omega}{c}d}$$

These four equations may be solved for the four unknown E_{21}, E_{22}, r, t

$$E_{21} = \frac{2(N+n)\, e^{-iN\frac{\omega}{c}d}}{(N+n)(N+1)\, e^{-iN\frac{\omega}{c}d} - (N-1)(N-n)\, e^{iN\frac{\omega}{c}d}}$$

$$E_{22} = \frac{2(N-n)\, e^{iN\frac{\omega}{c}d}}{(N+n)(N+1)\, e^{-iN\frac{\omega}{c}d} - (N-1)(N-n)\, e^{iN\frac{\omega}{c}d}}$$

$$r = \frac{(N-1)(N+n)\, e^{-iN\frac{\omega}{c}d} - (N+1)(N-n)\, e^{iN\frac{\omega}{c}d}}{(N+1)(N+n)\, e^{-iN\frac{\omega}{c}d} - (N-1)(N-n)\, e^{iN\frac{\omega}{c}d}}$$

$$t = e^{-iN\frac{\omega}{c}d} \frac{4N}{(N+1)(N+n)\, e^{-iN\frac{\omega}{c}d} - (N-1)(N-n)\, e^{iN\frac{\omega}{c}d}}$$

The calculation of the power transmission and reflection coefficients is then a tedious but straight forward algebraic task. They are

$$\mathcal{T} = ntt^* \qquad \mathcal{R} = rr^*$$

as before. The easiest way to attack the problem is to carry out

the complex conjugation and multiplication first before substituting N = n+ik. Then substitute and collect terms, and you will find, forging ahead, that the expression is indeed real and that all of the exponentials have become sines and cosines of either the circular or hyperbolic variety. The result is:

$$\mathcal{T} =$$

$$\frac{8(\eta^2+k^2)n}{((\eta^2+k^2+n^2)(\eta^2+k^2+1)+4n\eta^2)\cosh 2d\frac{\omega}{c}k + 2\eta(n+1)(\eta^2+k^2+n)\sin h\ 2d\frac{\omega}{c}k}$$

$$\cdots\cdots\cdots\cdots\cdots\cdots\cdots\cdots$$

$$-((\eta^2+k^2-n^2)(\eta^2+k^2-1)-4nk^2)\cos 2d\frac{\omega}{c} + 2k(n+1)(\eta^2+k^2+n)\sin 2d\frac{\omega}{c}$$

The expression for the reflectivity has the same denominator and an equally large numerator, is not needed here, and is left as an exercise for the reader.

If, now, one puts in the long wavelength approximation

$$\eta = k = \left(\frac{2\pi\sigma}{\omega}\right)^{\frac{1}{2}} \text{ and } 2d\frac{\omega}{c}k = 2d/\delta << 1$$

one recovers the transmission equation from the simple boundary value problem.

$$\mathcal{T} = \frac{4n}{(n+1+\frac{4\pi}{c}\sigma d)^2}$$

This is the transmission of the film into the substrate as before. To calculate the transmission of the entire film and

substrate assembly, use, as before, the equation of the transmission of a thick substrate.

7. Non-normal Incidence.

The effect of rays not normal to the film surface has little effect of the angles are not too big. It is then necessary to consider two cases depending on whether the electric field vector is parallel or perpendicular to the plane of incidence (the plane defined by the normal to the film and by the direction of electromagnetic propagation). The final result is from Hadley and Dennison:[20]

$$\mathcal{T}_{\perp} = \frac{4n(1-\sin^2\theta)^{\frac{1}{2}}\left(1-\frac{\sin^2\theta}{n^2}\right)^{\frac{1}{2}}}{\left| n\left(1-\frac{\sin^2\theta}{n^2}\right)^{\frac{1}{2}} + (1-\sin\theta^2)^{\frac{1}{2}} + \frac{4\pi}{c}\sigma d\right.}$$

$$\mathcal{T}_{\parallel} = \frac{4n\,(1-\sin\theta^2)^{\frac{1}{2}}\left(1-\frac{\sin\theta^2}{n^2}\right)^{\frac{1}{2}}}{\left| n(1-\sin^2\theta)^{\frac{1}{2}} + \left(1-\frac{\sin^2\theta}{n^2}\right)^{\frac{1}{2}} + \frac{4\pi}{c}\sigma d\right.}$$

For a spectrometer with f/1.4 optics the maximum half angle of the radiation with the axis of the system is 18°. Now $\sin(18^{\circ})$ is .09 so the correction $(1-\sin^2 18^{\circ})^{\frac{1}{2}}$ is .95. The main effect, then of off axis rays is to reduce the apparant index of refraction of the substrate by 5%, or, equivalently, increase the apparent structures of the film by the same amount.

8. Zero Dimensional Samples.

The problem of the optical properties of small metallic particles (samples where all the dimensions are smaller than the wavelength of the light)was first considered by Mie[21] and Debye.[22] It is worked out in great detail by Born and Wolf.[23] For the case in which I am interested the problem is given in a simpler form by Landau and Lifshitz.[24] This is when the particles are spherical and the wavelength of the radiation inside the sample is longer than the sample dimensions. The interior wavelength is the skin depth

$$\delta = \frac{\lambda}{n} = \left(\frac{c^2}{2\pi\sigma_o\omega}\right)^{\frac{1}{2}}$$

where

$$n = \left(\frac{2\pi\sigma_o}{\omega}\right)^{\frac{1}{2}}$$

Typically for millimeter wave radiation(λ = .1 cm), $\sigma_o = 10^{18}$ sec^{-1} and $\omega = 10^{12}$ sec^{-1} so that $n = 10^3$-10^4. The ultra long wavelength case obtains for particles with diameter 1000 Å or less.

There are two mechanisms that must be considered which will reduce the intensity of radiation transmitted through an array of small particles, scattering and absorption. Of course, scattering does not reduce the energy of the light; it merely removes it from the beam. For a detector with large diameter optics such as any far infrared one the maximum energy that can be removed by scattering alone is the ratio of the square of the acceptance angle to 4π. If there are f/1.4

optics then a large amount of scattering reduces the transmitted intensity to .06 the incident value. Because scattering increases the effective path length through the medium it enhances any absorption mechanism.

Because of the large wavelength the field around the particle is quasi static. It causes the particle to be polarized. This gives rise to fields at large distances; these are the scattered radiation. The fields at great distance R are

$$\vec{E}' = \frac{\omega^2}{c^2 R} (\vec{P} + \vec{M} \times \hat{n})$$

$$\vec{H}' = \hat{n} \times \vec{E}'$$

and where $\vec{P}$ and $\vec{M}$ are evaluated at retarded time t - R/c. The energy flow per unit time unit area in the direction of n is the time average poynting vector

$$\vec{S}' = \frac{c}{4\pi} \vec{E}' \times \vec{H}'$$

The intensity scattered into a solid angle $d\Omega$ is

$$dI + (\vec{S}' \cdot \hat{n}) R^2 d\Omega = \frac{\omega^4}{c^4} V^2 (|\chi_e^2 + \chi_m^2|) I_o$$

where $I_o = \frac{c}{4\pi} E_o^2$ is the incoming flux density, and χe and χm are the electric and magnetic polarizabilities. These can be calculated in this case from the static boundary value problem because of the extreme long wavelength. They are

$$\chi_e = \frac{-3}{4\pi} \frac{\varepsilon - 1}{\varepsilon + 2} = \frac{3}{4\pi} \frac{-4\pi\sigma_2 - \omega + i4\pi\sigma_1}{-4\pi\sigma_2 + 2\omega + i4\pi\sigma_1}$$

$$\chi_m = \frac{3}{8\pi} \{1 - 6i(\frac{\delta}{D})^2 + 3(1+i) \frac{\delta}{D} \cot((1+i)\frac{D}{2\delta})\}$$

where $\delta = (\frac{c^2}{2\pi\sigma\omega})^{\frac{1}{2}}$. In this case $\delta << D$ and

$$\chi_m = -\frac{\pi}{420}\frac{D^4\sigma^2\omega^2}{c^4} + i\frac{D^2\sigma\omega}{4Dc^2}$$

It can be neglected with respect to the electric term.

The differential scattering cross section is

$$ds = \frac{\omega^4}{c^4} V^2(|\chi_e|^2 + |\chi_m|^2)\sin^2\theta d\Omega$$

$$= \frac{9}{16\pi^2}\frac{\omega^4}{c^4} V^2 \sin^2\theta d\Omega \qquad \sigma_1 >> \sigma_2, \omega$$

The total cross section for scattering is

$$S = \frac{8\pi}{3}\frac{\omega^4}{c^4} V^2(|\chi_e|^2 + |\chi_m|^2)$$

$$= \frac{3}{2}\frac{\omega^4}{c^4} V^2$$

The absorbtion cross section is given by the tatio of energy dissipated per unit time (Q) to the incident energy per unit area unit time (S).

$$Q = -\vec{D}\cdot\frac{\partial\vec{E}}{t} - \vec{M}\cdot\frac{\partial H}{\partial t}$$

$$= \tfrac{1}{2} V(\chi_{e_2} + \chi_{m_2})|E|^2$$

where χ_{e_2} and χ_{m_2} are the imaginary parts of the electric and magnetic polarizibilities respectively. Then

$$S = \frac{2\pi}{c}\omega V(\chi_{e_2} + \chi_{m_2})$$

$$\chi_{e_2} = \frac{9\omega\sigma_1}{(4\pi\sigma_1)^2 + (4\pi\sigma_2 - 2\omega)^2}$$

$$\chi_{m_2} = \frac{D^2\sigma\omega}{4Dc^2}$$

If $\sigma >> \sigma_2, \omega$

$$\chi_{e_2} = \frac{9\omega}{16\pi^2\sigma_1} \qquad \chi_{m_2} = \frac{D^2\sigma_1\omega}{40c^2}$$

and

$$S = \frac{2\pi^2}{3c} D^3\omega^2\sigma_1 \left(\frac{9}{16\pi^2\sigma_1^2} + \frac{D^2}{40c^2}\right)$$

This calculation has found the cross section for one particle while the experiment gives the absorbtion coefficient for an array of 10^{18} particles. The absorbtion coefficient, α, is

$$\alpha = \frac{N}{V}\sigma$$

where N/V is the number density of the particles.

The transmitted intensity through the array is

$$I = I_o e^{-\alpha\ell} = I_o e^{-\sigma\frac{N}{V}\ell} = I_o e^{-\sigma\frac{N}{A}}$$

where I_o is the incident intensity, is the length of the sample, and N/A is the number of particles per unit area normal to the beam.

APPENDIX C

LINEAR RESPONSE THEORY

1. General.

Linear response theory is a version of time dependent perturbation theory applied to statistical systems. It has been discussed in detail in connection with correlation functions by Martin.[25] In this appendix I will attempt to show how to use it to find the connection between the current correlation function and the conductivity used in Chapter III. This will draw heavily on a set of lecture notes and a problem from Wilkins.[26]

2. The Density Operator

It is required to calculate the change in the expectation value of an operator J from its equilibrium value due to the application of a weak time dependent external perturbation $H_1(t)$. Given $|\alpha\rangle$ a complete set of states and P_α the probability that the system is in the α^{th} state, the density operator is defined as

$$\rho = \sum_\alpha P\alpha|\alpha\rangle\langle\alpha|$$

The expectation value of an operator J is

$$\langle J\rangle = T_r\ \rho J = \sum_\beta \langle\beta|\rho J|\beta\rangle \quad \sum_\alpha P\alpha\langle\beta|\alpha\rangle\langle\alpha|J|\beta\rangle$$

where the $|\beta\rangle$ are any complete set of states. Now the Schroedinger equation is

$$i\hbar \frac{\partial}{\partial t} |\alpha\rangle = H|\alpha\rangle$$

which implies

$$i\hbar \frac{\partial}{\partial t} \rho = (H,\rho)$$

Now, to do perturbation theory write $H = H_o + H_1, \rho = \rho_o + \rho_1$. H_o is the (solvable) unperturbed Hamiltonian and ρ_o is the density operator appropriate to it. ρ_o is independent of H_1 and ρ_1 is proportional to it. One likes to work in the interaction representation; it is convenient to put the time dependence of H_o into ρ. So define

$$\rho^I = e^{\frac{i}{\hbar}Hot} \rho e^{-\frac{i}{\hbar}Hot} = \rho_o + \rho_1{}^I$$

$$H^I = e^{\frac{i}{\hbar}Hot} H e^{-\frac{i}{\hbar}Hot} = H_o + H_1{}^I$$

and, neglecting terms of order $H_1{}^2$

$$ih \frac{\partial}{\partial t} \rho_1{}^I = (H_1{}^I, \rho_o)$$

3. Change of an Observable.

To find the change in the operator J when the time dependent perturbation is turned on, suppose that this is done slowly from time $t = -\infty$. The change in the expectation value of J is then

$$\langle \delta J^I(t) \rangle = \langle J^I(t) \rangle_H - \langle J^I(t) \rangle_{Ho} = T_r \rho J - \langle J^I(t) \rangle_{Ho}$$

$$= T_r \, \rho_1{}^I(t) \, J(t)$$

To find the value of $\rho_1{}^I$ at any time, integrate the equation for the time derivative of it in terms of the commutator of $H_1{}^I$ and ρ_o. to find

$$\rho_1{}^I(t) = -\frac{i}{\hbar} \int_{-\infty}^{t} (H_1{}^I(t'), \rho_o) dt' = -\frac{i}{\hbar} \int_{-\infty}^{\infty} \theta(t-t') (H_1{}^I(t'), \rho_o) dt'$$

and $$\langle \delta J^I(t) \rangle = -\frac{i}{\hbar}\int_{-\infty}^{\infty} dt' \theta(t-t')\ T_r\{(H_1^I(t'), \rho_o) J^I(t)\}$$

$$= -\frac{i}{\hbar}\int_{-\infty}^{\infty} dt' \theta(t-t')\ T_r\{\rho_o (J^I(t), H_1^I(t'))\}$$

using commutation properties of the trace.

4. The Perturbation Hamiltonian.

Let

$$H^I(t) = J^+(t)U(t)$$

Where $J^+(t)$ is the Hermitian conjugate of the observable J and U(t) is an external potential. At this point also drop the superscript I.

5. Fourier Transforming

With the above changes, the Fourier transform of the change in the expectation value of J is

$$\langle \delta J(\omega) \rangle = \frac{1}{2\pi\hbar}\int_{-\infty}^{\infty} dt \int_{-\infty}^{\infty} dt' \int_{-\infty}^{\infty} d\ ' \frac{e^{-i\omega'(t-t')}}{\omega' + ie} U(t') \langle [J(t), J^+(t')] \rangle_o e^{i\omega t}$$

since the $\theta(t-t')$ is

$$\theta(t-t') = i\int_{-\infty}^{\infty} \frac{d\omega'}{2\pi} \frac{e^{-i\omega(t-t')}}{\omega' + i\varepsilon}$$

Make the following change of variables

$$\omega' \to \omega - \omega\ ,\ \int_{-\infty}^{\infty} d\omega' \to \int_{-\infty}^{\infty} d\omega'$$

$$t \to t + t',\ \int_{-\infty}^{\infty} dt \to \int_{-\infty}^{\infty} dt$$

$$\langle \delta J(\omega) \rangle = \frac{1}{2\pi\hbar} \int_{\infty}^{\infty} dt' U(t') e^{i\omega t'} \int_{\infty}^{\infty} \frac{d\omega'}{\omega-\omega'+ie} \int_{\infty}^{\infty} dt\ e^{i\omega' t} \langle [J(t+t'), J^{+}(t')] \rangle_{0}$$

Notice that the expectation value of the commutator is taken in the unperturbed system. (The density operator which was used was ρ_0) Because of this its value can only depend on the difference of the arguments, t+t'-t, only. In that expectation value the arguments can be set to t and 0 respectively. The the first integral is just the Fourier transform of the potential, $U(\omega)$.

$$\langle \delta J(\omega) \rangle = U(\omega) \frac{1}{2\pi\hbar} \int_{\infty}^{\infty} \frac{d\omega'}{\omega-\omega'+ie} \int_{\infty}^{\infty} dt\ e^{i\omega' t} \langle [J(t), J^{+}(0)] \rangle_{0}$$

$$\equiv U(\omega)\ \ \chi(\omega)$$

with $\chi(\omega)$ defined appropriately.

The complex function $\chi(\omega)$ can be shown to satisfy the Kramers-Kronig relations by doing the following integral in the ω'' UHP

$$\int_{C} d\omega'' \frac{\chi(\omega'')}{\omega''-\omega} = 0$$

$$= i\pi\chi(\omega) + P\int_{-\infty}^{\infty} \frac{\chi(\omega'')\, d\omega''}{\omega''-\omega}$$

or

$$\mathrm{Im}\chi(\omega) = \frac{1}{\pi} P\int_{-\infty}^{\infty} \frac{\mathrm{Re}\chi(\omega'')\, d\omega''}{\omega''-\omega}$$

$$\mathrm{Re}\chi(\omega) = \frac{1}{\pi} P\int_{-\infty}^{\infty} \frac{\mathrm{Im}\chi(\omega'')\, d\omega''}{\omega''-\omega}$$

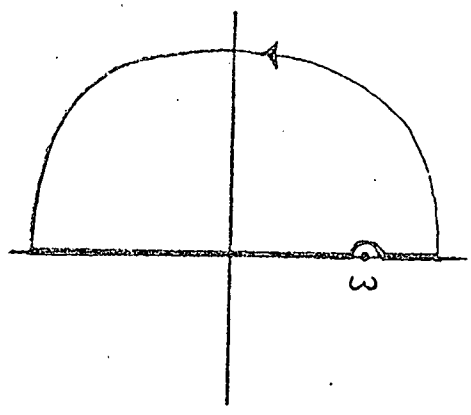

Figure C1. Contour for Kramers-Kronig

6. Electromagnetic Behavior

The frequency dependent conductivity is calculated by considering the change in the expectation value of the current operator $J(x,t)$ due to an external vector potential $A(x,t)$. The pertubation Hamiltonian is

$$H_1 = -\frac{1}{c} \int d^3x \, \vec{J}(\vec{x},t) \cdot \vec{A}(\vec{x},t)$$

Except for the vector notation and the integral, this looks like (mirable dictu!) the H_1 used earlier. The electrical conductivity is defined by

$$J\mu(\vec{q},\omega) = \sigma\mu\nu(\vec{q},\omega) \left\{\frac{\omega}{c} A\nu(\vec{q},\omega)\right\}$$

where

$$J\mu(\vec{q},\omega) = \frac{1}{V} \int d^3x \, dt \, e^{-i(\vec{q}\cdot\vec{x}-\omega t)} \, J\mu(\vec{x},t)$$

The gauge used is the one where $\phi = 0$ and

$$\frac{i\omega}{c} A\nu(\vec{q},\omega) = E\nu(\vec{q},\omega)$$

The gauge $\vec{A} = \vec{0}$ could also be used.

Since there are no currents without the external perturbation

$$\langle J\mu(\vec{q},\omega)\rangle = \langle \delta J\mu(\vec{q},\omega)\rangle$$

$$= -\frac{1}{2\pi chV} \int d^3x e^{-i\vec{q}\cdot\vec{x}} \int d^3x' \vec{A}(x',\omega) \cdot \int_{-\infty}^{\infty} \frac{d\omega'}{\omega-\omega'+i\delta} \int_{-\infty}^{\infty} dt e^{i\omega' t}$$

$$\langle \left[J\mu(\vec{x},t), \vec{J}(\vec{x},0)\right]\rangle_o$$

The translational symmetry of the system requires that

$\langle J\mu(x,t)J\nu(x',0)\rangle$ depend only on $|\vec{x}-\vec{x}'|$. Using the

convolution theorem,

$$F(\vec{x}) = \int dt' g(\vec{x}-\vec{x}')\mathcal{H}(x') = F(\vec{q}) = g(\vec{q})\mathcal{H}(\vec{q}),$$

the expectation value of the current immediately becomes

$$\langle J\mu(\vec{q},\omega)\rangle = \frac{\vec{A}(\vec{q},\omega)}{2\pi c\hbar V}\cdot \int_{\infty}^{\infty}\frac{d\omega'}{\omega-\omega'-i\delta}\int_{\infty}^{\infty}dt e^{i\omega' t}\langle\left[J\mu(\vec{q},t),\ \vec{J}(-\vec{q},0)\right]\rangle_o$$

and

$$\sigma_{\mu\nu}(\vec{q},\vec{\omega}) = \frac{i}{2\pi\hbar\omega V}\int_{\infty}^{\infty}\frac{d\omega'}{\omega-\omega'+i\delta}\int_{\infty}^{\infty}dt\langle\left[J\mu(\vec{q},t),\ J\nu(-\vec{q},0)\right]\rangle_o(\cos\omega t+i\sin\omega t)$$

$$\equiv \sigma_{\mu\nu_1} + i\sigma_{\mu\nu 2}$$

where $\sigma_{\mu\nu 1}$ is the real and $\sigma_{\mu\nu 2}$ the imaginary part of the conductivity. Comparing this equation with the Kramers-Kronig relations makes it immediately obvious that

$$\sigma_{\mu\nu 1}(\vec{q},\omega) = \frac{1}{2\hbar\omega V}\int_{-\infty}^{\infty}dt\langle\left[J\mu(\vec{q},t),\ J\nu(-\vec{q},0)\right]\rangle_o\cos\omega t$$

$$\sigma\mu\nu_2(\vec{q},\omega) = \frac{-1}{2\hbar\omega V}\int_{-\infty}^{\infty}dt\langle\left[J\mu(\vec{q},t),\ J\nu(-\vec{q},0)\right]\rangle_o\sin\omega t$$

The only remaining task is to evaluate the expectation value of the commutator.

Recall

$$\langle\left[J(t),\ J(0)\right]\rangle_o = T_r\rho_o\{J(t)J(0) - J(0)J(t)\}$$

$$= \sum_\alpha P_\alpha\langle\alpha|J(t)J(0)|\alpha\rangle - \sum_\alpha P_\alpha\langle\alpha|J(0)J(t)|\alpha\rangle$$

$$= \sum_{\alpha\beta} P_\alpha\langle\alpha|J(t)|\beta\rangle\langle\beta|J(0)|\alpha\rangle \sum_{\alpha\beta}{}_\beta\langle\beta|J(0)|\alpha\rangle\langle\alpha|J(t)|\beta\rangle$$

where $|\alpha\rangle$ and $|\beta\rangle$ have been exchanged in the second sum

$$= \sum_{\alpha\beta} P_\alpha\langle\alpha|J(t)|\beta\rangle\langle\beta|J(0)|\alpha\rangle\ (1-\frac{P_\beta}{P_\alpha})$$

For most situations the ensemble characterising the system is canonical, e.g.

$$P_\alpha = \frac{e^{\frac{E_\alpha}{kT}}}{\sum_\alpha e^{\frac{E_\alpha}{kt}}}$$

and

$$\langle [J(t),J(0)] \rangle_o = \sum_{\alpha\beta} P_\alpha \langle \alpha|J(t)|\beta\rangle\langle\beta|J(0)|\alpha\rangle (1-e^{\frac{\hbar\omega_{\alpha\beta}}{kT}})$$

$$= (1-e^{-\frac{\hbar}{kT}}) \langle J(t)J(0)\rangle_o$$

so finally

$$\sigma_1 = \frac{1}{2\hbar\omega V} (1-e^{-\frac{\hbar\omega}{kT}}) \int_\infty^\infty dt \langle J_\mu(\vec{q},t)\ J_\nu(-q,0)\rangle_o \cos\omega t$$

$$\sigma_2 = \frac{1}{2\hbar\omega V} (1-e^{-\frac{\hbar\omega}{kT}}) \int_\infty^\infty dt \langle J_\mu(\vec{q},t)\ J_\nu(-q,0)\rangle_o \sin\omega t$$

are the expressions for the real and imaginary parts of the conductivity.

7. Fluctuation-Dissapation Theorem

The conductivities calculated in the previous section are the ones used in Chapter III, on fluctuations in a superconductor. Another method of doing that calculation is to use the fluctuation-dissapation theorem; this is the way that Schmidt[27] attacks the problem. Returning to the middle of section 5 and rewriting the equation for $\chi(\omega)$

$$\chi(\omega) = \frac{1}{2\pi\hbar}\int_{-\infty}^{\infty}\frac{d\omega'}{\omega-\omega'+ie}\,\phi(\omega')$$

with

$$\phi(\omega') = \int_{-\infty}^{\infty}dt\; e^{i\omega' t}\langle[J(t),J^{+}(0)]\rangle_{o} = (1-e^{\frac{\hbar\omega'}{kT}})$$

$$\int_{-\infty}^{\infty}dt e^{i\omega' t}\langle J(t)J^{+}(0)\rangle_{o}$$

called the spectral response function. Now consider

$$\psi(\omega') = \int_{-\infty}^{\infty}dt\; e^{i\omega' t}\langle\{J(t),J^{+}0)\}\rangle_{o}$$

where $\{J,J^{+}\} \equiv J^{+}J + J^{+}J$. The expectation value of this is

$$\langle\{J(t),J^{+}(0)\}\rangle_{o} = \mathrm{Tr}\rho_{o}(J(t)J^{+}(0) + J^{+}(0)J(t))$$

With an analysis exactly following that for the commutator $\psi(\omega')$ becomes

$$\psi(\omega') = (1+e^{\frac{\hbar\omega'}{kT}})\int_{-\infty}^{\infty}dt\; e^{i\omega' t}\langle J(t)J^{+}(0)\rangle_{o}$$

the only difference being the plus sign. Next, write

$$\langle|J(0)|^{2}\rangle = \frac{1}{2}\langle J(0)J^{+}(0) + J^{+}(0)J(0)\rangle_{o}$$

$$= \frac{1}{2}\lim_{t\to 0}\int_{-\infty}^{\infty}\frac{d\omega}{2\omega}\,e^{-i\omega t}\,\psi(\omega)$$

$$= \frac{1}{2}\int_{-\infty}^{\infty}\frac{d\omega}{2\pi}\,\phi(\omega)\,\frac{\psi(\omega)}{\phi(\omega)}$$

$$\langle|J(0)|^{2}\rangle\ \frac{1}{2}\int_{-\infty}^{\infty}\frac{d\omega}{2\pi}\,\phi(\omega)\coth\frac{\hbar\omega}{kT}$$

Now by using

$$\chi(\omega) = \frac{1}{2\pi\hbar}\int_{-\infty}^{\infty}\frac{\phi(\omega')d\omega'}{\omega-\omega'+ie} = \frac{1}{2\pi\hbar}\,P\int_{-\infty}^{\infty}\frac{\phi(\omega')d\omega'}{\omega-\omega'} - \frac{1}{2\hbar}\int_{-\infty}^{\infty}\delta(\omega-\omega')\phi(\omega')d\omega'$$

one gets

$$\chi(\omega) = \frac{1}{2\pi\hbar}\,P\int_{-\infty}^{\infty}\frac{\phi(\omega')d\omega'}{\omega-\omega'} - \frac{i}{2\hbar}\,\phi(\omega)$$

The first term is the real part of χ and the second the imaginary part, since it is easy to show that ϕ is real. (Take the complex conjugate, let t become -t and you will recover ϕ.) Then

$$\langle|J|^2\rangle = -\hbar\int_{-\infty}^{\infty}\frac{d\omega}{2\pi}\,\mathrm{Im}\,\chi(\omega)\,\coth\frac{\hbar\omega}{kT}$$

This is the fluctuation-dissapation theorem. At low frequencies, where $\coth\frac{h\omega}{kT} = \frac{2kT}{\hbar\omega}$, where $\phi\to 0$ causing $\mathrm{Im}\chi\to 0$ also, then from Kramers-Kronig

$$\langle|J|^2\rangle = -\frac{kT}{\pi}\int_{-\infty}^{\infty}\frac{d\omega\,\mathrm{Im}\chi(0)}{\omega}$$

$$= -kT\lim_{\omega\to 0} R_e\,\chi(\omega)$$

and

$$\chi(0) = -\frac{1}{kT}\langle|J|^2\rangle$$

APPENDIX D

UNSUCCESSFUL EXPERIMENTS

The purpose of this appendix is to mention a few things that didn't quite come off but which might be of some interest or use.

1. Coated Lead Films

The first attempts at the fluctuation experiments were done on lead films grown in a separate evaporator and then mounted on a standard sample rotator. In order to protect the surfaces of the films they were covered by an evaporated layer of KCl after the lead evaporation but before removal from the high vacuum. The KCl protected the lead surfaces from oxidation. The way it was done was as follows. First, KCl substrates were cleaved, put into the evaporator and four narrow gold strips were deposited for resistance probes. Then the evaporator was opened and the mask was changed to a circular one. After evacuation the substrates were cooled to near liquid nitrogen temperature and the lead and KCl evaporations followed in quick succession. They were then warmed up, removed, leads were soldered to the gold contacts, and they were mounted to a variable temperature sample rotator.

The problem was that it was not possible to get continuous films that transmitted enough to make the very sensitive measurements needed for the fluctuation experiments. Measurements of the transmission at 4.2^{o} or 1.2^{o} compared to that at 90^{o} K showed the peak at the energy gap first seen by Glover and

Tinkham[28] very nicely indeed. This might be a good method for preparing samples designed for high pressure experiments on superconductors.

2. Coaxial Light Cones.

Following a calculation by R.K. Elsley on the low frequency cutoff of cylindrical waveguides compared with a coaxial arrangement which has no such cutoff, a comparison was made between the transmission at room temperature of a standard condensing cone (1/2 inch to 3/16 inch) to a similar cone with a 1/16 inch brass rod down the center. It was expected that the latter would show an improved transmission at around 2 cm^{-1}.

Well, it did, sort of. Compared to the standard cone the coaxial one transmitted 90% at 2 cm^{-1} and 80% at 8 cm^{-1}. The brass rod simply took up too much area. If a very thin wire could be stretched down the center of a light cone or light pipe and could be kept centered and straight it would probably be worth doing.

3. Crystal Quartz.

The first experiments on small particles were done with the particles mounted on crystal quartz blanks. One can imagine the delight when temperature dependence on these samples showed a decrease in transmission at the lowest frequencies (beginning at 3 cm^{-1} and becoming less at lower frequencies) as the temperature was reduced. There was another absorbtion band at 25 cm^{-1}. One can equally imagine the distress when this was found to be an artefact of the quartz

on which the particles were sitting.

This is not really an unsuccessful experiment but rather an uncompleted one. There is a very low frequency absorbtion in crystal quartz at very low temperatures. The problem will arise in deciding whether this is due to the quartz itself (unlikely) or to some impurity (and if so then what?).

REFERENCES TO APPENDICES

Appendix A. V_3Si.

1. B.W. Batterman and C.S. Barrett, Phys. Rev. Letters 13, 390 (1964).

2. H.J. Levinstein and J.E. Kunzler, Phys. Letters 20, 581 (1966).

3. J.J. Hauser, D.D. Bacon, and W.H. Haemmerle, Phys. Rev. 151, 296 (1966).

4. V. Hoffstein and R.W. Cohen, Phys. Letters 29A, 603 (1969).

5. D.R. Bosomworth and G.W. Cullen, Phys. Rev. 160, 346 (1967).

6. J. Labbe and J. Friedel, J. Phys. Radium 27, 153, 303 (1966); J. Labbe, S. Barisic, and J. Friedel, Phys. Rev. Letters 19, 1039 (1967).

7. D.E. Williamson, J. Opt. Soc. Am. 42, 712 (1952).

8. W.E. Lamb, Phys. Rev. 70, 308 (1946).

9. C.H. Townes and A.L. Schallow, Microwave Spectroscopy, (McGraw-Hill, 1955) p. 391.

10. M. Tinkham in Far Infrared Properties of Solids, Mitra and Nudelman, eds. (Plenum, 1970).

Appendix B. Infrared Properties of Metals.

11. M. Tinkham in Far Infrared Properties of Solids, Mitra and Nudelman, eds. (Plenum, 1970).

12. A.V. Solokov, Optical Properties of Metals, (American Elsevier, 1967). Chapter 1.

13. B.D. Donovan, Elementary Theory of Metals, (Pergamon, 1967) Chapter 9.

14. D.C. Mattis and J. Bardeen, Phys. Rev. 111, 412 (1958).

15. A.A. Abrikosov, L.P. Gor'kov, and I.M. Khalatnikov, Sov. Phys. JETP 8, 182 (1959).

16. P.B. Miller, Phys. Rev. 118, 928 (1960).

17. R.A. Ferrell and R.E. Glover, Phys. Rev. 109, 1398 (1958).

18. M. Tinkham and R.A. Ferrell, Phys. Rev. Letters 2, 331 (1959).

19. E. Hagen and H. Reubens, Ann. Physik 1, 352 (1900); 11, 873 (1903).

20. L.N. Hadley and D.M. Dennison, J. Opt. Soc. Am. 37, 451 (1947).

21. G. Mie, Ann. Physik 25, 377 (1908).

22. P. Debye, Ann. Physik 30, 57 (1909).

23. M. Born and E. Wolf, Principles of Optics, (Pergamon, 1964), Section 13.5.

24. L.D. Landau and E.M. Lifshitz, Electrodynamics of Continuous Media , (Addison-Wesley, 1960), Sections 72 and 73.

Appendix C. Linear Response Theory

25. P.C. Martin in DeWitt and Balain, eds., Many Body Physics (Probleme a N-Corps), (Gordon and Breach, 1968).

26. J.W. Wilkins, Physics 653, Cornell University (1968).

27. H. Schmidt, Z. Physik 216, 336 (1968); 232, 442 (1970).

Appendix D. Unsuccessful Experiments.

28. R.E. Glover and M. Tinkham, Phys. Rev. 108, 243 (1957).